An experimental and numerical study of the small scales of a passive scalar field generated by a line source in turbulent channel flow

Emmanuel Germaine

Doctor of Philosophy

Department of Mechanical Engineering

McGill University

Montréal, Québec

December 2012

A thesis submitted to McGill University in partial fulfillment of the requirements of the degree of Doctor of Philosophy.

TABLE OF CONTENTS

ABSTRACT

The prediction and control of the turbulent mixing of passive scalars is of particular interest to a variety of engineering fields. The present research aims to improve our incomplete understanding of this subject. In this regard, we study, by means of both experiments and numerical simulations, the evolution of a passive scalar (temperature) injected in a highly anisotropic manner at small scales into an inhomogeneous turbulent flow. The source of the scalar consists of a fine heated wire placed in the flow, generating a thermal plume downstream. Multiple phenomena (including turbulent mixing within the plume, molecular diffusion, etc.) play a role in the evolution of the temperature fluctuations, θ, which dissipate with increasing distance from the source. The scalar dissipation rate ($\varepsilon_\theta \equiv \alpha\langle(\partial\theta/\partial x_i)^2\rangle$, where α is the thermal diffusivity of the fluid) represents the rate at which the scalar variance is destroyed. The dissipation process occurs at the smallest scales of the turbulence and is still not completely understood. In this work, particular attention is paid to the evolution of the three components of the scalar dissipation rate, i.e. $\varepsilon_{\theta_x} \equiv \alpha\langle(\partial\theta/\partial x)^2\rangle$, $\varepsilon_{\theta_y} \equiv \alpha\langle(\partial\theta/\partial y)^2\rangle$ and $\varepsilon_{\theta_z} \equiv \alpha\langle(\partial\theta/\partial z)^2\rangle$, to further understand the small scales of the scalar field and, in particular, examine the return to isotropy of the (anisotropically-generated) scalar field.

The experiments were carried out in a turbulent channel flow facility. The scalar fluctuations were measured by means of cold-wire thermometry and ε_θ was determined by estimating the derivatives of the temperature fluctuations. The transverse derivatives were estimated using a pair of parallel cold-wires, whereas the longitudinal derivative was estimated using a single cold-wire and Taylor's hypothesis.

Direct numerical simulations were also performed to both reproduce the experimental results and provide additional data that is experimentally inaccessible. To this end, a new computer program, called 3DFLUX, was developed and implemented. 3DFLUX is a fully three-dimensional, high-order, conservative, monotonicity preserving, flux integral method for the solution of the advection-diffusion equation. It is nominally third-order in space and second-order in time, and generates low numerical diffusion and anisotropic distortion. In addition, 3DFLUX, is guaranteed to be free of splitting errors and has a better convergence rate than widely used one-dimensional techniques, such as the piecewise parabolic method (PPM), the weighted essentially non-oscillatory (WENO) method, and the recently-proposed jet scheme, which is based on the level-set method. A detailed presentation of 3DFLUX is reported in this thesis.

In contrast with recent research using alternate numerical approaches, we show that the experiments and numerical simulations are in excellent agreement for both the large- and small-scales statistics of the scalar field. In addition, combining the obtained results with the two approaches enable us to analyze and provide insight on the nature of a turbulent scalar plume injected at small scales. We show that the return to isotropy of the small scales is never perfectly observed in any region of the channel for the downstream distances studied herein. However, the small-scale anisotropy measured in the central region is smaller than the persistent anisotropy observed in the near-wall region, which is found to be most prominent in the numerical simulations, which are performed at a lower Reynolds number than the experiments. The mean velocity gradient plays a key role in the evolution of ε_θ and in this lack of isotropization of the small scales of the scalar field.

RÉSUMÉ

Les écoulements fluides turbulents jouent un rôle majeur dans de nombreuses applications industrielles. L'objectif de cette recherche est d'approfondir notre compréhension des mécanismes mis en jeu lorsque ces écoulements sont utilisés pour le transport ou le mélange de scalaires. Plus précisément, cette étude, qui associe à la fois expérience et simulation numérique, s'intéresse à l'évolution d'une quantité scalaire (la température) lorsque celle-ci est injectée de manière anisotrope et aux petites échelles de la turbulence dans un écoulement turbulent non-homogène. L'injection de température fût réalisée à partir d'une source linéaire de chaleur (fil fin chauffé), créant ainsi un panache thermique dans l'écoulement. Plusieurs processus physiques tel que le brassage induit par la turbulence ou la diffusion moléculaire au sein du panache, contribuent à l'évolution des fluctuations de température, θ. Ces fluctuations se dissipent avec l'éloignement en aval du point d'injection. Le taux de dissipation de la variance du scalaire ($\varepsilon_\theta \equiv \alpha\langle(\partial\theta/\partial x_i)^2\rangle$ ou α est la diffusivité thermique du fluide) représente le taux auquel les fluctuations du champs scalaire sont détruites. La dissipation s'opère aux petites échelles de la turbulence et les mécanismes qui la mettent en œuvre sont encore mal compris de nos jours. Dans cette étude, une attention particulière est portée sur l'évolution des trois composantes du taux de dissipation du champs scalaire $\varepsilon_{\theta_x} \equiv \alpha\langle(\partial\theta/\partial x)^2\rangle$, $\varepsilon_{\theta_y} \equiv \alpha\langle(\partial\theta/\partial y)^2\rangle$ et $\varepsilon_{\theta_z} \equiv \alpha\langle(\partial\theta/\partial z)^2\rangle$, afin d'en extraire des informations sur le comportement anisotrope des petites structures du champs scalaire.

Les expériences fûrent menées dans un écoulement turbulent de canal et les fluctuations du champs scalaire fûrent mesurées au moyen de la thermométrie à fil froid. Le taux de dissipation, ε_θ, fût déduit des mesures des dérivées spatiales des fluctuations de température; les dérivées spatiales transversales étant

mesurées à l'aide d'une sonde, spécialement conçue à cet effet, et possédant deux fils froids parallèles alors que la dérivée longitudinale fût estimée à partir d'une mesure de dérivée temporelle avec un seul fil (hypothèse de Taylor).

Des simulations numériques directes fûrent mises en œuvre afin de reproduire les résultats expérimentaux et de fournir des données d'analyse supplémentaires et inaccessibles expérimentalement. Le développement d'un nouveau code numérique appelé 3DFLUX a constitué une partie importante de cette recherche. 3DFLUX est basé sur une méthode numérique d'intégration des flux. C'est un schéma multi-dimensionnel, parallelisable, d'ordre élevé, conservatif et qui garantie la monotonicité de la solution. Nous montrons notamment que 3DFLUX est d'ordre 3 et 2 respectivement en espace et en temps et qu'il présente des taux de convergence supérieurs aux techniques uni-dimensionnelles très répandues telles que les méthodes PPM « piecewise parabolic method », WENO « weigthed essentially non-oscillatory » ou une méthode récente nommée « jet scheme » et basée sur des techniques dites « level-set ». Une description détaillée de 3DFLUX est rapportée dans cette thèse.

En opposition avec des publications récentes et basées sur des méthodes numériques différentes, nos resultats montrent une excellente corrélation entre les approches numériques et expérimentales autant pour les grandes que pour les petites échelles du champs scalaire. Finalement, cette étude apporte plusieurs éléments nouveaux sur l'évolution d'un champs scalaire lorsque celui-ci est injecté à petite échelle dans un écoulement turbulent. Le retour à l'isotropie des fines structures du champs scalaire n'est pas clairement observée dans le canal aux positions, etudiées dans ce mémoire, en aval de la source. Toutefois, l'anisotropie des petites échelles est faible dans la région centrale du canal en comparaison à celle mesurée dans la région pariétale, d'autant plus

importante dans les simulations numériques; celles-ci étant réalisées à un nombre de Reynolds qui est inférieur à celui des expériences. Le rôle du gradient de vitesse moyenne dans l'évolution de ε_θ est analysé pour justifier ce non-retour à l'isotropie.

PREFACE

The work outlined in this manuscript thesis was carried out in the Department of Mechanical Engineering at McGill University from September 2007 to December 2012. It is submitted to McGill University in partial fulfillment of the requirements of the degree of Doctor of Philosophy.

Contributions of authors

This manuscript-based thesis is composed of two articles. Although the work for this thesis has been performed in close collaboration with my supervisors, Prof. Luca Cortelezzi and Prof. Laurent Mydlarski, my contribution has been the predominant one for each publication. The details of these contributions are summarized below.

Manuscript 1 (Chapter 2): *3DFLUX: A high-order fully three-dimensional flux integral solver for the scalar transport equation.* This manuscript has been published in the *Journal of Computational Physics*. Under the supervision of my two co-authors, Laurent Mydlarski and Luca Cortelezzi, I:

i) developed and implemented the algorithm (3DFLUX),

ii) executed both the experiments and the numerical simulations,

iii) analyzed the results, and

iv) wrote the manuscript, which was subsequently edited by Luca Cortelezzi.

Manuscript 2 (Chapter 3): *Evolution of the scalar dissipation rate emitted from a concentrated line source in turbulent channel flow.* This manuscript has been submitted to the *Journal of Fluid Mechanics*. Under the supervision of my two co-authors, Luca Cortelezzi and Laurent Mydlarski, I:

i) executed the simulations,

ii) executed the experiments,

iii) analyzed the resulting experimental and numerical data, and

iv) wrote the manuscript, which was subsequently edited by Laurent Mydlarski.

Statement of Originality

The objective of this thesis is to investigate by means of both experiments and numerical simulations the scalar dissipation rate in a turbulent flow. To that end, I developed a new numerical scheme (3DFLUX) to solve the scalar transport equation, simulating the mixing of a scalar field in a turbulent flow. The convergence rate and accuracy of 3DFLUX was characterized using several multidimensional tests. 3DFLUX is found to be noticeably more accurate than the currently available numerical schemes having the same convergence rate and is expected to be a promising code for the simulation of practical engineering applications. Reaping the complementary benefits of experiments and numerical simulations, the scalar dissipation rate of the temperature field generated by a line source in a turbulent channel flow was investigated. To the best of my knowledge, the present research — which analyzes spectra, probability density functions, wall-normal and downstream evolutions, anisotropies and conditional expectations of the three individual components of the scalar dissipation rate by means of both experiments and direct numerical simulations — has no analog in the scientific literature.

ACKNOWLEDGEMENTS

First of all, I would like to express my most sincere thanks to Prof. Laurent Mydlarski and Prof. Luca Cortelezzi who co-supervised my Ph.D. thesis. They gave me the opportunity to perform both experimental and numerical research in the exciting scientific field of turbulent flows. It is thanks to their valuable suggestions, guidance and continuous encouragement that I was able to undertake this project. Their support increased my motivation for going deeper and deeper into the subject, pushing my limits farther that I expected. Thanks to them, I now understand the meaning and implication of the famous quote "Stay hungry. Stay foolish." Finally, their commitment allowed me to present my work at prestigious international conferences, where I had the opportunity to meet many eminent scientists. Thank you.

I would like to acknowledge the financial support of the Werner Graupe Foundation for the first three years of my Ph.D. Furthermore, I thank again my supervisors for their financial support during the last part of my studies.

I am very grateful to Jan Binder, Systems Manager at the Centre for Intelligent Machines for his helpful and continuous support. I am more than indebted to Oleg Gubanov for teaching me the fundamentals of advanced techniques in `C++` programming. Thank you, Oleg, you gave me the tools to build the core of this thesis. I also would like to thank Maxime Boucher and Jason Lepore for the numerous discussions we had that were very instructive and productive for my research. Thank you.

I would like to thanks Prof. Gérard Lavergne and Prof. Azemi Benaissa from l'Institut Supérieur de l'Aéronautique et de l'Espace (ISAE - Supaéro) and the Royal Military College of Canada, respectively. You both inspired me

and convinced me to pursue Ph.D. studies at McGill University. You were right, it was definitively an invaluable experience. Thank you.

To my friends Tristan and Audrey Tichadou, Frédéric and Delphine Ressaire, Emmanuel Piuze, Mathieu Porte, Aurelien Labrosse and my cousin Olivier Teisserenc – thank you for your support and invaluable friendship.

As always, my family has been there for me. I am very grateful for the encouraging support of my parents, Michel and Janine, my sister, Estelle and my in-laws, Babu and Catherine Bommel, and Ilinka Ghika. I am also particularly thankful to Pierre Bommel who inspired me to apply to McGill University's Ph.D. program – thank you so much to all of you.

Finally, I would like to give very special thanks to my love Ioana for tirelessly supporting me through this experience. You definitively were the rock that kept me in touch with reality throughout my studies. I can never thank you enough.

To my daugthers Maëlle and Camille,
to my nephew Mathis
I love you, thank you for helping me keep my work in perspective,
"Stay hungry. Stay foolish." (Whole Earth Catalog, 1974).

CHAPTER 1

Introduction

The ability of turbulence to mix a scalar quantity (i.e. energy, chemical species concentration, etc.) is of particular interest to a variety of engineering fields, such as combustion, pollutant dispersion and heat transfer. For example, combustion only occurs if the fuel and oxidizer are mixed at the molecular level; ecological problems arise if dangerous chemicals are not sufficiently diffused when emitted into the environment. In these examples, the prediction and the control of the combustion or the pollutant dispersion require an accurate understanding of the phenomena that govern mixing in turbulent flows. However, our understanding of this process remains incomplete.

The present thesis focuses on the evolution of a scalar injected at small scales into a turbulent flow. The source of the scalar (temperature, herein) consists of a fine heated wire placed in the flow, creating a thermal plume downstream of the source. After being injected, the scalar field is advected, stretched and distorted due to the chaotic nature of the flow. Turbulent mixing by eddies that are larger than the plume, turbulent mixing within the plume (i.e. by eddies that are smaller than the plume), and molecular diffusion are some of the phenomena that play a role in the evolution of the temperature fluctuations. Repeated stretching and folding of the scalar field results in smaller and smaller structures, until the scalar variance is removed

(or "dissipated") by molecular diffusion. This, being said, the mechanisms that effect the scalar dissipation remain unclear. The present research aims to analyze the scalar dissipation rate by means of both experiments and numerical simulations.

As previously noted, the scalar under consideration in this work is temperature. In addition, the latter is classified as a *passive scalar* when the temperature differences are small enough to not affect the dynamics of the flow. Note that the formalism presented in this study also applies to any other passive scalar. The use of a passive scalar therefore permits observations of the dynamics of the flow, which are responsible for the mixing, but independent of the scalar field being mixed.

In theory and under certain conditions (described in section 1.1), the large scales, strongly affected by the boundary conditions and therefore generally anisotropic, are decoupled from the small-scales; the latter being statistically isotropic. However, numerous experiments have reported persistent anisotropy of the scalar field even when *i)* the scalar is advected by an isotropic velocity field, and *ii)* both the large and small scales of the scalar field are of the same order of magnitude as those of the velocity field (Warhaft, 2000). These results contradict the notion of a possible independence of the largest and smallest scales of the scalar field. Hence, the scalar field must be analyzed carefully and separately, given that it does not emulate the turbulent velocity field in a straightforward manner.

Furthermore, in many applications of turbulent scalar mixing, the length scales of the thermal field are different (sometimes drastically so) from those of the hydrodynamic turbulence. This difference only increases the difficulties in modeling scalar mixing. For example, the same scalar, when injected at two different scales, is not, *a priori*, expected to evolve similarly in the two cases.

Consequently, the present research studies in detail the evolution of a passive scalar when it is injected into a turbulent flow at scales far smaller than the largest scales of the (advecting) velocity field.

1.1 Theoretical Background

The evolutions of the instantaneous velocity ($\tilde{U}_i$) and pressure ($\tilde{p}$) fields in a constant property flow are determined by the equations of conservation of mass and momentum

$$\frac{\partial \tilde{U}_i}{\partial x_i} = 0, \quad \frac{\partial \tilde{U}_i}{\partial t} + \tilde{U}_j \frac{\partial \tilde{U}_i}{\partial x_j} = -\frac{1}{\rho}\frac{\partial \tilde{p}}{\partial x_i} + \nu \frac{\partial^2 \tilde{U}_i}{\partial x_j^2}, \tag{1.1}$$

where ρ is the density of the fluid and ν is its kinematic viscosity. Given i) the difficulty in finding solutions to the above equations in the turbulent regime, and ii) the random nature of turbulent flows, the dependent variables lend themselves to statistical analysis. To this end, instantaneous quantities are decomposed into mean, $\langle U_i \rangle$, and fluctuating, u_i, quantities using the Reynolds decomposition: $\tilde{U}_i \equiv \langle U_i \rangle + u_i$, where angular brackets ($\langle\rangle$) denote averages.

The governing equations for the mean flow are obtained by applying the above decomposition and averaging. The result is

$$\frac{\partial \langle U_i \rangle}{\partial x_i} = 0, \quad \frac{\partial \langle U_i \rangle}{\partial t} + \langle U_j \rangle \frac{\partial \langle U_i \rangle}{\partial x_j} = -\frac{1}{\rho}\frac{\partial \langle p \rangle}{\partial x_i} + \nu \frac{\partial^2 \langle U_i \rangle}{\partial x_j^2} - \frac{\partial \langle u_i u_j \rangle}{\partial x_j}. \tag{1.2}$$

The new terms, $\langle u_i u_j \rangle$, which originate from the Reynolds decomposition are called Reynolds stresses. They are unknown, and thus cause a closure problem for the Reynolds-averaged Navier-Stokes (RANS) equations.

The tendency towards either laminar or turbulent flow depends upon the balance of forces acting on the fluid. The inertial force (per unit volume) is given by $\rho U^2/L$, whereas the viscous one is $\mu U/L^2$, where L is some characteristic length of the system, U is an average fluid velocity, ρ is the density

of the fluid, and μ is its dynamic viscosity. The ratio of these forces is defined to be the Reynolds number ($Re \equiv \rho UL/\mu$). At low Reynolds numbers, viscous forces dominate and the flow is laminar. Once the Reynolds number exceeds some critical value, the inertial forces become predominant and the flow transitions from laminar to turbulent.

The theoretical foundation of (hydrodynamic) turbulence was proposed by Kolmogorov (1941). This work, commonly referred to as $K41$, provides insight into the roles played by the different length scales within a turbulent flow, from the largest (integral) length scale, ℓ, to the smallest length scale, η. Kolmogorov's theory is based upon three fundamental ideas. The first is that, at sufficiently high Reynolds numbers, the small scales of the turbulent motion are statistically isotropic (the postulate of local isotropy). Given this, Kolmogorov proposed two hypotheses pertaining to the nature of small-scale turbulence. The first states that, at sufficiently high Reynolds numbers, the statistics of the small-scale motions have a universal form that is uniquely determined by the kinematic viscosity ν ($= \mu/\rho$) and the dissipation rate of the turbulent kinetic energy $\varepsilon = (\nu/2)\langle(\partial u_i/\partial x_j + \partial u_j/\partial x_i)^2\rangle$. One consequence of this hypothesis is that the Kolmogorov length scale η is given to be $(\nu^3/\varepsilon)^{1/4}$. The second states that, at sufficiently high Reynolds numbers, and for scales that are neither large nor small (i.e. those found in the "inertial subrange"), the statistics have a universal form uniquely determined by ε, and independent of ν. Kolmogorov therefore establishes a distinct separation between the large and the small scales. The former are anisotropic because of their dependence on the geometry of the problem. They contain the majority of the turbulent kinetic energy and have relatively long timescales/lifetimes. The smallest scales are responsible for the dissipation of the kinetic energy. They have a short lifetime and are assumed to be isotropic. Between the large scales, $O(\ell)$,

and the smallest scales, $O(\eta)$, an inertial subrange exists in which turbulent kinetic energy is transferred. This transfer is observed in the power spectrum of turbulent kinetic energy and is characterized by the well-known "$-5/3$" power-law.

$K41$ introduces several concepts necessary to the description of the transport and dissipation of turbulent kinetic energy in a turbulent flow. As there is also significant interest in heat and mass transfer, Kolmogorov's arguments were extended by Obukhov (1949) and Corrsin (1951) to the transport of passive scalars. Kolmogorov Obukhov Corrsin (KOC) phenomenology is based on analogous notions to those of K41, starting with a similar postulate of local isotropy for the scalar field, which states that, at sufficiently high Reynolds and Péclet numbers ($Pe = UL/\alpha$, where α is the scalar (thermal) diffusivity), it assumes that there is a decay of any large-scale anisotropy when smaller and smaller scales are considered. The first KOC hypothesis states that at sufficiently high Reynolds and Péclet numbers, the statistics of the small scales are uniquely governed by the kinematic viscosity, ν, the scalar diffusivity, α, the dissipation rate of turbulent kinetic energy, ε, and the scalar dissipation rate, ε_θ ($\equiv \alpha\langle(\partial\theta/\partial x_i)^2\rangle$). Secondly, it hypothesizes that, at sufficiently high Reynolds and Péclet numbers, the large and small scales are connected by an "inertial-convective subrange" in which the scalar statistics are uniquely determined by ε and ε_θ and are independent of ν and α. This range comprises scales smaller than the large scales, ℓ and ℓ_θ, and larger than the small dissipative scales, η and η_θ. The smallest hydrodynamic and scalar scales (η and η_θ, respectively) are related by the Prandtl ($Pr = \nu/\alpha$) or Schmidt ($Sc = \nu/D$, where D is the molecular diffusivity of a chemical species in a fluid) numbers. Note that η_θ and η are of the same order of magnitude in the air flow studied herein, where $Pr \sim O(1)$.

The evolution of the instantaneous scalar concentration, say temperature, T, in a constant property flow is determined by the advection-diffusion equation

$$\frac{\partial \tilde{T}}{\partial t} + \tilde{U}_j \frac{\partial \tilde{T}}{\partial x_j} = \alpha \frac{\partial^2 \tilde{T}}{\partial x_j^2} + S, \tag{1.3}$$

where S is a source term. This equation governs the evolution of $\tilde{T}$ given its transport by advection, its transport by molecular diffusion and the influence of the source term, S, which accounts for the increase in internal energy due to viscous dissipation. For an incompressible flow, at a sufficiently low Eckert number ($Ec = U_\infty^2/(c_p \Delta T) \ll 1$, where ΔT is a characteristic temperature difference of the flow), the source term, S, is negligible. The above equation depends explicitly on the velocity field. When the latter becomes turbulent, so can the scalar field, should the Péclet number be large enough. Thus, turbulent scalar fields also lend themselves to a statistical description, where mean quantities, $\langle T \rangle$, and fluctuations, θ, are similarly related to the instantaneous temperature: $\tilde{T} \equiv \langle T \rangle + \theta$.

The governing equation for the mean of the scalar, $\langle T \rangle$, is obtained by applying the above Reynolds decomposition to equation (1.3), and then averaging it. The result is

$$\frac{\partial \langle T \rangle}{\partial t} + \langle U_j \rangle \frac{\partial \langle T \rangle}{\partial x_j} = \alpha \frac{\partial^2 \langle T \rangle}{\partial x_j^2} - \frac{\partial \langle u_j \theta \rangle}{\partial x_j}. \tag{1.4}$$

Furthermore, the scalar variance, $\langle \theta^2 \rangle$, budget is obtained by subtracting the mean equation (1.4) from the instantaneous equation (1.3), multiplying by θ,

and averaging it

$$\underbrace{\frac{\partial}{\partial t}\langle\frac{1}{2}\theta^2\rangle}_{(i)} + \underbrace{\langle U_j\rangle\frac{\partial}{\partial x_j}\langle\frac{1}{2}\theta^2\rangle}_{(ii)} = -\underbrace{\frac{\partial}{\partial x_j}\langle\frac{1}{2}u_j\theta^2\rangle}_{(iii)} + \underbrace{\alpha\frac{\partial^2}{\partial x_j^2}\langle\frac{1}{2}\theta^2\rangle}_{(iv)} - \underbrace{\langle u_j\theta\rangle\frac{\partial\langle T\rangle}{\partial x_j}}_{(v)} - \underbrace{\alpha\langle\frac{\partial\theta}{\partial x_j}\frac{\partial\theta}{\partial x_j}\rangle}_{(vi)}. \tag{1.5}$$

This equation provides insight into the physical phenomena that govern the evolution of scalar fluctuations. It shows that the rate of change *(i+ii)* of $\langle\theta^2\rangle$ is controlled by turbulent advection *(iii)*, molecular diffusion *(iv)*, production *(v)*, and (molecular) dissipation, ε_θ *(vi)*.

The existence of an inertial subrange in the kinetic energy spectrum requires a large separation between the integral and dissipative scales. This condition is respected when the turbulent Reynolds number ($R_\ell = u_{rms}\ell/\nu$) is sufficiently high, because $\ell/\eta \sim R_\ell^{3/4}$. Similarly, the transfer of the scalar variance from the large to small scales, via an inertial-convective subrange, is only possible when both the Reynolds and Péclet numbers are sufficiently high. Therefore, for KOC theory to be valid, the scalar injection and dissipation scales must also be separated. However, when the injection is performed at small scales, the statistics of the scalar field are significantly different when examined near the source, as compared to far downstream. Near the source, the scalar field is highly anisotropic, of small integral length scale (ℓ_θ), and concentrated in a small region of the flow. Most of the contribution to the scalar variance is due to the flapping of the plume by the large-scale velocity field. As the plume broadens, the range of scales increases. Sufficiently far downstream of the source, the thermal wake develops internal large-scale structures. In this region, the separation between large and small structures

is more distinct and one could assume that the small scales tend to isotropy, as hypothesized by KOC theory.

In equation (1.5), the large scales generate scalar fluctuations through the action of the mean temperature gradient, the diffusion terms spread spots of different intensities, and the smallest scales "dissipate" the fluctuations by homogenizing the scalar's concentration. The three components of the scalar dissipation rate ($\varepsilon_{\theta_x} \equiv \alpha\langle(\partial\theta/\partial x)^2\rangle$, $\varepsilon_{\theta_y} \equiv \alpha\langle(\partial\theta/\partial y)^2\rangle$ and $\varepsilon_{\theta_z} \equiv \alpha\langle(\partial\theta/\partial z)^2\rangle$) can be used to quantify the local isotropy of the small scales of the scalar field and are consequently quantities of central importance that will be extensively analyzed in this work.

1.2 Motivation and Objectives

The majority of studies of turbulent scalar mixing focus on the evolution of a scalar field injected at large scales. Furthermore, in many cases, the flow under consideration in previous works was homogeneous and isotropic. The assumption of homogeneity considerably simplifies the analysis and yields interesting similarities between the scaling of the velocity and scalar fields when the injection occurs at large scales. However, such a configuration is not representative of many flows, which are generally inhomogeneous and exhibit discrepancies between the scales of the velocity and scalar fields. Furthermore, of the small subset of published articles that considered small-scale injection of the scalar field, few focus on the dissipation rate of the scalar fluctuations, even though ε_θ remains one of the less understood (yet most important) quantities within a turbulent flow. The small-scale injection of a scalar in an inhomogeneous flow is of relevance to engineering applications, such as the transport of a plume emitted by a smokestack in the atmospheric boundary layer, or the transport of a species injected in a combustion chamber before ignition. Although such applications are clearly important to modern life, few studies

of turbulent scalar mixing *i*) resulting from small-scale injection, and *ii*) focussing on the scalar dissipation rate, have been undertaken. This fact is the principal motivation for the present work.

The main objective of the present thesis is to further understand the evolution of the scalar field when injected (in a highly anisotropic manner) at small scales in an inhomogeneous turbulent flow. This research aims to *i)* provide new data on the nature of a turbulent scalar plume injected at small scales, and *ii)* ultimately improve our predictions of the phenomena that rely on turbulent scalar mixing. This will be accomplished by studying the evolution of the scalar dissipation rate in the flow under consideration.

The scalar dissipation rate is a critical quantity in the modeling and prediction of turbulent passive scalars. In many cases, local isotropy is invoked when estimating ε_θ. When the scalar is injected at small scales, such an assumption is clearly inaccurate near the source. Furthermore, though this assumption may increase in validity with increasing distance from the source, the rate at which it does so is an important factor. Therefore, particular attention will be paid to the evolution of the three different components of the scalar dissipation rate.

The scalar dissipation rate was analyzed by means of complementary experiments and numerical simulations. The latter can provide information that is difficult or impossible to obtain experimentally. In addition, a sensible combination of experiments and numerical simulations can provide deeper insight into the complex physical processes underlying the dissipation rate of scalar fields in turbulent flows.

1.3 Structure of the thesis

This document is a manuscript-thesis which contains two articles and is divided into four chapters. In the current chapter, the theoretical background

is discussed, and the motivation and objectives of the research are described. Chapter 2 contains the first article in which a new numerical solver (3DFLUX, designed for the solution of the advection-diffusion equation) is presented. Chapter 3 contains the second article in which our experimental and numerical analysis of the small scales of the scalar field generated downstream of a line source in fully developed, high-aspect ratio, turbulent channel flow is presented and discussed. Finally, the contributions of this research and possible future work are reported in the last chapter, which concludes this thesis.

1.4 Note on the literature review

Due to the specific format of a manuscript-thesis and the specificities of each article, i.e. the first one being related to a problem of computational physics, whereas the second-one deals with fluid mechanics, two literature reviews have been provided, separately, as a part of each manuscript.

CHAPTER 2

3DFLUX: A high-order fully three-dimensional flux integral solver for the scalar transport equation

2.1 Preface

As previously noted, the goal of this thesis is to investigate the evolution of the scalar dissipation rate that occurs when a scalar is mixed in a turbulent flow. One approach to study such a subject is by way of experiments. Another alternative is by means of numerical simulations. Both can reveal a great deal of valuable information and each can be sufficient for the majority of investigations of turbulent scalar mixing. However, noting that *i*) performing accurate simulations that provide reliable data is challenging and frequently requires validation using experimental data, and *ii*) numerical simulations can provide detailed data that are difficult, if not presently impossible to measure experimentally, both approaches are used in this thesis. Such a combined approach is complementary and should serve to improve the analysis. To this end, the present chapter describes the numerical method that was developed to simulate the experiments described in the next chapter.

The evolution of a scalar in a turbulent flow is governed by the advection-diffusion equation (1.3). An important problem in the realm of scientific computing is the accurate solution of this equation on a discretized grid by means of a high-fidelity solution that is undertaken at a reasonable computational

cost. Thus, accurate high-order schemes are preferred because of their low numerical dissipation and low dispersion errors. However, many aspects that can be neglected when using low-order schemes must be treated carefully when using high-order ones. To this end, I developed a new scheme, called 3DFLUX, using a conservative formulation of the semi-Lagrangian method. To the best of my knowledge, 3DFLUX is the first fully three-dimensional, high-order, conservative, selective monotonicity preserving, flux integral method, for the solution of the advection-diffusion equation. Its implementation is discussed in detail in the present chapter.

3DFLUX: A high-order fully three-dimensional flux integral solver for the scalar transport equation

Emmanuel Germaine, Laurent Mydlarski and Luca Cortelezzi

Department of Mechanical Engineering, McGill University, Montreal, Quebec, Canada

2.2 Abstract

We present a detailed derivation of a high-order, fully three-dimensional, conservative, monotonicity preserving, flux integral method for the solution of the equation for scalar transport in incompressible flow. This algorithm, named 3DFLUX, produces highly accurate solutions that are nearly unaffected by numerical dissipation, at a realistic computational cost. The performance of 3DFLUX is characterized by means of several challenging multidimensional tests. 3DFLUX is nominally third-order in space and second-order in time, however, at low Courant numbers, it appears to be superconvergent and, depending on the problem solved, is fourth-order or higher in space. Finally, 3DFLUX is used to simulate the transport of a scalar in a complex flow of practical relevance, and its results are in excellent agreement with experimental measurements.

Keywords: flux integral method; multidimensional transport equation; selective flux-limiters; monotonicity preservation; advection-diffusion equation.

2.3 Introduction

The scalar transport equation is encountered in a wide range of scientific applications. For example, it models the transport of a scalar (e.g. mass, energy, etc.) in a fluid flow, where it is known as the advection-diffusion equation. In economics, it is used to model the temporal evolution of a financial market, where it is known as the Black-Scholes equation. It constitutes an important tool for medical image analysis, where it takes the form of the Fokker-Planck equation. In biology, it can be used to simulate the dynamics of living species in their environment.

In engineering applications, the scalar transport equation is most often solved by finite difference or finite volume methods. The latter are employed to simulate fluid flows because of their strictly conservative formulation and their flexibility, which enables the solution of problems in complex geometries. Existing finite volume methods (Patankar, 1980; Versteeg & Malalasekera, 2007) are very robust, low-order and widely used in commercial software packages. They are reliable for industrial applications, but their accuracy is insufficient for scientific research.

Numerical methods that simulate the transport of a scalar are divided into two classes: Eulerian and Lagrangian. Eulerian methods solve the equation on a spatially fixed grid. Lagrangian methods solve the equation by tracking the path of the particles, and the nodes of the grid (used to discretize the computational domain) move with the particles. Lagrangian methods are more stable than Eulerian ones, but they require a re-meshing procedure that can be complex to implement and computationally expensive.

Semi-Lagrangian methods (Staniforth & Côté, 1991) constitute an appealing alternative approach as they combine the positive aspects of Eulerian and Lagrangian methods. Semi-Lagrangian methods solve the scalar transport

equation on a fixed grid by tracking a different set of particles at each time-step. They are widely used in meteorological applications because they are more stable than Eulerian schemes and simpler to implement than Lagrangian ones. The main disadvantage of semi-Lagrangian methods is that, in general, they are not conservative.

A conservative formulation of a semi-Lagrangian method was first presented by Leonard *et al.* (1995) using a flux integral approach. Leonard's scheme provides an explicit single-step, forward-in-time, conservative control volume update of the unsteady two-dimensional advection-diffusion equation. Other conservative, multidimensional, flux-based semi-Lagrangian methods for purely advective flows have been presented by Leveque (1996) and Harris *et al.* (2011). The advantage of using a multidimensional formulation is to avoid splitting techniques, which solve multidimensional problems as a sequence of one-dimensional schemes (Strang, 1968; Leonard *et al.*, 1996; Skamarock, 2006). Splitting techniques considerably simplify the algorithm on Cartesian grids, at the cost of inducing local splitting errors (Kozlov *et al.*, 2004). However, this advantage is lost on non-Cartesian grids where their implementation is complex compared to a multidimensional scheme (Harris *et al.*, 2011).

Crucial in the flux integral method is the type of interpolation used to approximate the scalar field within the cells that discretize the domain. High-order schemes require the use of high-order interpolations, which can degrade the monotonicity of the solution where the gradients are poorly resolved. This degradation leads to unphysical over- and undershooting, and oscillations of the solution near its extrema. These detrimental effects can, however, be avoided and monotonicity can be enforced by use of a flux-limiter scheme, for example, the popular flux-corrected transport scheme proposed by Zalesak (1979). Complementing the flux integral method with a flux-corrected

transport scheme (Zalesak, 2005) allows to correct the value of the fluxes after they have been computed and, consequently, enforce the monotonicity of the solution. Thuburn (1996) proposed a multidimensional implementation of a flux-limiter scheme, which is computationally less expensive than Zalesak's method, but has more stringent stability restrictions (Mittal & Skamarock, 2010).

The main disadvantage of the flux-limiter schemes is that they tend to smooth the solution, consequently degrading its global accuracy. To overcome this disadvantage, Blossey & Durran (2008) proposed an algorithm that only activates the flux-limiter in regions where the gradients are poorly resolved. Their algorithm preserves the global accuracy of the flux integral method at the expense of negligible violations in the monotonicity of the solution. Recently, Harris *et al.* (2011) confirmed the effectiveness of the selective limiter scheme in conjunction with a two-dimensional conservative semi-Lagrangian method.

We leverage and extend the schemes and results discussed above to derive and implement a highly accurate, fully three-dimensional, cost-effective flux integral method, named 3DFLUX, for the solution of the scalar transport equation. 3DFLUX is fully explicit and multidimensional. The latter property guarantees that 3DFLUX is free of splitting errors and results in a better convergence rate of the numerical errors when compared to widely used one-dimensional techniques, such as the piecewise parabolic method (PPM) (Colella & Woodward, 1984), the weighted essentially non-oscillatory (WENO) method (Liu *et al.*, 1994), and the recently-proposed jet scheme (Nave *et al.*, 2010; Seibold *et al.*, 2012), which is based on the level-set method. 3DFLUX is nominally third-order in space and second-order in time. It generates low numerical dissipation and anisotropic distortion (Leonard *et al.*, 1993). 3DFLUX

allows the solution of problems of practical interest at a reasonable computational cost.

In the derivation of 3DFLUX, we restrict the value of the Courant number to be one or less because our research focuses on the advection-diffusion of the smaller scales of turbulent flows. However, there are no conceptual difficulties in extending 3DFLUX to Courant numbers greater than one to target applications in atmospheric science. We characterize the convergence rate, accuracy and cost-efficiency of 3DFLUX by running several multidimensional tests: a two-dimensional purely advective mixing/unmixing problem (Seibold *et al.*, 2012), the rotation of a slotted cylinder (Orszag, 1971), a two-dimensional purely advective unsteady deformational flow (Blossey & Durran, 2008), and a three-dimensional advection-diffusion problem. We show that at the highest possible Courant number — one in our implementation — 3DFLUX results in a noticeably higher accuracy and better cost-efficiency than the currently available numerical schemes having the same convergence rate. We also show that, at low enough Courant numbers, 3DFLUX unexpectedly appears to be superconvergent. Lastly, we complete the validation of 3DFLUX by simulating an experiment in which a scalar (temperature) is released from a heated line source in a fully developed turbulent channel flow. The statistics produced by 3DFLUX are in remarkable agreement with those measured in the experiment (Lavertu & Mydlarski, 2005).

The remainder of this paper is organized as follows: In section 2.4, a detailed derivation of the numerical method is presented. In section 2.5, two- and three-dimensional numerical tests are performed to validate the performance of our scheme, including a three-dimensional direct numerical simulation (DNS)

of a thermal plume in a fully turbulent channel flow that exemplifies the potential of our scheme to simulate flows of interest in engineering applications. Lastly, conclusions are presented in section 2.6.

2.4 Numerical Method

The equation governing the unsteady, three-dimensional transport of a scalar property, ϕ, can be written in a generic form as

$$\frac{\partial(\rho\phi)}{\partial t} + \vec{\nabla} \cdot (\rho\vec{u}\phi) = \vec{\nabla} \cdot (\Gamma\vec{\nabla}\phi) + S, \tag{2.1}$$

where ρ is a physical property of the system, $\vec{u} = (u, v, w)$ is the advecting velocity vector field, Γ is a diffusion coefficient of the system, and S represents the source (or sink) terms.

Equation (2.1) states that the rate of change of ϕ depends on the balance between advective transport, diffusive transport and source or sink terms. For the sake of clarity, we limit our discussion to the well known advection-diffusion equation governing the time evolution of the internal energy of a flow of a simple compressible substance, where ρ is the fluid density, ϕ is the temperature, $\Gamma = \kappa/c_p$, where κ is the thermal conductivity of the fluid and c_p is its specific heat capacity at constant pressure, and $S = \dot{q}/c_p$, where $\dot{q}$ quantifies the volumetric heat source/sink terms. Obviously, any scalar transport equation that can be cast in the form of (2.1) can be solved using the algorithm presented herein.

The density, ρ, and the coefficient of diffusion, Γ, of the fluid are related to the fluid temperature, ϕ, and the fluid pressure, p, by the constitutive equations, i.e. $\rho = \rho(\phi, p)$ and $\Gamma = \Gamma(\phi, p)$. These relations are usually non linear and often cause major difficulties in the solution of equation (2.1). Consequently, we restrict our attention to flow where ρ and Γ are constant. Under

these assumptions, the equation (2.1) is fully determined and still correctly models the evolution of a scalar in a wide range of engineering applications.

2.4.1 Discretization of the scalar transport equation

In the flux integral method, the computational domain is discretized with a number of non-overlapping control volumes, or computational cells, of size $\Delta V = \Delta x \times \Delta y \times \Delta z$. The grid nodes are cell-centered and the value of the scalar property, ϕ, at a node represents the average value of ϕ within the control volume ΔV. The components of the velocity field are represented on three different staggered grids so that the value of the three components of the velocity, u, v and w, are stored at the center of each side of the control volume. The flux integral method solves equation (2.1) by estimating the fluxes exchanged between adjacent cells. With a staggered arrangement, the velocity components are directly available at the cell-sides, where they are needed for the calculation of the fluxes. This method is a multidimensional finite volume method.

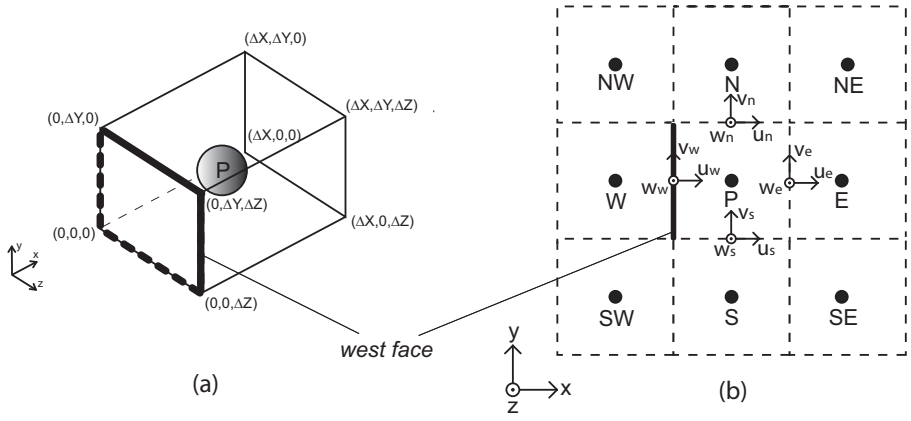

Figure 2–1: (a) Computational cell of volume ΔV. (b) Arrangement of the grid nodes and the staggered velocity components in a two-dimensional view of the three-dimensional grid.

To implement the flux integral method, we need to introduce a nomenclature (Patankar, 1980) to designate the location of the cell center and cell sides. Let us focus on a grid point P, as shown in figure 2–1. Each neighbouring grid

point of P is identified by one or more of the following six capital letters: W, E, N, S, B, F. These letters identify the nodes at the west, east, north, south, back and front sides of the computational cell containing P, respectively. For example, the node W is the closest neighbour to P located in the negative x-direction, the node SW is the closest neighbor to P located in the negative x- and y-directions, the node WW is the second closest neighbour to P located in the negative x-direction, and so on. The same lowercase letters are used to identify the sides of the computational cell, or control volume, containing the grid point P. For example, ϕ_w and u_w represent, respectively, the average values of the scalar ϕ and the u-component of the velocity field on the west side of the cell P.

The scalar transport equation (2.1) can be written in integral form as follows

$$\int_{\Delta t}\int_{\Delta V} \frac{\partial(\rho\phi)}{\partial t}\,\mathrm{d}V\mathrm{d}t = \int_{\Delta t}\int_{\Delta V}\left[-\vec{\nabla}\cdot(\rho\vec{u}\phi)+\vec{\nabla}\cdot(\Gamma\vec{\nabla}\phi)+S\right]\,\mathrm{d}V\mathrm{d}t, \quad (2.2)$$

where ΔV is the volume of the computational cell. Since the value of ϕ at the center of a cell is the average of ϕ within that cell, the left-hand side of (2.2) can be written as

$$\int_{\Delta t}\int_{\Delta V} \frac{\partial(\rho\phi)}{\partial t}\,\mathrm{d}V\mathrm{d}t = \rho(\phi^{t+\Delta t}-\phi^{t})\Delta V. \quad (2.3)$$

Since the flow is assumed to be of constant density, the first term on the right-hand side of (2.2) can be written as

$$\begin{aligned}-\int_{\Delta t}\int_{\Delta V}\left[\frac{\partial(\rho u\phi)}{\partial x}+\frac{\partial(\rho v\phi)}{\partial y}+\frac{\partial(\rho w\phi)}{\partial z}\right]\,\mathrm{d}V\mathrm{d}t =& \Delta y\Delta z\int_{\Delta t}(\rho u_w\phi_w-\rho u_e\phi_e)\,\mathrm{d}t\\ &+\Delta x\Delta z\int_{\Delta t}(\rho v_s\phi_s-\rho v_n\phi_n)\,\mathrm{d}t\\ &+\Delta x\Delta y\int_{\Delta t}(\rho w_b\phi_b-\rho w_f\phi_f)\,\mathrm{d}t.\end{aligned} \quad (2.4)$$

Similarly, the second term on the right-hand side of (2.2) can be rewritten as

$$\int_{\Delta t}\int_{\Delta V}\left[\frac{\partial}{\partial x}\left(\Gamma\frac{\partial\phi}{\partial x}\right)+\frac{\partial}{\partial y}\left(\Gamma\frac{\partial\phi}{\partial y}\right)+\frac{\partial}{\partial z}\left(\Gamma\frac{\partial\phi}{\partial z}\right)\right]\mathrm{d}V\mathrm{d}t = \Delta y\Delta z\int_{\Delta t}\Gamma\left(\left.\frac{\partial\phi}{\partial x}\right|_e-\left.\frac{\partial\phi}{\partial x}\right|_w\right)\mathrm{d}t + \Delta x\Delta z\int_{\Delta t}\Gamma\left(\left.\frac{\partial\phi}{\partial y}\right|_n-\left.\frac{\partial\phi}{\partial y}\right|_s\right)\mathrm{d}t + \Delta x\Delta y\int_{\Delta t}\Gamma\left(\left.\frac{\partial\phi}{\partial z}\right|_f-\left.\frac{\partial\phi}{\partial z}\right|_b\right)\mathrm{d}t. \tag{2.5}$$

Note that the advective and diffusive terms on the west face of the control volume can be rewritten as

$$\Delta y\Delta z\int_{\Delta t}\left(\rho u_w\phi_w\right)\,\mathrm{d}t=\langle\rho u_w\phi_w\rangle\,\Delta y\Delta z\Delta t, \tag{2.6}$$

and

$$\Delta y\Delta z\int_{\Delta t}-\Gamma\left.\frac{\partial\phi}{\partial x}\right|_w\,\mathrm{d}t=\left\langle-\Gamma\left.\frac{\partial\phi}{\partial x}\right|_w\right\rangle\Delta y\Delta z\Delta t, \tag{2.7}$$

where angular brackets $\langle\cdot\rangle$ represent the time average over a time interval Δt. Finally, the last term on the right-hand side of (2.2), the source term, can be rewritten as

$$\int_{\Delta t}\int_{\Delta V}S\;\mathrm{d}V\mathrm{d}t=\langle S\rangle\,\Delta V\Delta t. \tag{2.8}$$

Hence, the equation (2.2) can be rewritten in flux form as follows

$$\phi_P^{t+\Delta t}\;=\;\phi_P^t+\mathrm{f}_w-\mathrm{f}_e+\mathrm{f}_s-\mathrm{f}_n+\mathrm{f}_b-\mathrm{f}_f+\langle S\rangle\,\frac{\Delta t}{\rho}, \tag{2.9}$$

where the terms f_w, f_e, f_s, f_n, f_b and f_f, denote the sum of the advective and the diffusive fluxes across the west, east, south, north, front and back sides of

the control volume P, respectively. f_w, f_s and f_b are defined as

$$\begin{aligned}
\mathrm{f}_w &= \frac{\Delta t \Delta y \Delta z}{\rho \Delta V}\left(\langle \rho u_w \phi_w \rangle - \left\langle \Gamma \left.\frac{\partial \phi}{\partial x}\right|_w \right\rangle\right) \\
\mathrm{f}_s &= \frac{\Delta t \Delta x \Delta z}{\rho \Delta V}\left(\langle \rho u_s \phi_s \rangle - \left\langle \Gamma \left.\frac{\partial \phi}{\partial y}\right|_s \right\rangle\right) \\
\mathrm{f}_b &= \frac{\Delta t \Delta x \Delta y}{\rho \Delta V}\left(\langle \rho u_b \phi_b \rangle - \left\langle \Gamma \left.\frac{\partial \phi}{\partial z}\right|_b \right\rangle\right).
\end{aligned} \tag{2.10}$$

Equation (2.9) is strictly conservative when the flux across two adjacent control volumes is the same. Consequently, for a given control volume, only the fluxes f_w, f_s and f_b have to be calculated as the three remaining fluxes, i.e. f_e, f_n and f_f, are directly determined as follows

$$\begin{aligned}
(\mathrm{f}_e)_{ijk} &= (\mathrm{f}_w)_{i'jk} \\
(\mathrm{f}_n)_{ijk} &= (\mathrm{f}_s)_{ij'k} \\
(\mathrm{f}_f)_{ijk} &= (\mathrm{f}_b)_{ijk'}
\end{aligned} \tag{2.11}$$

where the indices i, j and k represent the components along the coordinate axes x, y and z, respectively, and where $i' = i + 1$, $j' = j + 1$ and $k' = k + 1$. Note that equation (2.9) is equivalent to the two-step Lax-Wendroff scheme, i.e. a second-order in time method, when the fluxes are computed at the intermediate time step $t + \Delta t/2$ (Press *et al.*, 2007, p.1040).

Note that in equations (2.10), the values of the scalar at the side of a cell, i.e ϕ_w, ϕ_s and ϕ_b, and the gradients of ϕ normal to the side of a cell, i.e $\partial\phi/\partial x|_w$, $\partial\phi/\partial y|_s$ and $\partial\phi/\partial z|_b$, have to be computed before performing the time average of the fluxes. The values of ϕ and its gradients are unknown at the sides of the control volume, but they can be interpolated from the values of ϕ known at the center of the cells. The computation of the fluxes is presented in detail in the next subsections.

2.4.2 Piecewise polynomial interpolation of face quantities

To compute the fluxes, the unknown values of the scalar and its gradients at the sides of a cell can be obtained by interpolating the known values of ϕ at the center of the surrounding cells. One of the most common and simple methods is piecewise linear interpolation. This interpolation leads to very efficient second-order schemes whose applicability, however, is limited to diffusion-dominated problems. In fact, these second-order schemes generate questionable solutions, which are affected by spurious oscillations when the magnitude of the advective terms is greater than that of the diffusive ones. In fluid mechanics, for example, the Péclet number quantifies the ratio of the advective and diffusive terms. Hence, the validity of such second-order schemes is limited to simulations of fluid flows where the local Péclet number, i.e. Péclet number based on the local velocity, diffusivity, and cell dimensions, is lower than 2 (Patankar, 1980).

The limitations of such second-order schemes can be overcome using upwind schemes, such as the popular first-order upwind schemes that use piecewise constant interpolation, where the unknown value of ϕ at any given side of a cell is set equal to the known value of ϕ at the center of the adjacent upstream cell. In other words, the west value ϕ_w is taken equal to ϕ_W when u_w is positive. Otherwise it is equal to ϕ_P (see figure 2–1). Despite their simplicity, speed and robustness, first-order schemes are usually not adequate for accurate simulations because they exhibit high numerical diffusion and poor convergence properties in addition to producing erroneous solutions when the flow is not aligned with the grid lines (Versteeg & Malalasekera, 2007; Nassehi & Das, 2007).

Higher-order upwind schemes have subsequently been introduced over the years, such as the popular Quadratic Upstream Interpolation for Convective

Kinematics with Estimated Streaming Terms (QUICKEST) scheme, proposed by Leonard (1979). QUICKEST is based on a quadratic polynomial interpolation which leads to a third-order scheme. It has a limitation, however, as the interpolation performed by QUICKEST is locally one-dimensional. As a result, QUICKEST produces anisotropically distorted results when used to solve multidimensional problems (Leonard *et al.*, 1993). To avoid these detrimental effects, Leonard *et al.* (1995) proposed a Uniformly Third-Order Polynomial Interpolation Algorithm (UTOPIA) implemented with a flux integral method. Leonard *et al.* (1995) characterized the performance of UTOPIA by solving a purely two-dimensional advective problem: the transport of a Gaussian bell in a rotating flow. Subsequently, Leveque (1996) proposed a three-dimensional scheme, equivalent to UTOPIA, for solving purely advective problems.

Over the years, flux-based methods have been used for atmospheric transport and chemical models (Jakobsen, 2008). State-of-the-art solvers, such as COCO (CCSR Ocean Component Model), developed by the Center for Climate System Research (Hasumi & Daigaku, 2006), combine UTOPIA and QUICKEST to simulate ocean circulation and transport. More specifically, COCO separately solves the two-dimensional planar advection using UTOPIA, the vertical advection using QUICKEST and diffusion using a second-order, finite central difference scheme. This awkward combination of algorithms has been devised to circumvent the complexity of implementing UTOPIA in three-dimensions.

Leveraging Leonard's work (Leonard *et al.*, 1995), this article provides the reader with a detailed derivation and a careful validation of a new, fully three-dimensional, flux integral solver for the scalar transport equation. Our solver (3DFLUX) is third-order accurate under the assumption that the fluid properties are constant.

The exact solution of the scalar transport equation (2.1), $\phi = \phi(x, y, z, t)$, is discretized over a number of cells covering the computational domain. At any time t, the value stored at the center of a cell is the average of $\phi(x, y, z, t)$ over the volume of the cell. A three-dimensional piecewise quadratic interpolation is used to calculate the fluxes of the scalar across the sides of a cell. The exact solution, at each time step, is approximated within each cell by a quadratic polynomial of the form

$$\psi(x, y, z) = \sum_{i=0}^{2} \sum_{j=0}^{2} \sum_{k=0}^{2} c_{ijk} x^i y^j z^k, \tag{2.12}$$

where c_{ijk} are ten unknown coefficients. To determine these coefficients at each time step, we impose that the average value of the polynomial ψ and its first-order, second-order and cross derivatives are equal to the value of the average solution at the center of the cell and its corresponding derivatives.

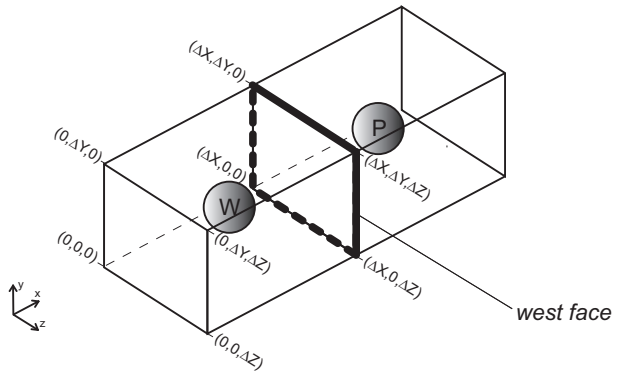

Figure 2–2: Computational cells W and P.

As an example, we present the ten conditions used to determine the coefficients, c_{ijk}, of the interpolant, ψ_W, within the west cell (see figure 2–2), where the subscript W indicates the name of the cell. As a first condition, we impose the average value of the interpolant over the west cell to be equal to the value of the average of the scalar over the west cell

$$\frac{1}{\Delta V}\int_V \psi_W \,\mathrm{d}V = \sum_{i=0}^{2}\sum_{j=0}^{2}\sum_{k=0}^{2} c_{ijk}\left(\frac{\Delta x}{2}\right)^i\left(\frac{\Delta y}{2}\right)^j\left(\frac{\Delta z}{2}\right)^k = \phi_W, \qquad (2.13)$$

where $(\Delta x/2, \Delta y/2, \Delta z/2)$ are the coordinates of the center of the west cell (see figure 2–2). Similarly, the remaining nine conditions are obtained imposing that the average value of the first, second and cross derivatives of the interpolant over the west cell are equal to the corresponding derivatives of the average of the scalar over the west cell. We have

$$\frac{1}{\Delta V}\int_V \left.\frac{\partial\psi}{\partial x}\right|_W \mathrm{d}V = \sum_{i=0}^{2}\sum_{j=0}^{2}\sum_{k=0}^{2} i c_{ijk}\left(\frac{\Delta x}{2}\right)^{i-1}\left(\frac{\Delta y}{2}\right)^j\left(\frac{\Delta z}{2}\right)^k = \left.\frac{\partial\phi}{\partial x}\right|_W$$
$$\frac{1}{\Delta V}\int_V \left.\frac{\partial\psi}{\partial y}\right|_W \mathrm{d}V = \sum_{i=0}^{2}\sum_{j=0}^{2}\sum_{k=0}^{2} j c_{ijk}\left(\frac{\Delta x}{2}\right)^{i}\left(\frac{\Delta y}{2}\right)^{j-1}\left(\frac{\Delta z}{2}\right)^k = \left.\frac{\partial\phi}{\partial y}\right|_W$$
$$\frac{1}{\Delta V}\int_V \left.\frac{\partial\psi}{\partial z}\right|_W \mathrm{d}V = \sum_{i=0}^{2}\sum_{j=0}^{2}\sum_{k=0}^{2} k c_{ijk}\left(\frac{\Delta x}{2}\right)^{i}\left(\frac{\Delta y}{2}\right)^{j}\left(\frac{\Delta z}{2}\right)^{k-1} = \left.\frac{\partial\phi}{\partial z}\right|_W$$

$$\frac{1}{\Delta V}\int_V \left.\frac{\partial^2\psi}{\partial x^2}\right|_W \mathrm{d}V = \sum_{i=0}^{2}\sum_{j=0}^{2}\sum_{k=0}^{2} i^2 c_{ijk}\left(\frac{\Delta x}{2}\right)^{i-2}\left(\frac{\Delta y}{2}\right)^j\left(\frac{\Delta z}{2}\right)^k = \left.\frac{\partial^2\phi}{\partial x^2}\right|_W$$
$$\frac{1}{\Delta V}\int_V \left.\frac{\partial^2\psi}{\partial y^2}\right|_W \mathrm{d}V = \sum_{i=0}^{2}\sum_{j=0}^{2}\sum_{k=0}^{2} j^2 c_{ijk}\left(\frac{\Delta x}{2}\right)^{i}\left(\frac{\Delta y}{2}\right)^{j-2}\left(\frac{\Delta z}{2}\right)^k = \left.\frac{\partial^2\phi}{\partial y^2}\right|_W$$
$$\frac{1}{\Delta V}\int_V \left.\frac{\partial^2\psi}{\partial z^2}\right|_W \mathrm{d}V = \sum_{i=0}^{2}\sum_{j=0}^{2}\sum_{k=0}^{2} k^2 c_{ijk}\left(\frac{\Delta x}{2}\right)^{i}\left(\frac{\Delta y}{2}\right)^{j}\left(\frac{\Delta z}{2}\right)^{k-2} = \left.\frac{\partial^2\phi}{\partial z^2}\right|_W$$

$$\frac{1}{\Delta V}\int_V \left.\frac{\partial^2\psi}{\partial x\partial y}\right|_W \mathrm{d}V = \sum_{i=0}^{2}\sum_{j=0}^{2}\sum_{k=0}^{2} ij c_{ijk}\left(\frac{\Delta x}{2}\right)^{i-1}\left(\frac{\Delta y}{2}\right)^{j-1}\left(\frac{\Delta z}{2}\right)^k = \left.\frac{\partial^2\phi}{\partial x\partial y}\right|_W$$
$$\frac{1}{\Delta V}\int_V \left.\frac{\partial^2\psi}{\partial x\partial z}\right|_W \mathrm{d}V = \sum_{i=0}^{2}\sum_{j=0}^{2}\sum_{k=0}^{2} ik c_{ijk}\left(\frac{\Delta x}{2}\right)^{i-1}\left(\frac{\Delta y}{2}\right)^{j}\left(\frac{\Delta z}{2}\right)^{k-1} = \left.\frac{\partial^2\phi}{\partial x\partial z}\right|_W$$
$$\frac{1}{\Delta V}\int_V \left.\frac{\partial^2\psi}{\partial y\partial z}\right|_W \mathrm{d}V = \sum_{i=0}^{2}\sum_{j=0}^{2}\sum_{k=0}^{2} jk c_{ijk}\left(\frac{\Delta x}{2}\right)^{i}\left(\frac{\Delta y}{2}\right)^{j-1}\left(\frac{\Delta z}{2}\right)^{k-1} = \left.\frac{\partial^2\phi}{\partial y\partial z}\right|_W, \qquad (2.14)$$

where $\partial\phi/\partial x|_W$, $\partial\phi/\partial y|_W$, $\partial\phi/\partial z|_W$, $\partial^2\phi/\partial x^2|_W$, $\partial^2\phi/\partial y^2|_W$, $\partial^2\phi/\partial z^2|_W$, $\partial^2\phi/\partial x\partial y|_W$, $\partial^2\phi/\partial y\partial z|_W$, $\partial^2\phi/\partial x\partial z|_W$ are the first-order, second-order and cross-derivatives of the average value of the scalar, ϕ.

The ten equations (2.13) and (2.14) yield a 10×10 non-singular system of equations. This system can be cast in the matrix-vector form $A \cdot \vec{c} = \vec{b}$, where A is the Vandermonde matrix, $\vec{c}$ the coefficients vector, and $\vec{b}$ the vector of conditions. The inverse coefficients matrix (A^{-1}) can be pre-computed. It has the form

$$\begin{pmatrix}
1 & -\frac{\Delta x}{2} & -\frac{\Delta y}{2} & -\frac{\Delta z}{2} & \frac{\Delta x^2}{12} & \frac{\Delta y^2}{12} & \frac{\Delta z^2}{12} & \frac{\Delta x\Delta y}{4} & \frac{\Delta x\Delta z}{4} & \frac{\Delta y\Delta z}{4} \\
0 & 1 & 0 & 0 & -\frac{\Delta x}{2} & 0 & 0 & -\frac{\Delta y}{2} & -\frac{\Delta z}{2} & 0 \\
0 & 0 & 0 & 0 & \frac{1}{2} & 0 & 0 & 0 & 0 & 0 \\
0 & 0 & 1 & 0 & 0 & -\frac{\Delta y}{2} & 0 & -\frac{\Delta x}{2} & 0 & -\frac{\Delta z}{2} \\
0 & 0 & 0 & 0 & 0 & 0 & 0 & 1 & 0 & 0 \\
0 & 0 & 0 & 0 & 0 & \frac{1}{2} & 0 & 0 & 0 & 0 \\
0 & 0 & 0 & 1 & 0 & 0 & -\frac{\Delta z}{2} & 0 & -\frac{\Delta y}{2} & -\frac{\Delta x}{2} \\
0 & 0 & 0 & 0 & 0 & 0 & 0 & 0 & 1 & 0 \\
0 & 0 & 0 & 0 & 0 & 0 & 0 & 0 & 0 & 1 \\
0 & 0 & 0 & 0 & 0 & 0 & \frac{1}{2} & 0 & 0 & 0
\end{pmatrix}. \quad (2.15)$$

The ten coefficients defining the three-dimensional interpolant can then be simply obtained by multiplying the inverse matrix by the vector

$$\left[\phi_W, \left.\frac{\partial\phi}{\partial x}\right|_W, \left.\frac{\partial\phi}{\partial y}\right|_W, \left.\frac{\partial\phi}{\partial z}\right|_W, \left.\frac{\partial^2\phi}{\partial x^2}\right|_W, \left.\frac{\partial^2\phi}{\partial y^2}\right|_W, \left.\frac{\partial^2\phi}{\partial z^2}\right|_W, \left.\frac{\partial^2\phi}{\partial x\partial y}\right|_W, \left.\frac{\partial^2\phi}{\partial x\partial z}\right|_W, \left.\frac{\partial^2\phi}{\partial y\partial z}\right|_W\right]^T. \quad (2.16)$$

The components of the above vector, i.e. the derivatives of the average value, ϕ_W, at the center of the west cell are approximated using fourth-order centered finite difference formulas. The derivatives of ϕ_W for the west cell are

expressed in the following form

$$\left.\frac{\partial\phi}{\partial x}\right|_W = \frac{1}{12\Delta x}\left(\phi_{WWW} - 8\phi_{WW} + 8\phi_P - \phi_E\right) + O(\Delta x^4)$$
$$\left.\frac{\partial\phi}{\partial y}\right|_W = \frac{1}{12\Delta y}\left(\phi_{SSW} - 8\phi_{SW} + 8\phi_{NW} - \phi_{NNW}\right) + O(\Delta y^4)$$
$$\left.\frac{\partial\phi}{\partial z}\right|_W = \frac{1}{12\Delta z}\left(\phi_{BBW} - 8\phi_{BW} + 8\phi_{FW} - \phi_{FFW}\right) + O(\Delta z^4)$$

$$\left.\frac{\partial^2\phi}{\partial x^2}\right|_W = \frac{1}{12\Delta x^2}\left(-\phi_{WWW} + 16\phi_{WW} - 30\phi_W + 16\phi_P - \phi_E\right) + O(\Delta x^4)$$
$$\left.\frac{\partial^2\phi}{\partial y^2}\right|_W = \frac{1}{12\Delta y^2}\left(-\phi_{SSW} + 16\phi_{SW} - 30\phi_W + 16\phi_{NW} - \phi_{NNW}\right) + O(\Delta y^4)$$
$$\left.\frac{\partial^2\phi}{\partial z^2}\right|_W = \frac{1}{12\Delta z^2}\left(-\phi_{BBW} + 16\phi_{BW} - 30\phi_W + 16\phi_{FW} - \phi_{FFW}\right) + O(\Delta z^4)$$

$$\left.\frac{\partial^2\phi}{\partial x\partial y}\right|_W = \frac{1}{4\Delta x\Delta y}\left(\phi_N + \phi_{SWW} - \phi_{NWW} - \phi_S\right) + O(\Delta x^2\Delta y^2)$$
$$\left.\frac{\partial^2\phi}{\partial x\partial z}\right|_W = \frac{1}{4\Delta x\Delta z}\left(\phi_F + \phi_{BWW} - \phi_{FWW} - \phi_B\right) + O(\Delta x^2\Delta z^2)$$
$$\left.\frac{\partial^2\phi}{\partial y\partial z}\right|_W = \frac{1}{4\Delta y\Delta z}\left(\phi_{FNW} + \phi_{BSW} - \phi_{FSW} - \phi_{BNW}\right) + O(\Delta y^2\Delta z^2)\,. \quad (2.17)$$

The above equations require the values of the scalar at twenty-five distinct nodes, see figure 2–3. Of course, the use of fourth-order formulas does not improve the convergence rate of our quadratic interpolation but, as shown by Russell (1995), considerably improves its accuracy.

The stencils shown in figure 2–3 represent the collection of the nodes used to compute the polynomial interpolants ψ_W and ψ_P. On the one hand, a stencil of twenty-five nodes could be considered as unnecessarily large, making their software implementation complex and computationally intensive. On the other hand, such stencil leads to high-order interpolations. The recent emergence of affordable multi-core processors and the constantly increasing

size of memory chips make the use of large stencils realistic, as our multi-threaded implementation of 3DFLUX shows.

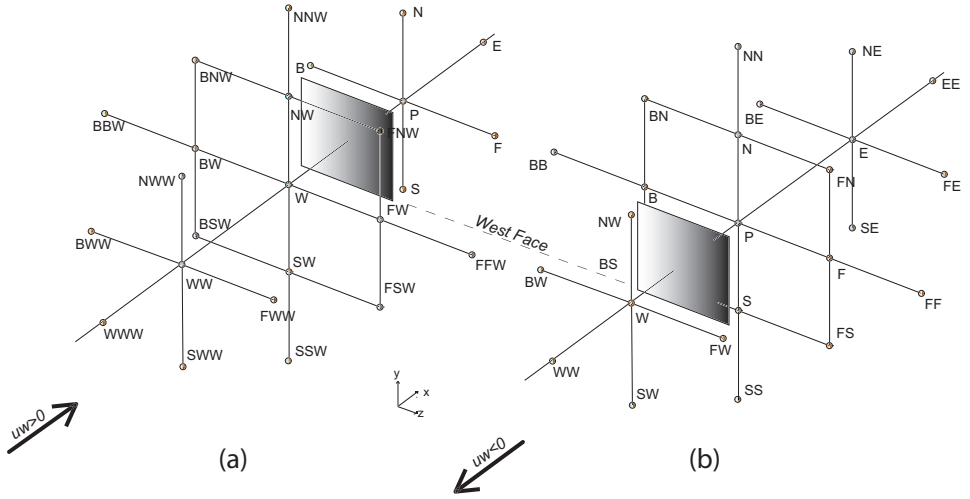

Figure 2–3: Stencils used to compute the polynomial interpolant within the cell W (a) and within the cell P (b), respectively. The polynomial interpolants in the cells W and P are used to estimate the values of the fluxes at the west face when $u_w > 0$ and $u_w < 0$, respectively.

Finally, the values of the scalar and its normal gradients, at the side of a cell are estimated by averaging the polynomial interpolant of the upstream cell over the side area of the cell. For example, the value at the west side is evaluated by averaging the polynomial interpolant, ψ_W, over the area of the west side, when u_w is positive, or by averaging the polynomial interpolant ψ_P, when u_w is negative, i.e.

$$\phi_w = \begin{cases} \dfrac{1}{\Delta z \Delta y} \displaystyle\int_{\Delta z} \int_{\Delta y} \psi_W(\Delta x, y, z)\ \mathrm{d}y\mathrm{d}z, u_w > 0 \\ \dfrac{1}{\Delta z \Delta y} \displaystyle\int_{\Delta z} \int_{\Delta y} \psi_P(\Delta x, y, z)\ \mathrm{d}y\mathrm{d}z, u_w < 0. \end{cases} \tag{2.18}$$

Note that ψ_W and ψ_P are determined using the stencil of nodes shown on figure 2–3(a) and 2–3(b) respectively.

Similarly, the gradient normal to the west side is computed as follows

$$\left.\frac{\partial\phi}{\partial x}\right|_w = \begin{cases} \dfrac{1}{\Delta z\Delta y}\displaystyle\int_{\Delta z}\int_{\Delta y} \left.\dfrac{\partial\psi(\Delta x,y,z)}{\partial x}\right|_W \mathrm{d}y\mathrm{d}z, & u_w > 0 \\ \dfrac{1}{\Delta z\Delta y}\displaystyle\int_{\Delta z}\int_{\Delta y} \left.\dfrac{\partial\psi(\Delta x,y,z)}{\partial x}\right|_P \mathrm{d}y\mathrm{d}z, & u_w < 0. \end{cases} \tag{2.19}$$

The polynomial interpolants ψ_P, ψ_S and ψ_B are computed following a similar procedure. Note that this polynomial can also be obtained by an appropriate permutation of the inverse coefficient matrix (2.15) and the components of the vector (2.17).

2.4.3 Computation of the time-averaged fluxes

The flux integral method combines both Eulerian and Lagrangian point of views – the solution of the scalar field is discretized in space on an Eulerian grid, whereas it is discretized in time in a Lagrangian frame of reference. This interesting semi-Lagrangian approach was first introduced by Courant *et al.* (1952) and, since then, widely used for the simulation of the transport equation (Staniforth & Côté, 1991; Xu *et al.*, 2002; Falcone & Ferretti, 2002; Paoli *et al.*, 2006). Semi-Lagrangian schemes allow for larger time steps and have better stability properties than the classical Eulerian explicit and semi-implicit schemes.

We derive the time-averaged advective and diffusive fluxes using a Lagrangian description of the flow. For simplicity, we limit our derivation to the fluxes across the west face of the cell P when the three components of the velocity field are oriented in their positive directions, i.e. $u_w > 0$, $v_w > 0$ and $w_w > 0$. Furthermore, we also limit our implementation to Courant numbers ($c_x = u_w\Delta t/\Delta x$, $c_y = v_w\Delta t/\Delta y$ and $c_z = w_w\Delta t/\Delta z$) less than or equal to unity. The time average of the advective and the diffusive fluxes over a time

interval Δt and across the west face are expressed as follows

$$\langle \rho u_w \phi_w \rangle = \frac{1}{\Delta t} \int_0^{\Delta t} \rho u_w \phi_w \, \mathrm{d}t, \tag{2.20}$$

and

$$\left\langle \Gamma \left. \frac{\partial \phi}{\partial x} \right|_w \right\rangle = \frac{1}{\Delta t} \int_0^{\Delta t} \Gamma \left. \frac{\partial \phi}{\partial x} \right|_w \, \mathrm{d}t, \tag{2.21}$$

where ϕ_w and $\partial\phi/\partial x|_w$ are respectively the average value of the scalar and the average of its gradient at the west side of the cell P.

The scalar flux quantifies the rate of advection-diffusion of a scalar transported across the west face, that is, the amount of the scalar that passes through the west face per unit time. Consequently, the average of the advective and diffusive fluxes over a time interval Δt is, respectively, the average of the scalar properties $\rho u_w \phi$ and $\Gamma \, \partial\phi/\partial x|_w$ over the volume of fluid that crosses the west face in the time interval Δt.

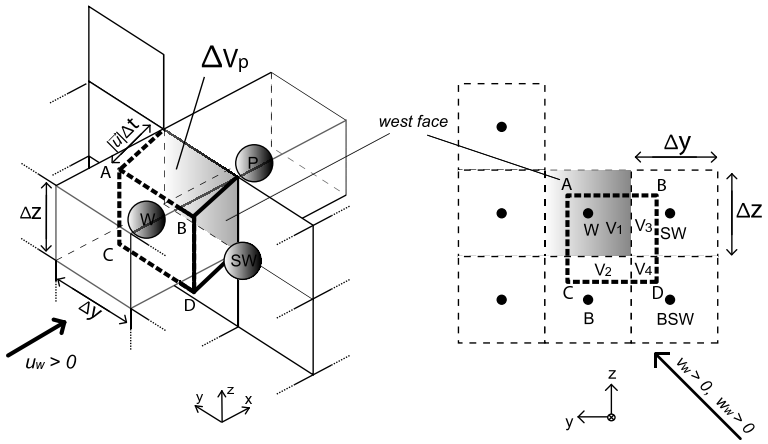

Figure 2–4: Approximation of the volume of fluid that traverses the west face in a time interval Δt.

As the velocity is assumed constant in the vicinity of the west face of the cell P, the volume of fluid that traverses the west face in a time interval Δt is approximated by a rectangular prism $\Delta V_p = u_w \Delta t \times \Delta y \times \Delta z$. This rectangular prism is a backwards-in-time projection over an interval Δt of the west face of the cell P, where the magnitude and the orientation of the projection is given

by the vector $-\vec{u}\Delta t$, i.e $(-u_w\Delta t, -v_w\Delta t, -w_w\Delta t)$, as shown in figure 2–4. Note that, as the transverse velocity components v_w and w_w are non-zero, the prism overlaps with several cells, i.e. cells W, B, SW and BSW. The volume fraction of fluid particles transported from each distinct cells into the cell P are the four sub-volumes V_1 to V_4 illustrated in figure 2–4. The coordinates of the vertices A, B, C and D are determined by integrating backward in time over an interval Δt the equation of the motion of the fluid particles located at the four corners of the west face of the cell P. The equation of motion of a fluid particle located at $\vec{x}$ is

$$\frac{\mathrm{d}\vec{x}}{\mathrm{d}t} = \vec{u}\left(\vec{x}, t\right), \tag{2.22}$$

integrating it backward in time over a time interval Δt with the final conditions, $x(\Delta t) = \Delta x$, $y(\Delta t) = \Delta y$ and $z(\Delta t) = \Delta z$, we have

$$\begin{cases} x(0) = \Delta x - u_w\Delta t \\ y(0) = \Delta y - v_w\Delta t = \Delta y + v_w\dfrac{x(0) - \Delta x}{u_w} \\ z(0) = \Delta z - w_w\Delta t = \Delta z + w_w\dfrac{x(0) - \Delta x}{u_w}. \end{cases} \tag{2.23}$$

The integral of the scalar quantity, $\rho u_w\phi(0)$, over the rectangular prism, ΔV_p, can be rewritten as

$$\begin{aligned} \int_{\Delta V_p} \rho u_w\phi(0)\ \mathrm{d}V_p \approx u_w \int_{x(0)}^{\Delta x} \Bigg(& \int_0^{z(0)} \int_0^{y(0)} \rho\psi_W\ \mathrm{d}y\mathrm{d}z \\ & + \int_0^{z(0)} \int_{y(0)}^{\Delta y} \rho\psi_B\ \mathrm{d}y\mathrm{d}z \\ & + \int_{z(0)}^{\Delta z} \int_0^{y(0)} \rho\psi_{SW}\ \mathrm{d}y\mathrm{d}z \\ & + \int_{z(0)}^{\Delta z} \int_{y(0)}^{\Delta y} \rho\psi_{BSW}\ \mathrm{d}y\mathrm{d}z \Bigg)\, \mathrm{d}x, \end{aligned} \tag{2.24}$$

where the four terms on the right-hand side represent the integration of the interpolants ψ_W, ψ_B, ψ_{SW} and ψ_{BSW} over the volumes V_1, V_2, V_3 and V_4,

respectively, and computed at $t = 0$. Note that the average value of $\rho u_w \phi$ over the prism ΔV_p represents the average flux across the west face during Δt, i.e.

$$\langle \rho u_w \phi_w \rangle = \frac{1}{u_w \Delta t \Delta y \Delta z} \int_{\Delta V_p} \rho u_w \phi(x, y, z, t) \mathrm{d}V_p. \tag{2.25}$$

To perform the above integration, we recall that the Lagrangian form of the transport equation (2.1) is

$$\frac{\mathrm{D}(\rho\phi)}{\mathrm{D}t} = \vec{\nabla} \cdot (\Gamma \vec{\nabla} \phi) + S, \tag{2.26}$$

where $D/\mathrm{D}t$ is the material derivative. Hence, the time evolution of the scalar $\rho\phi$ transported by a fluid particle is obtained by integrating equation (2.26) with respect to time $\tilde{t}$ from 0 to t as follows

$$\rho\phi(x, y, z, t) = \rho\phi(x, y, z, 0) + \int_0^t \left(\vec{\nabla} \cdot (\Gamma \vec{\nabla} \phi) + S \right) \mathrm{d}\tilde{t}. \tag{2.27}$$

Equation (2.27) states that the amount of $\rho\phi$ transported by a particle is not constant when it is subject to diffusion and source terms. Note that the value of $\phi(x, y, z, 0)$ is unknown, therefore it is approximated by the polynomial interpolant ψ computed at $t = 0$. The integral (2.27) can be easily computed because ψ is a quadratic polynomial and the source terms are constant within a cell during a time interval Δt. For instance, the integral over the volume V_1 can be approximated as

$$\int_0^t \left(\vec{\nabla} \cdot (\Gamma \vec{\nabla} \phi) + S \right) \mathrm{d}\tilde{t} \approx \left(\vec{\nabla} \cdot (\Gamma \vec{\nabla} \psi_W) + S \right) t. \tag{2.28}$$

Using equations (2.24), (2.27) and (2.28), we derive the time average of the advective fluxes as follows

$$\langle \rho u_w \phi_w \rangle = \frac{1}{\Delta t \Delta y \Delta z} \times \tag{2.29}$$

$$\begin{aligned}
&\Bigg\{ \int_0^{z(0)} \int_0^{y(0)} \left[\int_{x(0)}^{\Delta x} (\rho \psi_W)\, \mathrm{d}x + u_w \frac{\Delta t^2}{2} \left(\vec{\nabla} \cdot (\Gamma \vec{\nabla} \psi_W) + S_W \right) \right] \mathrm{d}y \mathrm{d}z \\
&+ \int_0^{z(0)} \int_{y(0)}^{\Delta y} \left[\int_{x(0)}^{\Delta x} (\rho \psi_B)\, \mathrm{d}x + u_w \frac{\Delta t^2}{2} \left(\vec{\nabla} \cdot (\Gamma \vec{\nabla} \psi_B) + S_B \right) \right] \mathrm{d}y \mathrm{d}z \\
&+ \int_{z(0)}^{\Delta z} \int_{y(0)}^{\Delta y} \left[\int_{x(0)}^{\Delta x} (\rho \psi_{BSW})\, \mathrm{d}x + u_w \frac{\Delta t^2}{2} \left(\vec{\nabla} \cdot (\Gamma \vec{\nabla} \psi_{BSW}) + S_{BSW} \right) \right] \mathrm{d}y \mathrm{d}z \\
&+ \int_{z(0)}^{\Delta z} \int_0^{y(0)} \left[\int_{x(0)}^{\Delta x} (\rho \psi_{SW})\, \mathrm{d}x + u_w \frac{\Delta t^2}{2} \left(\vec{\nabla} \cdot (\Gamma \vec{\nabla} \psi_{SW}) + S_{SW} \right) \right] \mathrm{d}y \mathrm{d}z \Bigg\},
\end{aligned} \tag{2.30}$$

where the subscripts identify the cells in which ψ and S are computed. Note that using equations (2.22) and (2.23), we transformed the integrals in x into integrals in t as follows

$$\begin{aligned}
\int_{x(0)}^{\Delta x} \left(\vec{\nabla} \cdot (\Gamma \vec{\nabla} \psi_W) + S \right) t \; \mathrm{d}x &= \int_0^{\Delta t} u_w \left(\vec{\nabla} \cdot (\Gamma \vec{\nabla} \psi_W) + S_W \right) t \mathrm{d}t \\
&= u_w \frac{\Delta t^2}{2} \left(\vec{\nabla} \cdot (\Gamma \vec{\nabla} \psi_W) + S_W \right).
\end{aligned} \tag{2.31}$$

To determine the average of the diffusive flux at the west face, we first take the derivative of equation (2.26) in the direction normal to the west face, i.e. in the x-direction, and we multiply it by Γ to obtain

$$\frac{\partial}{\partial x} \left[\Gamma \left(\frac{\mathrm{D}(\rho \phi)}{\mathrm{D}t} \right) \right] = \frac{\mathrm{D}}{\mathrm{D}t} \left(\rho \Gamma \frac{\partial \phi}{\partial x} \right) = \frac{\partial}{\partial x} \left[\Gamma \left(\vec{\nabla} \cdot (\Gamma \vec{\nabla} \phi) + S \right) \right]. \tag{2.32}$$

The above equation is then integrated with respect to time from 0 to t to express the time evolution of the quantity $\Gamma \partial \phi(x, y, z, t)/\partial x$

$$\Gamma \left(\frac{\partial \phi(x, y, z, t)}{\partial x} - \frac{\partial \phi(x, y, z, 0)}{\partial x} \right) = \frac{\Gamma}{\rho} \int_0^t \frac{\partial}{\partial x} \left[\vec{\nabla} \cdot (\Gamma \vec{\nabla} \phi + S) \right] \mathrm{d}t. \tag{2.33}$$

The polynomial interpolant, ψ, is used to approximate $\partial\phi(x,y,z,0)/\partial x$ which is unknown. Hence, noticing that for any quadratic polynomial ψ we have

$$\frac{\partial}{\partial x}\left[\vec{\nabla}\cdot(\Gamma\vec{\nabla}\psi)\right]=0, \tag{2.34}$$

and assuming that the source term is constant within a cell during an interval Δt, i.e. $\partial S/\partial x=0$, we derive the time average of the diffusive flux as follows

$$\begin{aligned}\left\langle \Gamma\left.\frac{\partial\phi}{\partial x}\right|_w\right\rangle = \frac{\Gamma}{\rho u_w\Delta t\Delta y\Delta z}\int_{x(0)}^{\Delta x}\Bigg[&\int_0^{z(0)}\int_0^{y(0)}\left(\rho\left.\frac{\partial\psi}{\partial x}\right|_W\right)\,\mathrm{d}y\mathrm{d}z\\ &+\int_0^{z(0)}\int_{y(0)}^{\Delta y}\left(\rho\left.\frac{\partial\psi}{\partial x}\right|_B\right)\,\mathrm{d}y\mathrm{d}z\\ &+\int_{z(0)}^{\Delta z}\int_0^{y(0)}\left(\rho\left.\frac{\partial\psi}{\partial x}\right|_{SW}\right)\,\mathrm{d}y\mathrm{d}z\\ &+\int_{z(0)}^{\Delta z}\int_{y(0)}^{\Delta y}\left(\rho\left.\frac{\partial\psi}{\partial x}\right|_{BSW}\right)\,\mathrm{d}y\mathrm{d}z\Bigg]\mathrm{d}x.\end{aligned} \tag{2.35}$$

Equations (2.30) and (2.35) respectively express the time averages of the advective and diffusive fluxes across the west face of the cell P. The average fluxes for the other faces and the other velocity orientations are determined using similar derivations.

2.4.4 Stability

3DFLUX is unconditionally stable when solving pure advection problems because it is strictly a flux integral method (see Leonard, 1997, for details). However, there exists a geometric constraint on the size of the rectangular prism used to perform the backward integration, as it cannot exceed the dimension of one cell (see figure 2–4). This constraint limits the range of the Courant numbers to

$$|c_x|\le 1,\ |c_y|\le 1,\ |c_z|\le 1. \tag{2.36}$$

In theory, one could relax the above constraint by allowing larger rectangular prisms when performing the backward integration. However, such a modification would render the implementation of our algorithm extremely complex.

3DFLUX is only conditionally stable when solving purely diffusive or advective-diffusive problems. To derive the stability constraint, we perform a von Neumann type of stability analysis for the case of constant coefficients, no source, periodic boundary conditions and homogeneous grid, i.e. $\Delta x = \Delta y = \Delta z = \Delta h$. Writing the solution at node P and time t in a wave form

$$\phi_p^t = e^{at} e^{i(k_1 x + k_2 y + k_3 z)}, \tag{2.37}$$

where a is a constant, (k_1, k_2, k_3) are the wavenumbers in the x-, y- and z-directions, respectively, $i = \sqrt{-1}$, and substituting equation (2.37) into the discretized equation (2.9), we obtain

$$e^{a\Delta t} = 1 + \frac{1}{e^{at} e^{i(k_1 x + k_2 y + k_3 z)}} \left[(\mathrm{f}_w - \mathrm{f}_e) + (\mathrm{f}_s - \mathrm{f}_n) + (\mathrm{f}_b - \mathrm{f}_f) \right], \tag{2.38}$$

where $e^{a\Delta t} = \phi_p^{t+\Delta t} / \phi_p^t = G$ is called the complex amplitude ratio. The necessary and sufficient condition for 3DFLUX to be stable is that

$$|G|_{\max} \leq 1, \tag{2.39}$$

where $|G|_{\max}$ is the maximum magnitude of G.

For a pure diffusion problem, the fluxes in equation (2.38) are determined from equation (2.35). For instance, using equation (2.11), the term $(\mathrm{f}_w - \mathrm{f}_e)$ can be written as

$$\mathrm{f}_w - \mathrm{f}_e = -\frac{\Gamma \Delta t}{\rho \Delta h^2} \left(-\frac{1}{8}\phi_{EE} + \frac{35}{24}\phi_E - \frac{31}{12}\phi_P + \frac{5}{4}\phi_W + \frac{1}{24}\phi_{WW} - \frac{1}{24}\phi_{WWW} \right). \tag{2.40}$$

Substituting equation (2.37) into equation (2.40), we obtain

$$\frac{(\mathrm{f}_w - \mathrm{f}_e)}{e^{at}e^{i(k_1x+k_2y+k_3z)}} = \\ -\frac{\Gamma\Delta t}{\rho\Delta h^2}\left(-\frac{1}{8}e^{2i\theta} + \frac{35}{24}e^{i\theta} - \frac{31}{12} + \frac{5}{4}e^{-i\theta} + \frac{1}{24}e^{-2i\theta} - \frac{1}{24}e^{-3i\theta}\right), \qquad (2.41)$$

where $\theta = k_1\Delta h$ is the wavenumber weighted by the grid spacing and $-\pi \leq \theta \leq \pi$. The other terms on the right hand side of equation (2.38) are determined similarly. Finally, it can be shown that

$$|G|_{\max} = \left|1 - 16\frac{\Gamma\Delta t}{\rho\Delta h^2}\right|, \qquad (2.42)$$

and, consequently, the stability condition is

$$0 \leq \frac{\Gamma\Delta t}{\rho\Delta h^2} \leq \frac{1}{8}, \qquad (2.43)$$

where $\Gamma\Delta t/\rho\Delta h^2$ is a dimensionless diffusive coefficient.

In addition, this analysis shows that 3DFLUX is, as UTOPIA, only second-order accurate when the problem is purely diffusive. In fact, equation (2.40) can be rewritten as a second-order finite difference approximation of the second order derivative of ϕ with respect to h, i.e.

$$\mathrm{f}_w - \mathrm{f}_e = -\frac{\Gamma\Delta t}{\rho\Delta h^2}\left(\frac{\partial^2\phi}{\partial h^2} + \frac{1}{12}\Delta h^2\frac{\partial^4\phi}{\partial h^4} + O(\Delta h^3)\right). \qquad (2.44)$$

Leonard *et al.* (1995) showed, using a Taylor series analysis, that the coupling between the advective and diffusive terms present in the flux integral method (see equation (2.30)) leads to a third-order advection-diffusion solver. However, when the coupling terms do not exist, i.e. when advection is absent, the diffusion solver is equivalent to a second-order finite difference scheme.

2.4.5 Monotonicity preservation

A scheme is said to be monotonicity-preserving when it does not generate new local extrema in the solution and the value of a local minimum/maximum

is non-decreasing/non-increasing in time (Harten, 1983). Godunov (1959) showed that any linear monotonicity-preserving scheme is, at most, first-order accurate in space. Hence, advection schemes of orders higher than one are not monotonicity-preserving, and generate spurious oscillations near discontinuities or near poorly resolved gradients of the solution. Zalesak (1979) was the first to propose a monotonicity-preserving high-order method called the flux-corrected transport (FCT) method.

The FCT method corrects the high-order solution by using a low-order scheme in the vicinity of the poorly resolved gradients and can be decomposed in four steps. In the first step, a solution is computed with a first-order scheme. It is called "transported and diffused" and is identified by the superscript "td". This solution is calculated as follows

$$\left(\phi_P^{t+\Delta t}\right)^{\mathrm{td}} = \left(\phi_P^{t}\right)^{\mathrm{corr}} + \mathrm{f}_w^{\mathrm{low}} - \mathrm{f}_e^{\mathrm{low}} + \mathrm{f}_s^{\mathrm{low}} - \mathrm{f}_n^{\mathrm{low}} + \mathrm{f}_b^{\mathrm{low}} - \mathrm{f}_f^{\mathrm{low}} + \langle S \rangle \frac{\Delta t}{\rho}, \quad (2.45)$$

where the superscript "low" indicates the fluxes computed with the low-order scheme and $(\phi_P^t)^{\mathrm{corr}}$ is the corrected solution computed at previous time steps. In our 3DFLUX solver, the low-order scheme has been implemented by simply replacing the quadratic interpolant polynomial, ψ, in equation (2.12) with a zero-order polynomial. Doing so, we obtain a first-order scheme that is equivalent to the well-known upwind scheme proposed by Patankar (1980).

The second and the third steps consist of, respectively, computing the fluxes with the high-order scheme and estimating the values of the corrected fluxes. The low-order scheme is monotonicity preserving, has low accuracy and is highly diffusive. The high-order scheme is not monotonicity preserving, but more accurate and produces low numerical diffusion. Hence, the value of the corrected fluxes has to be an optimal compromise between the values of the low- and high-order fluxes so that the corrected solution benefits from the

advantages of both schemes. The corrected fluxes are expressed, for instance at the west face, as

$$\mathrm{f}_w^{\mathrm{corr}} = \mathrm{f}_w^{\mathrm{low}} + \beta_w \mathrm{A}_w, \tag{2.46}$$

where $\mathrm{A}_w = \mathrm{f}_w - \mathrm{f}_w^{low}$ is called the anti-diffusive flux at the west face and the parameter $\beta_w \in [0, 1]$ has to be evaluated at the west face. Note that the corrected flux is equal to the low-order flux when $\beta = 0$ and equal to the high-order flux when $\beta = 1$. The fourth and final step consists of computing the corrected solution using equations (2.45) and (2.46) as follows

$$\left(\phi_P^{t+\Delta t}\right)^{\mathrm{corr}} = \left(\phi_P^{t+\Delta t}\right)^{\mathrm{td}} + \beta_w \mathrm{A}_w - \beta_e \mathrm{A}_e + \beta_s \mathrm{A}_s - \beta_n \mathrm{A}_n + \beta_b \mathrm{A}_b - \beta_f \mathrm{A}_f. \tag{2.47}$$

The main difficulty in Zalesak's method stands in correctly estimating the limiting parameters: β_w, β_e, β_s, β_n, β_b, and β_f. For further details, the reader is referred to (Zalesak, 2005).

Ideally, a flux-limiting method preserves monotonicity without corrupting the accuracy of the high-order scheme. However, Blossey & Durran (2008) showed that although Zalesak's method correctly damps the over- and under-shoots produced in the vicinity of the poorly resolved gradient, it also incorrectly damps the extrema in the smooth and well-resolved parts of the solution. This results in an undesirable reduction of the overall accuracy of the scheme. For example, Blossey & Durran (2008) showed that their third-order scheme, based on a piecewise parabolic method (PPM) (Colella & Woodward, 1984), becomes only second-order accurate when it is combined with the FCT method.

Blossey & Durran (2008) therefore modified Zalesak's method to activate the flux-limiter only in the regions of the computational domain affected by unphysical over- and under-shooting. They showed that the PPM solver combined with their selective monotonicity preserving method, remains third-order

accurate while quasi-preserving the monotonicity of the solution (i.e. the over-shoots and under-shoots are negligible with respect to the magnitude of the solution). This selective monotonicity preservation introduces a smoothness parameter, λ, to detect the presence of the poorly resolved gradients in the solution. The value of λ is computed at each cell and compared to a predefined threshold value, λ^{MAX}. When λ remains below the threshold, the parameter β is set to one, which deactivates the monotonic limiter. Otherwise, the FCT method is used to calculate the value of β, i.e.

$$\beta = \begin{cases} \beta & \text{if } \lambda > \lambda^{\mathrm{MAX}}, \\ 1 & \text{otherwise.} \end{cases} \tag{2.48}$$

Blossey & Durran (2008) computed λ at the nodes using the first- and second-order derivatives of the scalar field in the direction normal to the face. Their approach was consistent with the PPM scheme that is based on a dimensional splitting method. Note that the parameter λ is analogous to the one-dimensional smoothness metric used in the WENO scheme (Jiang & Shu, 1996). More recently, Harris *et al.* (2011) defined λ using the derivatives of the scalar field in two directions, to be consistent with their two-dimensional solver.

Herein, we propose a three-dimensional formulation of the parameter, λ, as follows

$$\lambda_{ijk} = \frac{\max_{\ell \in I, m \in J, n \in K} \{\gamma_{\ell mn}\}}{\min_{\ell \in I, m \in J, n \in K} \{\gamma_{\ell mn}\} + \varepsilon}, \tag{2.49}$$

where

$$\gamma_{\ell mn} = \frac{1}{2}\left[\left(2\Delta x\frac{\partial\phi_{\ell mn}}{\partial x}\right)^2 + \left(\Delta x^2\frac{\partial^2\phi_{\ell mn}}{\partial x^2}\right)^2 + \left(2\Delta y\frac{\partial\phi_{\ell mn}}{\partial y}\right)^2 + \left(\Delta y^2\frac{\partial^2\phi_{\ell mn}}{\partial y^2}\right)^2 + \left(2\Delta z\frac{\partial\phi_{\ell mn}}{\partial z}\right)^2 + \left(\Delta z^2\frac{\partial^2\phi_{\ell mn}}{\partial z^2}\right)^2\right], \tag{2.50}$$

and

$$\begin{cases} I &= [i-2, i+1] \\ J &= [j-2, j+1] \\ K &= [k-2, k+1], \end{cases} \tag{2.51}$$

where i, j, k and ℓ, m, n are the cell indices in the x-, y- and z-direction, respectively. The derivatives in (2.50) are directly computed using equations (2.17) and ε is a small parameter required to prevent division by zero. We obtained consistent results using $\varepsilon = 10^{-8}$ and found that $\lambda^{\text{MAX}} = 60$ is an optimal value to identify the regions of the domain in which the monotonic limiter must be applied. This value is also consistent with the value reported by Harris *et al.* (2011).

2.4.6 Implementation of the boundary conditions

Our third-order scheme uses a large stencil (see figure 2–3) to compute the fluxes and update the average cell values at each time step. Therefore, near the boundaries of the computational domain, some of the values at neighboring cells required to construct this stencil are not available. To overcome this difficulty, we extend the computational domain by introducing fictitious nodes, also known as "ghost" or external nodes, on the outside of the domain, as shown in figure 2–5. By doing so, the solution is computed at all interior cells using the same stencil and scheme.

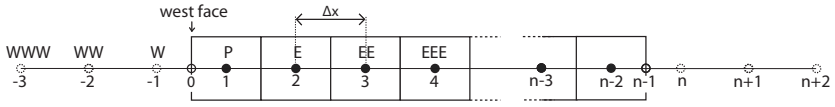

Figure 2–5: Treatment of the boundary using ghost-nodes.

The value of the scalar field at the ghost-nodes is extrapolated, at the beginning of each time step, from the boundary conditions and from the value of the scalar field at the internal nodes in the previous time step. Note that the computational scheme at the ghost-nodes can be entirely decoupled from the numerical scheme used at the interior nodes (Leveque, 2002). To compute the fluxes at the boundary with 3DFLUX, three ghost-nodes are required. However, when the fluxes are prescribed at the boundary, only the values at two ghost-nodes are required to compute the flux at the face of the first internal cell.

In practical applications, the implementation of the ghost-node technique is problem-dependent, see for example (Liu *et al.*, 2003; Krivodonova & Berger, 2006; Tan & Shu, 2010). Consequently, we restrict our discussion in this study to the treatment of the boundary conditions implemented in the test cases used to validate our solver, i.e. periodic, inflow, outflow and Neumann boundary conditions.

Periodic boundary conditions are used in all tests presented in section 2.5. In this case, the values at the three ghost-nodes are set equal to the values at the corresponding three internal nodes at the opposite side of the domain. In figure 2–5, the value of the nodes ϕ_W, ϕ_{WW} and ϕ_{WWW} is respectively equal to the value at the nodes ϕ_{n-2}, ϕ_{n-3} and ϕ_{n-4} (not shown).

The inflow and outflow conditions used in the last test of section 2.5 are those used to simulate the inlet and outlet conditions of a flow in a channel. The treatment of the inflow boundary conditions is trivial as the values of the scalar field (and by extension the values at the ghost-nodes) are prescribed at

the entrance of the channel. However, the treatment of the outflow boundary conditions is more challenging. To illustrate our discussion, we impose an outflow boundary at the node $n-1$ in figure 2–5. Among the different techniques that simulate an outflow boundary (Tsynkov, 1998; Lohéac, 1991; Nordström *et al.*, 1999; Schlatter *et al.*, 2005), we have chosen the method presented by Ferziger & Perić (2002). This method extrapolates the value of the scalar field at the ghost-nodes by solving an unsteady convective condition of the form

$$\frac{\partial \phi}{\partial t} + U \left. \frac{\partial \phi}{\partial x} \right|_n = 0, \tag{2.52}$$

where U is the average velocity of the outflow and $\partial\phi/\partial x|_n$ is the derivative of the scalar at node n in the outward direction normal to the boundary. Note that U is constant at the outlet and is chosen so that the outflow mass flux is equal to the incoming mass flux. The partial derivative, $\partial\phi/\partial x|_n$, is approximated using a third-order backward finite difference scheme (Pozrikidis, 1998, p.319)

$$\left. \frac{\partial \phi}{\partial x} \right|_n = \frac{11}{6}\phi_n - 3\phi_{n-2} + \frac{3}{2}\phi_{n-3} - \frac{1}{3}\phi_{n-4} + O(\Delta x^3), \tag{2.53}$$

and the time integration is performed using the explicit third-order Adams-Bashforth method (Durran, 1991)

$$\phi^{t+\Delta t} = \phi^t - \frac{1}{12} U \Delta t \left(23 \left. \frac{\partial \phi}{\partial x} \right|_n^t - 16 \left. \frac{\partial \phi}{\partial x} \right|_n^{t-\Delta t} + 5 \left. \frac{\partial \phi}{\partial x} \right|_n^{t-2\Delta t} \right). \tag{2.54}$$

Note that the value at the node ϕ_{n-1} is not used in equation (2.53).

The Neumann boundary condition is used in the first and last tests of section 2.5. To implement this condition, we use a local third-order Taylor expansion to extrapolate the value at the ghost-nodes. In the case shown in figure 2–5, the values of ϕ_W and ϕ_{WW} are given by

$$\phi_W = \phi_P - \Delta x \left. \frac{\partial \phi}{\partial x} \right|_w + O(\Delta x^3), \tag{2.55}$$

and

$$\phi_{WW} = \phi_E - 3\Delta x \left.\frac{\partial \phi}{\partial x}\right|_w + O(\Delta x^3), \tag{2.56}$$

respectively. Note that the no-flux boundary conditions is particularly simple to implement because the values at the ghost nodes are equal to the values at the mirror image internal points. In the case shown in figure 2–5, $\phi_W = \phi_P$ and $\phi_{WW} = \phi_E$.

2.5 Convergence rate and accuracy

The numerical errors that could affect the numerical solutions produced by 3DFLUX are attributable to *i*) the spatial interpolation presented in section 2.4.2 and *ii*) the backwards integration presented in section 2.4.3. The overall order of convergence of 3DFLUX in general is

$$O\left(\Delta t^k, \Delta h^{p+1}\right), \tag{2.57}$$

where k is the order of the time integration scheme, p is the order of the polynomial interpolant, and Δt and Δh are the temporal and the spatial resolutions of the scheme, respectively. Note that the maximum allowable time step, Δt, is controlled by the constraints (2.36) on the Courant numbers.

To assess the convergence rate and the accuracy of our solver, we present a series of five numerical tests. By construction, 3DFLUX is third-order accurate under constant flow conditions because the polynomial interpolation is quadratic ($p = 2$) and there is no truncation error in the time integration (i.e. equation (2.23) is exact). However, under non-constant flow conditions, the accuracy of the time integration algorithm depends on the accuracy of the approximation of the advective velocity field over the time interval, Δt. In 3DFLUX, the components of the velocity field in equation (2.23) are evaluated at the intermediate time step, $t + \Delta t/2$, by an explicit mid-point interpolation

(Leveque, 1996; Xiu & Karniadakis, 2001) as follows

$$\vec{u}^{t+\Delta t/2} = \frac{1}{2}\left(\vec{u}^{t+\Delta t} + \vec{u}^{t}\right). \tag{2.58}$$

Note that this temporal staggering of the velocity field maxes 3DFLUX second-order accurate in time when solving unsteady problems. However, as we will show in the following tests, the lower accuracy of the time integration scheme has a limited impact in practical applications. In fact, the accuracy of 3DFLUX depends essentially on the form of the spatial integration (Leonard *et al.*, 1993).

2.5.1 Test 1: Mixing/unmixing problem

We examine the accuracy and the convergence rate of 3DFLUX by solving the mixing/unmixing test proposed by Seibold *et al.* (2012). In this test, the computational domain is a two-dimensional square, i.e. $(x, y) \in [0, 1] \times [0, 1]$. The initial condition for the scalar field is

$$\phi(x, y, t = 0) = \cos(2\pi x)\cos(4\pi y), \tag{2.59}$$

and the boundary conditions are doubly periodic. For $t > 0$, the initial distribution of the scalar field is purely advected and deformed by the velocity field

$$\begin{cases} u(x, y, t) = \cos(\frac{\pi t}{T})\sin^2(\pi x)\sin(2\pi y) \\ v(x, y, t) = -\cos(\frac{\pi t}{T})\sin^2(\pi y)\sin(2\pi x), \end{cases} \tag{2.60}$$

which is unsteady, divergence-free and periodic in time with period T (Leveque, 1996). After each half-period, the direction of the flow is reversed and the fluid particles return to their initial position.

We perform a series of simulations in which the uniform size, $\Delta h \times \Delta h$, of the cells is repeatedly halved. We then perform an error analysis by computing the L^∞ and L^2 norms of the error, i.e. of the difference between the solution after one period T and the initial scalar field. Recall that the L^∞ norm of the

error is the maximum of the absolute value of the error. In the time integration, we use the largest possible time step allowed by the stability requirement because: *i*) the value of the maximum velocity over a period is 1, and *ii*) the upper limit of the Courant number is also 1, the largest possible time step is $\Delta t = \Delta h$.

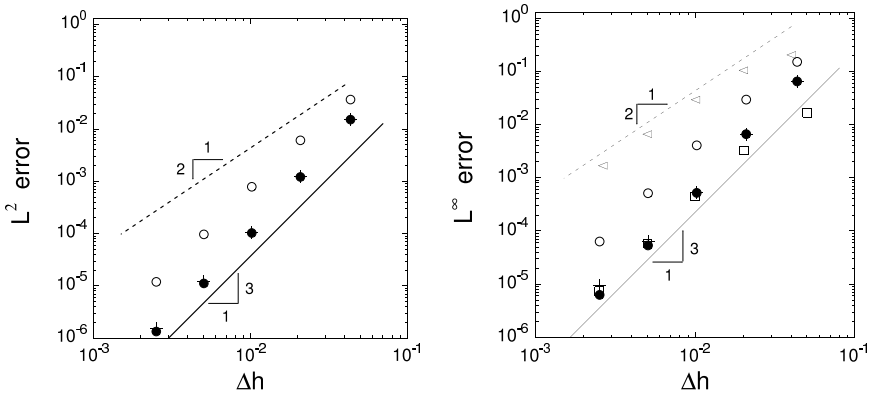

Figure 2–6: Error analysis of the mixing/unmixing problem. Convergence of the (a) L^2 and (b) L^∞ norms as a function of the cell size. The errors computed with the 3DFLUX (•), UTOPIA (○), WENO3 (◁), and bi-cubic jet (□) schemes using periodic boundary conditions, as well as the norms computed with the 3DFLUX (+) scheme when using the no-flux boundary condition are reported. The dashed and solid lines represent second- and third-order convergence, respectively. Note that the L^2 norm was not reported in (Seibold *et al.*, 2012) for the WENO3 and bi-cubic jet schemes.

Figure 2–6 reports the convergence rate of the numerical errors for several schemes including the WENO3 third-order scheme, the bi-cubic jet scheme by Seibold *et al.* (2012) and the third-order UTOPIA scheme. All schemes but WENO3 exhibit a third-order convergence rate using the L^2 and L^∞ norms. There are, however, significant differences in the accuracy of the schemes. The accuracy of 3DFLUX is comparable to the accuracy of the bi-cubic jet scheme, a recently proposed solver designed for the simulation of purely advective problems. The accuracy of UTOPIA is about an order of magnitude

worse than that of 3DFLUX, while WENO's accuracy is more than two orders of magnitude worse.

As previously mentioned, Seibold *et al.* (2012) used periodic boundary conditions in this test. However, because the velocity field is zero at any time on the boundaries of the unit square, and because there are no diffusion effects, the computational domain can be considered as a closed-domain. Hence, the solution of the test remains unchanged if we replace the periodic boundary condition with a no-flux boundary condition. We re-computed the solution up to one period T for different spatial resolutions with the no-flux boundary conditions and obtained the same results as in figure 2–6, therefore validating our implementation of the no-flux boundary conditions.

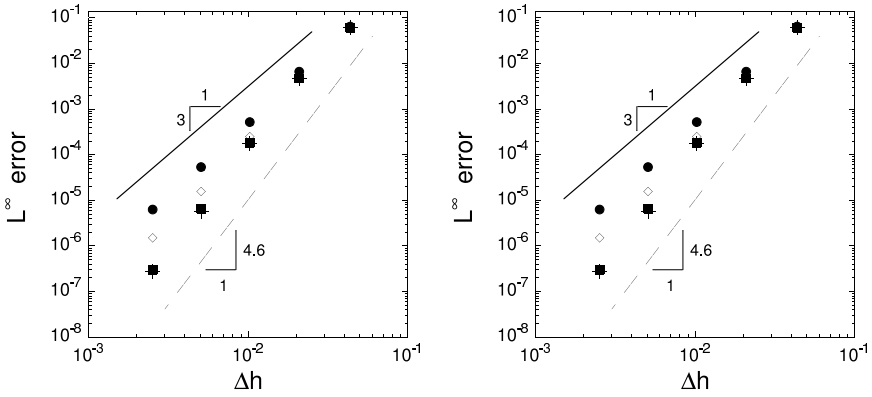

Figure 2–7: Error analysis of the mixing/unmixing problem for decreasing Courant numbers. Convergence of the (a) L^2 and (b) L^∞ norms as a function of cell size. The error computed using 3DFLUX with periodic boundary conditions at Courant numbers 1 (•), 0.1 (⋄), 0.01 (■) and 0.001 (+) is reported. The solid and dashed lines represent the slopes of convergence of order 3.0 and 4.6, respectively.

3DFLUX is nominally second-order in time and third-order in space. This is confirmed by figure 2–6, which shows that 3DFLUX is third-order when using the highest possible Courant number. One might therefore conclude that the spatial truncation error dominates the overall error. However, a series

of simulations in which the time step is repeatedly divided by a factor ten shows that a reduction in the time step leads to a considerable increase in the convergence rate of the L^2 and L^∞ norms, see figure 2–7. This result implies that the truncation error due to the time integration is not negligible. In fact, the solution computed at the highest resolution is 20 times more accurate when Δt is divided by 100. Figure 2–7 shows that the order of the convergence rate can unexpectedly be as high as 4.6, much higher than 3 when the Courant number is equal or lower to 0.01. Similarly, Blossey & Durran (2008) reported an order of convergence higher than three when using a third-order piecewise cubic method.

2.5.2 Test 2: Solid body rotation

This test, first proposed by Orszag (1971), examines the robustness of a numerical scheme when the solution contains discontinuities in its derivatives. The test consists in simulating the purely advective transport of a slotted cylinder moving in a rotational motion around the origin, as shown in figure 2–8. The slotted cylinder conserves its original shape while transported, and returns to its initial position after each period, T.

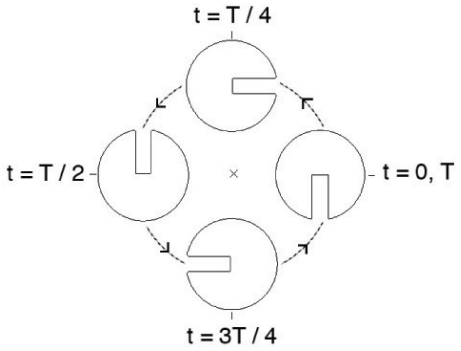

Figure 2–8: Rotation of a slotted cylinder over a period T. The position of the slotted cylinder is shown at five different times, $t = 0,\ T/4,\ T/2,\ 3T/4$ and T.

The numerical domain is a unit square domain, $(x, y) \in [-0.5, +0.5] \times [-0.5, +0.5]$. The initial condition for the concentration of the scalar field is a

slotted cylinder of diameter 0.25 centered at $(x, y) = (0.25, 0.)$, i.e.

$$\phi(x, y, t = 0) = \begin{cases} 1 & \text{if } r \leq 0.125 \wedge [(y > 0.0) \vee (0.225 < x < 0.275)] \\ 0 & \text{elsewhere,} \end{cases} \tag{2.61}$$

where

$$r = \left[(x - 0.25)^2 + y^2\right]^{\frac{1}{2}}. \tag{2.62}$$

The velocity field,

$$\begin{cases} u(x, y, t) = -\Omega y \\ v(x, y, t) = \Omega x, \end{cases} \tag{2.63}$$

transports the slotted cylinder over a circular path with constant angular velocity Ω (positive for counterclockwise rotation). Note that the domain is large enough to prevent the solid body from interacting with the boundaries. The grid is uniform, and the Courant numbers, c_x and c_y, are both set to one for each simulation, i.e. $\Delta t = 2\Delta h$.

The gradient of the scalar field at the contour of the slotted cylinder is discontinuous. Without a flux-limiter algorithm, 3DFLUX would generate spurious oscillations that would rapidly deteriorate the shape of the slotted cylinder – see for example (Xiu & Karniadakis, 2001). We show that implementing 3DFLUX with a flux-limiter algorithm prevents oscillations from occurring.

Figure 2–9 shows, for three spatial resolutions, three isocontours of the scalar field, $\phi = 0.01, 0.5$ and 0.99, after one and five revolutions of the slotted cylinder. In addition, figure 2–10 shows, after one revolution, a one-dimensional cross-section of the slotted cylinder along the x-axis and at $y = -0.05$. The $\phi = 0.5$ isocontour reproduces very well the slotted cylinder profiles, even after several rotations. The band delimited by the $\phi = 0.01$ and $\phi = 0.99$ isocontours illustrates clearly the effects of the numerical diffusion

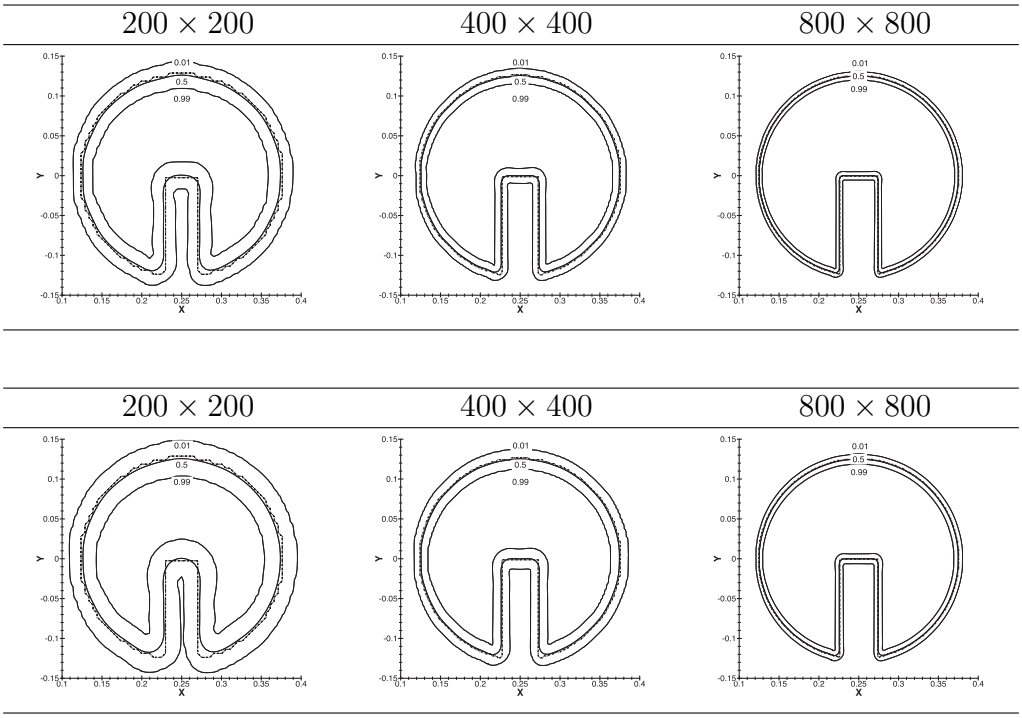

Figure 2–9: The slotted cylinder after one (a) and five (b) periods of rotation, respectively, for three different grid resolutions ($N_x \times N_y = 200 \times 200, 400 \times 400$ and 800×800). The isocontours corresponding to $\phi = 0.01$, 0.5 and 0.99, are compared to the exact solution (bold dashed line)

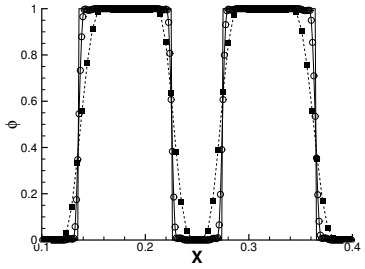

Figure 2–10: The 1D cross-section of the slotted cylinder at $y = -0.05$ for two mesh resolutions, $N_x \times N_y = 200 \times 200$ (■) and $N_x \times N_y = 800 \times 800$ (∘), are compared to the exact solution (solid line).

produced by the flux-limiter in the vicinity of the discontinuity. The flux-limiter diffuses the discontinuity of the scalar field over three nodes on each side of it, apparently independently of the spatial resolution (figure 2–10).

Hence, length scales smaller than 6 cells, centered on the discontinuity, are not fully resolved by 3DFLUX.

2.5.3 Test 3: Two-dimensional unsteady deformational flow

The pure advection test proposed by Blossey & Durran (2008) consists of simulating the stretching and rotation of a cosine bell advected by a deformational velocity field. The computational domain is the unit square $(x, y) \in [0, 1] \times [0, 1]$. The initial condition for the scalar field is defined as

$$\phi(x, y, t = 0) = \begin{cases} \frac{1+\cos(\pi r)}{2} \text{ if } \ r \leq 0 \\ \qquad 0 \quad \text{elsewhere,} \end{cases} \tag{2.64}$$

where

$$r = 5\left[(x - 0.3)^2 + (y - 0.5)^2\right]^{\frac{1}{2}}. \tag{2.65}$$

The unsteady, divergence free velocity field that advects the scalar field is defined as

$$\begin{cases} u(x, y, t) = (y - \frac{1}{2})\Omega \\ v(x, y, t) = -(x - \frac{1}{2})\Omega, \end{cases} \tag{2.66}$$

where the angular velocity, $\Omega = \Omega(x, y, t)$, is

$$\Omega(x, y, t) = \frac{4\pi}{T} \times \left\{1 + \left[1 - \frac{2}{(256\xi(x, y)^2 - 16\xi(x, y) + 1)(16\xi(x, y) + 1)}\right] \cos\left(\frac{2\pi t}{T}\right)\right\}, \tag{2.67}$$

where $\xi(x, y)$ is

$$\xi(x, y) = \left(x - \frac{1}{2}\right)^2 + \left(y - \frac{1}{2}\right)^2. \tag{2.68}$$

Figure 2–11 presents the evolution of the cosine bell in the clockwise direction at seven different time instants, $t = 0$, $T/4$, $2T/5$, $T/2$, $3T/5$, $3T/4$ and T. During the first half period (figure 2–11), the velocity field deforms the cosine bell and generates a long tail that stretches away from the center of the

bell. Sharp gradients appear on the lateral sides of the tail. At $t = T/2$, the bell recovers its initial shape and position. In the second half period (figure 2–11), the orientation of the stretching is inversed while the orientation of the circular motion remains in the clockwise direction. Finally, at $t = T$, the cosine bell returns to its initial position. The exact solution to this problem after one period is its initial condition, i.e. the scalar field defined in equation (2.64).

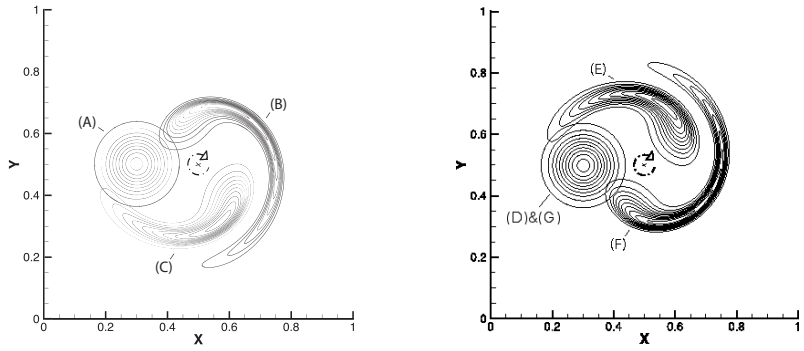

Figure 2–11: Advection of a cosine bell at different time intervals: $t = 0$ (A), $t = T/4$ (B), $t = 2T/5$ (C), $t = T/2$ (D), $t = 3T/5$ (E), $t = 3T/4$ (F) and $t = T$ (G). The isocontours are plotted from 0.05 to 0.95 in increments of 0.1.

The time evolution of the cosine bell has been computed using the largest time step possible corresponding to the largest Courant numbers admissible, i.e. $c_x = c_y = 1$. Note that in contrast with the mixing/unmixing test shown in section 2.5.1, where the transition from mixing to unmixing was obtained by reversing the flow, the velocity field defined in the present test never reverses. Blossey & Durran (2008) recommended avoiding tests with inversions of the velocity field because they can lead to phase error cancellation, masking computational inefficiencies.

To quantify the numerical error of 3DFLUX, we compare the initial condition (the exact solution) with the numerical solution obtained after one period. Figure 2–12 plots the contours of the exact and numerical solutions after one

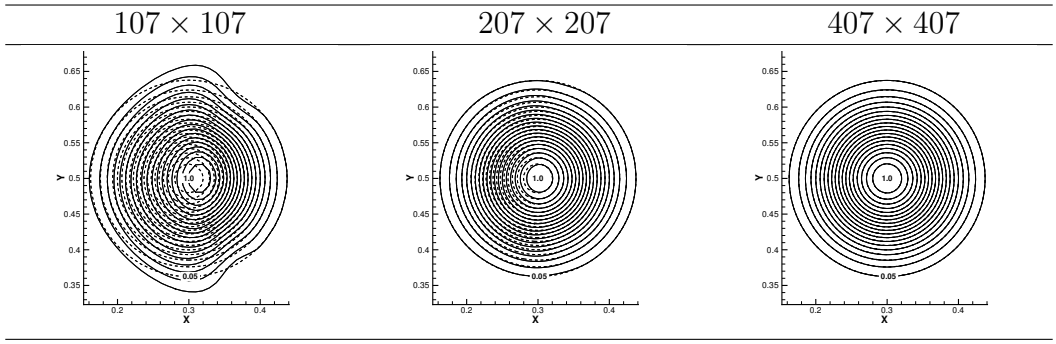

Figure 2–12: Comparison of the numerical solution after one period (solid lines) computed with 3DFLUX and the exact solution (dashed lines) for three different grid resolutions: $N_x \times N_y = 107 \times 107$ ($\Delta h = 0.01$), 207×207 ($\Delta h = 0.005$) and 407×407 ($\Delta h = 0.0025$) where $\Delta h = \Delta x = \Delta y$. The isocontours are plotted from 0.05 to 0.95 in increments of 0.05.

period for three different spatial resolutions, $N_x \times N_y = 107 \times 107,\ 207 \times 207$, and 407×407. The coarser resolution does not accurately resolve the small scales induced by the intensive stretching and, consequently, the solution is deformed in the y-direction and the center of the cosine bell is not correctly recovered. However, the monotonicity of the solution is preserved. Moreover, 3DFLUX does not generate spurious oscillations despite the presence of sharp gradients. The results obtained with finer resolutions (207×207 and 407×407) preserve well the symmetry of the cosine bell and its peak locations.

To characterize the convergence rate and accuracy of 3DFLUX, we calculate the L^2 and L^∞ norms of the error while halving the grid resolution. In figure 2–13, we compare the performance of 3DFLUX to those of UTOPIA and a second-order in time and third-order in space PPM scheme (Blossey & Durran, 2008). Figure 2–13 shows that, on average, at the highest resolution (807×807), 3DFLUX is twice as accurate as PPM and an order of magnitude more accurate than UTOPIA.

In addition, figure 2–13 confirms the results obtained in test 1. 3DFLUX is about one order of magnitude more accurate than UTOPIA in reconstructing

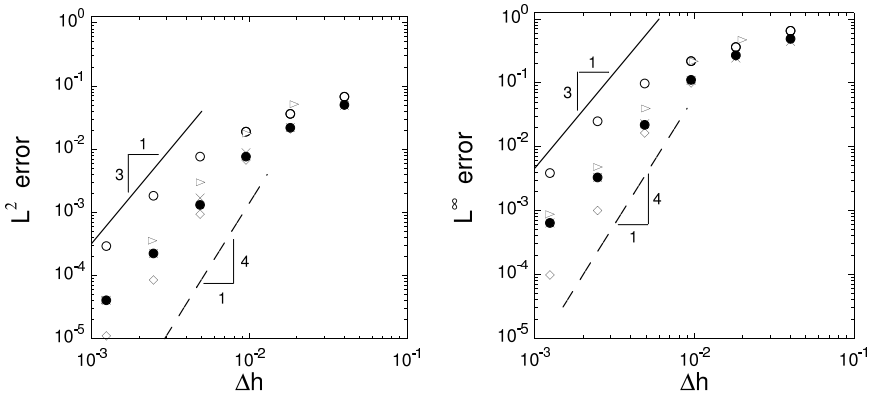

Figure 2–13: Error analysis for the two-dimensional unsteady deformational flow test. Convergence of (a) L^2 and (b) L^∞ norms as a function of the cell size, Δh, when $c_x = c_y = 1.0$. 3DFLUX (•), 3DFLUX with no limiter (×), UTOPIA (○) and the PPM scheme with selective FCT from (Blossey & Durran, 2008)(▷). Errors computed with the Courant numbers $c_x = c_y = 0.1$ using 3DFLUX (◇) are also reported. The solid and dashed lines show the slopes of third- and fourth-order convergence rates, respectively.

a smooth function that is subjected to substantial stretching. Apparently, the simplified polynomial interpolant used in UTOPIA, where the cross-terms are missing (Leonard *et al.*, 1995), induces a substantial loss of accuracy when the transport in the transverse directions is significant (see figure 2–13).

Although, 3DFLUX is nominally second-order in time and third-order in space, this test confirms that the convergence rate and accuracy of 3DFLUX improve at smaller time steps and, consequently, depend on the Courant numbers chosen. As shown in figure 2–13, the convergence rate of 3DFLUX increases and tends to be third-order when the time step is reduced by an order of magnitude. In fact, the slope of the L^∞ and L^2 norms for the two finest spatial resolutions shown in figure 2–13 are respectively equal to 2.39 and 2.48 when $c_x = c_y = 1.0$ and they are equal to 3.00 and 3.39, respectively, when $c_x = c_y = 0.1$. Note also the substantial improvement in accuracy when the Courant number is 0.1.

	3DFLUX with selective monotonic flux-limiter			3DFLUX without flux-limiter		
Δh	ϕmax	$\phi_{\min}$	L^∞	ϕmax	$\phi_{\min}$	L^∞
0.0400	0.583	-0.0000	0.492	0.605	-0.0741	0.447
0.0181	0.957	-0.0002	0.270	0.953	-0.0356	0.245
0.0095	1.004	-0.0002	0.112	1.006	-0.0196	0.109
0.0048	0.999	-0.0001	0.022	0.999	-0.0071	0.022
0.0024	0.999	-0.0001	0.003	0.999	-0.0009	0.003
0.0012	1.000	-0.0000	6×10^{-4}	1.000	-0.0001	6×10^{-4}

Table 2–1: Extrema and L^∞ norm computed with and without the flux-limiters after one period of the deformational flow. Δh is the uniform spatial resolution and the number of nodes, $N_x \times N_y$, are 27×27, 57×57, 107×107, 207×207, 407×407 and 807×807.

It is important to note that the accuracy and the convergence rate of 3DFLUX remain unchanged with or without the activation of the flux limiter presented in section 2.4.5. To obtain better insight into the efficiency of the selective monotonic limiter, we report the values of the extrema generated by the deformational flow for the different grid resolutions in table 2–1. As expected, the flux limiter considerably damps the undershoots that appears in a non-monotonicity preserving solution, and the remaining negative values are so small that they can be neglected. Note that when even small negative values are undesirable, a positivity preserving correction can be implemented (see Blossey & Durran, 2008, for details). Finally, we remark that the effect of the flux limiter becomes unobservable at the finest resolution reported in table 2–1.

2.5.4 Test 4: Three-dimensional advection-diffusion problem

This test investigates the convergence rate of 3DFLUX when solving a three-dimensional advection-diffusion problem. The test simulates the transport of a Gaussian sphere. The initial scalar field is

$$\phi(x, y, z, t = 0) = \exp\left[\frac{(x - x_0)^2 + (y - y_0)^2 + (z - z_0)^2}{-4\Gamma}\right], \tag{2.69}$$

where $(x_0, y_0, z_0) = (0.8, 0.8, 0)$ are the coordinates of the center of the Gaussian sphere. The velocity field

$$\begin{cases} u(x,y,z) = \Omega\left[-y\cos^2(\frac{\pi}{4}) - z\sin(\frac{\pi}{4})\right] \\ v(x,y,z) = \Omega\left[x\cos^2(\frac{\pi}{4}) - z\sin(\frac{\pi}{4})\cos(\frac{\pi}{4})\right] \\ w(x,y,z) = \Omega\left[x\sin(\frac{\pi}{4}) + y\sin(\frac{\pi}{4})\cos(\frac{\pi}{4})\right], \end{cases} \tag{2.70}$$

advects the Gaussian sphere along a circular trajectory lying on a diagonal plane of the cubic domain at a constant angular velocity, $\Omega = 2\pi$. After a complete rotation, i.e. at time $t = 1$, the exact solution is

$$\phi(x,y,z,t=1) = \frac{1}{2^{3/2}}\exp\left[\frac{(x-x_0)^2 + (y-y_0)^2 + (z-z_0)^2}{-8\Gamma}\right]. \tag{2.71}$$

We simulate the evolution of the Gaussian sphere (2.69) within a cube, $(x, y, z) \in [-2, 2] \times [-2, 2] \times [-2, 2]$, using a uniform spatial discretization, i.e. $\Delta x = \Delta y = \Delta z = \Delta h$, and a the time step corresponding to a Courant number of 0.9. We estimate the numerical error by comparing our solution with the exact solution (2.71).

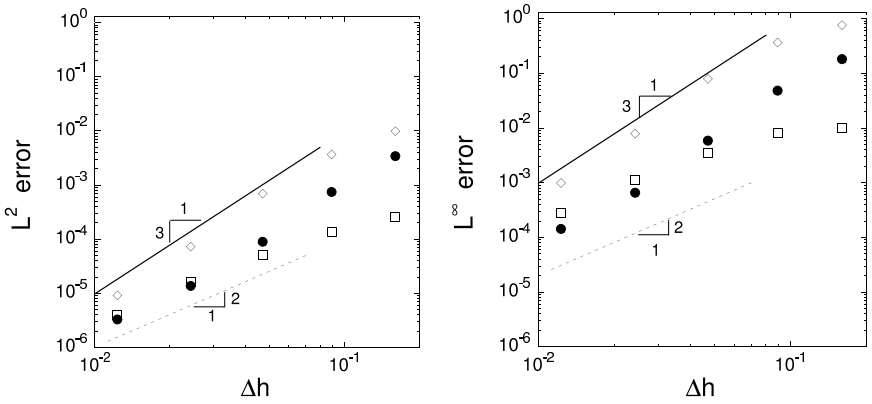

Figure 2–14: Error analysis for the three-dimensional advection-diffusion problem. Convergence of (a) L^2 and (b) L^∞ norms as a function of the cell size, Δh, when solving the pure advection ($\diamond$), the pure diffusion ($\square$) and the advection-diffusion ($\bullet$) test with 3DFLUX. The dashed and solid lines show the slopes of second- and third-order convergence rates, respectively.

The L^2 and L^∞ norms of the errors are reported in figure 2–14. 3DFLUX is third-order accurate when solving the advection-diffusion problems. Note that for the coarser spatial resolution, the Péclet cell number ($\rho u_{\max} \Delta h / \Gamma$), i.e. the ratio of the Courant number over the diffusive stability constraint (2.43), is 233, whereas for the finer spatial resolution it is 19. This is a considerable improvement with respect to second-order central difference schemes, which generate spurious oscillations for Péclet cell numbers higher than 2, see section 2.4.2.

Furthermore, figure 2–14 shows the numerical errors obtained in two additional tests: one where the diffusive terms are zero, i.e. $\Gamma = 0$, and the other where the velocity field (2.70) is replaced by a zero velocity field. The pure advective solution is compared to the initial solution after one full rotation whereas the pure diffusive solution is compared to the exact solution (2.71) at $t = 1$. Figure 2–14 shows that 3DFLUX is third-order when solving the purely advective problem, however, it becomes second-order when solving the pure diffusive problem, as noted in section 2.4.4.

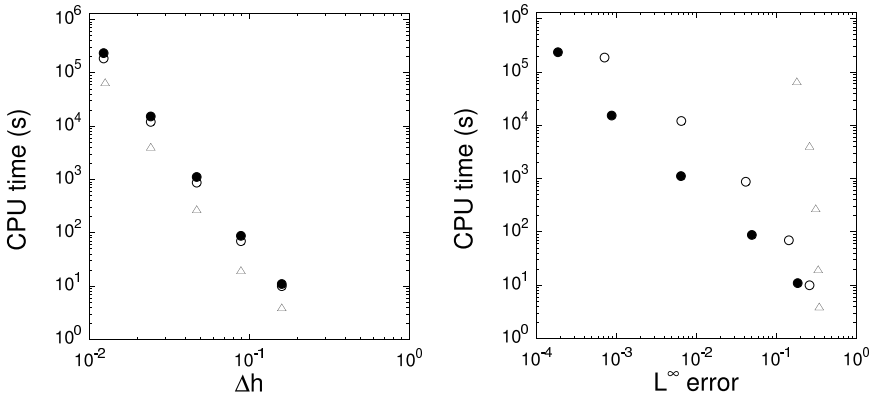

Figure 2–15: 3D advection-diffusion problem. Computational cost (a) and efficiency (b) are reported for 3DFLUX (•), UTOPIA (○) and the hybrid scheme (△) at $c = 0.45$.

To characterize the computational cost and efficiency of our code, we compare the CPU time required by 3DFLUX, UTOPIA and a traditional first-order discretization scheme to calculate the solution of the present test up to time $t = 1$. The low-order scheme is the hybrid scheme described in Spalding (1972) and Patankar (1980) which combines upwind and central differencing for the advective and diffusive terms, respectively, and use a second-order Runge-Kutta method for the time integration. 3DFLUX, UTOPIA and the hybrid scheme are all second-order in time. The hybrid scheme is a simple and fast algorithm that is implemented in most commercial CFD codes. For all computations, we set the Courant numbers to 0.45 because the hybrid scheme becomes unstable for higher Courant numbers.

The computation was performed using two standard high-end multi-core CPUs (Intel Xeon (R) E5645) running at 2.40 GHz with 48 GB of RAM. We leveraged Intel's Thread Building Blocks (TBB) library to exploit the capabilities of the multi-core processor. TBB is an object oriented library for `C++` language that allows programmers to decide the extent of parallelism.

Figure 2–15(a) show the CPU time (in seconds) needed for the computation as a function of the spatial resolution. As expected, the first-order scheme is significantly faster than the two others schemes because it performs a substantially smaller number of flops and does not require a flux limiter. We observe that UTOPIA is roughly 20% faster than 3DFLUX. Figure 2–15(b) plot the CPU time as a function of the L^∞ norm of the numerical error. 3DFLUX is clearly the most efficient scheme. For a given value of the L^∞ norm, 3DFLUX is about 10 times faster than UTOPIA. The poor efficiency of the hybrid scheme is due to its high numerical diffusion that affects considerably the solution of the multidimensional problems.

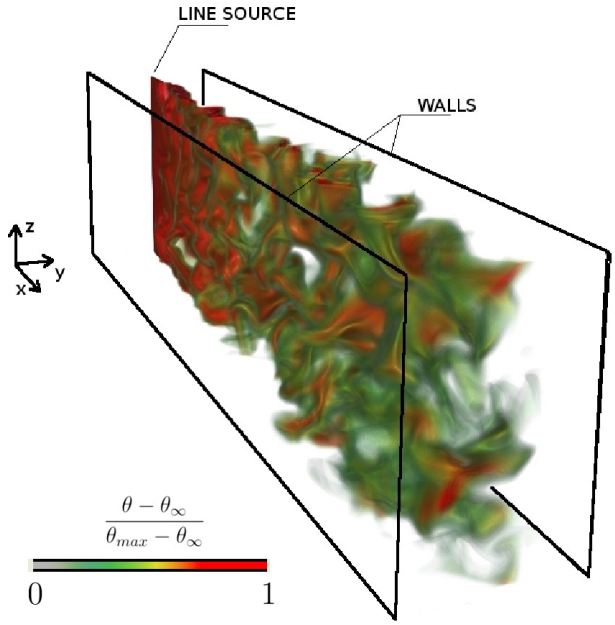

Figure 2–16: Release of a passive scalar from a line source in a turbulent channel flow. The mean flow is oriented in the positive x-direction. (Imagery produced using VAPOR, www.vapor.ucar.edu).

2.5.5 Test 5: Turbulent mixing in a channel flow

This test illustrates the potential of 3DFLUX to simulate complex flows of practical relevance. To this end, we simulated a real experiment where a scalar, temperature, is released from a heated line source in a fully developed turbulent channel flow (Lavertu & Mydlarski, 2005; Lepore & Mydlarski, 2011). Note that heat is released at a sufficiently small rate so that it has no effect on the dynamics of the fluid motion, i.e. the problem is one-way coupled. For this reason, we pre-compute the turbulent flow with a spectral solver and, once the velocity field is available, we compute the evolution of the scalar field a posteriori using 3DFLUX.

We simulate the experiment (Lavertu & Mydlarski, 2005; Lepore & Mydlarski, 2011) in a numerical channel of size $(x, y, z) \in \{[0, 4\pi] \times [-1, 1] \times [0, \pi]\}$, oriented so that x is the streamwise direction, y is the wall-normal direction, and z is the spanwise direction of the flow. The channel is delimited by two

parallel flat walls located at $y = \pm 1$. The scalar field is injected in the flow at constant power by a line source oriented in the spanwise direction located at $(x, y) = (0.24, 0)$, as shown in figure 2–16.

The turbulent velocity field is computed using a spectral code (Gibson *et al.*, 2008; Gibson, 2010*a*, `http://channelflow.org/`), which uses a spectral discretization in space (Fourier $\times$ Chebyshev $\times$ Fourier) and a third-order Runge-Kutta time integrator to solve the incompressible Navier-Stokes equations. The boundary conditions are periodic in the streamwise and spanwise directions and consist of no-penetration and no-slip conditions at the walls. The pressure gradient that drives the flow in the positive x-direction is adjusted dynamically to maintain a constant mass flux through the channel. The code is initialized with a parabolic velocity profile, $\vec{u} = [(1 - |y|)^2, 0, 0]$ plus a random disturbance to accelerate the onset of turbulence. The simulations are performed at a Reynolds number $Re = \langle U \rangle \, h/\nu = 3475$, where $\langle U \rangle$ is the mean velocity at the centerline of the channel, where the brackets indicate averaged values, h is the channel half-width and ν is the kinematic viscosity.

3DFLUX uses the precomputed velocity field as an input to solve the transport equation for the temperature ϕ. We discretized the channel with a grid $N_x \times N_y \times N_z = 771 \times 195 \times 194$ to resolve both the large and small scales of the turbulent scalar mixing. The boundary conditions for the scalar field are *i*) periodic in the spanwise direction, *ii*) inflow/outflow at the inlet/outlet of the channel, and *iii*) adiabatic (no-flux) at the walls. The line source is simulated by a sequence of nodes having a constant source term S.

The temperature field forms a plume that is transported in the streamwise and wall-normal directions, as shown in figure 2–16. The turbulent plume induces mixing over a wide range of length scales. A statistical description of the scalar field enables an analysis of the dynamics of mixing. In this test,

we compare statistics of the numerical simulations with the ones obtained in our experiments. In addition, we also report the data of Lavertu & Mydlarski (2005), where available. Since the Reynolds number of the experiments, $Re = 10350$, is higher than that used in the simulation, we use an appropriate normalization to make a meaningful comparison between the experimental and numerical results.

We first analyze the mean and root-mean-square (r.m.s.) temperature profiles and their peaks and widths. To this end, we define the scalar excess as $\Delta\phi = \phi - \phi_0$, where ϕ_0 is the ambient temperature in the channel before the injection of the scalar, and then we decompose it into a mean, $\langle\Delta\phi\rangle = \langle\phi - \phi_0\rangle$, and a fluctuating part θ, i.e. $\Delta\phi = \langle\Delta\phi\rangle + \theta$. The average value of the scalar field, $\langle\phi\rangle$, at a given location (x, y) can be expressed as

$$\langle\phi\rangle = \langle\phi(x,y)\rangle = \frac{1}{N_t}\sum_{1}^{N_t}\frac{1}{N_z}\sum_{1}^{N_z}\phi(x,y,z,t), \tag{2.72}$$

where N_t is the number of time steps required to obtain converged statistics. Since the scalar field is periodic, and thus statistically homogeneous in the spanwise direction, the statistics are computed by averaging the scalar field in the spanwise direction. We obtained converged statistics by running 3DFLUX for $2.2h/u_\tau$, which is equivalent to $N_t = 5,000$ with $\Delta t = 4.39 \times 10^{-4} h/u_\tau$, where $u_\tau = \sqrt{-(h/\rho)\partial\langle p\rangle/\partial x}$ is the friction velocity and $\partial\langle p\rangle/\partial x$ is the mean axial pressure gradient.

The mean and the r.m.s. temperature profiles normalized by their respective peak values are plotted as a function of the wall-normal locations at several locations downstream from the line source, see figure 2–17 and 2–18. Both experimental and numerical mean and r.m.s. profiles agree very well. The symmetry of the Gaussian distribution of the numerical profiles suggests that the flow statistics are correctly converged. Figure 2–19 shows the standard

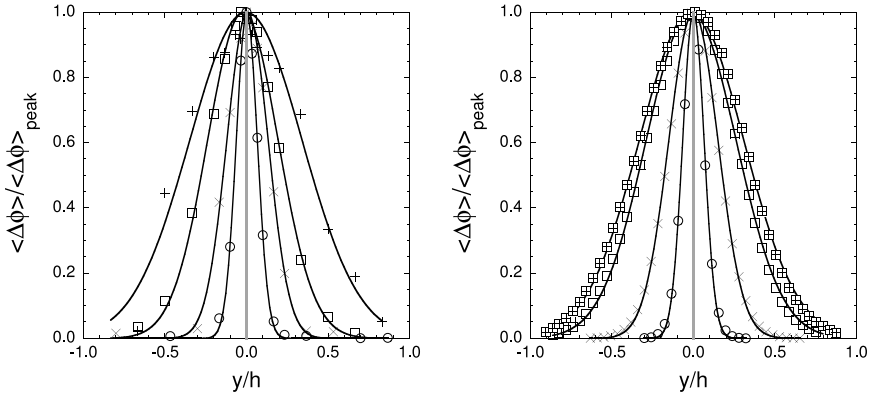

Figure 2–17: Non-dimensionalized mean temperature excess profiles at different downstream locations. Results from our experiments (a) and 3DFLUX (b) are reported for ∘, $x/h = 2.0$; ×, $x/h = 5.0$; □, $x/h = 10.0$; ⊞, $x/h = 12.0$; +, $x/h = 15.0$. The grey line indicates the transverse location of the source ($y_s/h = 0.0$) and the black lines are Gaussian curve fits to the data.

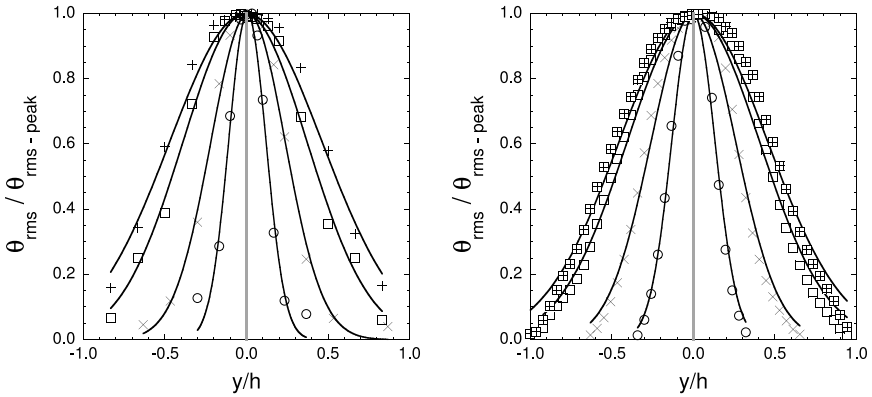

Figure 2–18: Non-dimensionalized r.m.s. temperature profiles at different downstream locations. Results from our experiments (a), and 3DFLUX (b) are reported for ∘, $x/h = 2.0$; ×, $x/h = 5.0$; □, $x/h = 10.0$; ⊞, $x/h = 12.0$; +, $x/h = 15.0$. The grey line indicates the transverse location of the source ($y_s/h = 0.0$) and the black lines are Gaussian curve fits to the data.

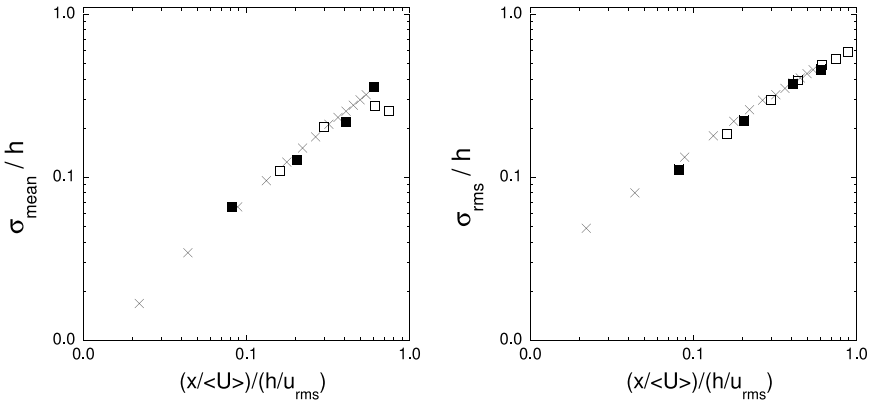

Figure 2–19: Non-dimensionalized standard deviation of the mean (a) and r.m.s. (b) temperature profiles at different downstream locations. Our experiments (■), 3DFLUX (×) and experimental results of (Lavertu & Mydlarski, 2005) (□). $\langle U \rangle$ and u_{rms} are the mean and r.m.s. velocities at the centerline of the channel, respectively.

deviation of the mean and r.m.s. profiles normalized by the channel half-width at several stations downstream the line source. All these results show an excellent agreement between the numerical simulations performed with 3DFLUX and the experiments.

2.6 Conclusions

We have presented 3DFLUX, a high-order, fully multidimensional, conservative, monotonicity preserving numerical scheme for the solution of the scalar transport equation. 3DFLUX is nominally third-order in space and second-order in time. Its convergence rate and accuracy have been characterized via several multidimensional tests, both purely advective and advective-diffusive problems. In general, when using the highest possible Courant number (one in our implementation), 3DFLUX presents a noticeably higher accuracy than the currently available numerical schemes having the same convergence rate. This is owed to the stencil presented in this article – a stencil that allows an accurate three-dimensional interpolation of the solution over a computational

cell. Unexpectedly, at low Courant numbers, 3DFLUX appears to be super-convergent and, depending on the problem solved, is fourth-order or higher in space.

3DFLUX is very attractive for research-oriented or high-end engineering applications because it does not require dimensional splitting and generates highly accurate solutions at a realistic computational cost. We successfully tested 3DFLUX's potentials by simulating a complex flow where a scalar is released from a line source in a fully turbulent channel flow. We showed a remarkable agreement between the statistics produced by 3DFLUX and those measured in an experiment.

Acknowledgements

The authors wish to thank P. Blossey and J. F. Gibson for the helpful discussions regarding selective flux-limiters and turbulent channel flow solvers, respectively. Funding was provided by NSERC under Contracts No. RGPIN217169 and No. RGPIN217184.

CHAPTER 3

Evolution of the scalar dissipation rate emitted from a concentrated line source in turbulent channel flow

3.1 Preface

As discussed in the previous chapter, a novel numerical scheme (3DFLUX) was developed to solve the advection-diffusion equation. 3DFLUX can be used to calculate quantities that are not accessible experimentally. In the context of the present work, such quantities include simultaneous measurements of temperature derivatives and cross-derivatives, measurement of the temperature fluctuations in the vicinity of walls, etc.

Reaping the complementary benefits of experiments and numerical simulations, both a quantitative description as well as a physical understanding of the phenomena that govern turbulent mixing are described in this chapter. The statistical analysis reported herein focuses on the scalar dissipation rate of the temperature field generated by a line source in a turbulent channel flow. The open-circuit high-aspect-ratio channel designed for the experiments is shown in figure 3–1 and examples of the direct numerical simulation are shown in figure 3–2.

One-dimensional spectra and probability density functions of temperature derivatives are investigated to study the evolution of the small-scale anisotropy within the thermal plume. The key role played by the velocity gradients near

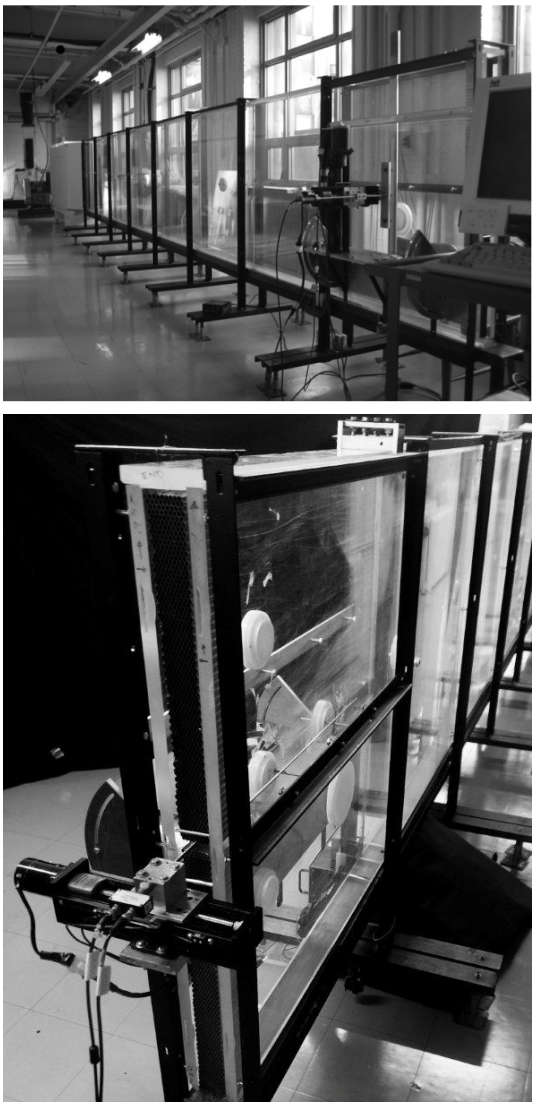

Figure 3–1: Channel and test section in which the experiments were conducted.

the wall is discussed in detail. To the best of my knowledge, such a statistical analysis, performed by means of both numerical simulations and experiments has no analog in the scientific literature.

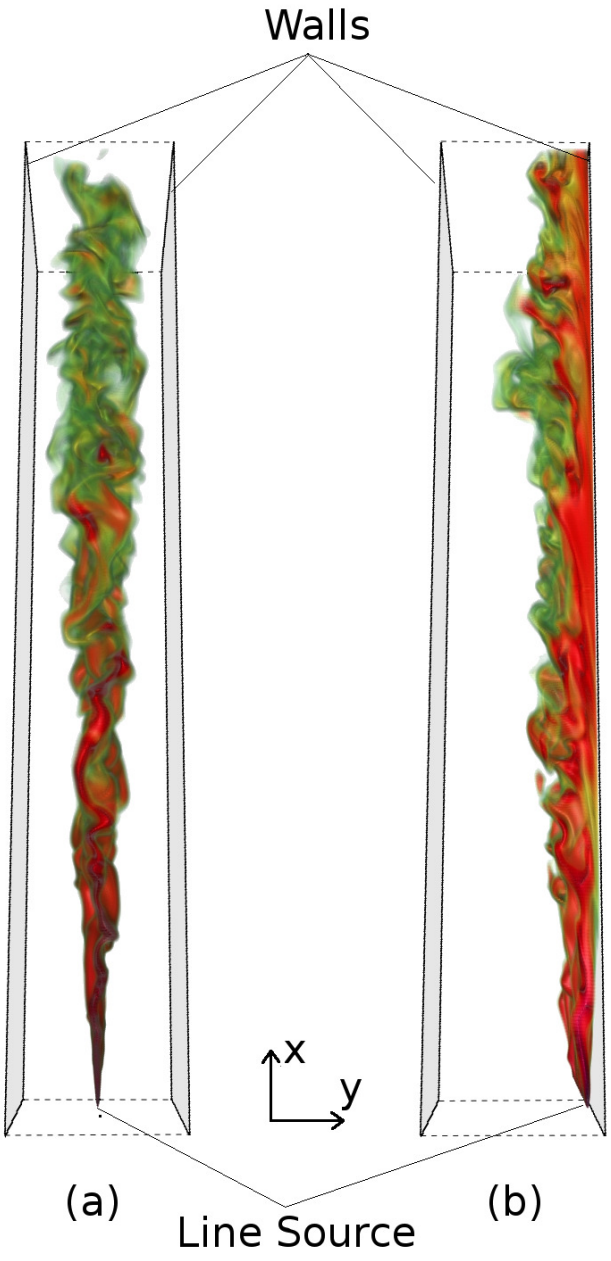

Figure 3–2: Examples of the direct numerical simulation. Top view of the instantaneous scalar field for two line source locations.

Evolution of the scalar dissipation rate emitted from a concentrated line source in turbulent channel flow

Emmanuel Germaine, Luca Cortelezzi and Laurent Mydlarski

Department of Mechanical Engineering, McGill University, Montreal, Quebec, Canada

3.2 Abstract

The dissipation rate, ε_θ, of a passive scalar (temperature in air) emitted from a concentrated source into a fully developed high-aspect-ratio turbulent channel flow is studied. The goal of the present work is to investigate the return to isotropy of the scalar field when the scalar is injected in a highly anisotropic manner into an inhomogeneous turbulent flow at small scales. Both experiments and direct numerical simulations (DNSs) are used to study the downstream evolution of ε_θ for scalar fields generated by line sources located at the channel centreline ($y_s/h = 1.0$) and near the wall ($y_s/h = 0.17$). The temperature fluctuations and temperature derivatives were measured by means of a pair of parallel cold-wire thermometers in a flow at $Re_\tau = 520$. The DNSs were performed at $Re_\tau = 190$ using a spectral method to solve the continuity and Navier-Stokes equations, and a flux integral method (Germaine *et al.*, 2013, 3DFLUX) for the advection-diffusion equation. The statistics of the scalar field computed from both experimental and numerical data were found to be in good agreement, with certain discrepancies that were attributable to the difference in the Reynolds number of the two flows. The return to isotropy of the small scales is never perfectly observed in any region of the channel for the downstream distances studied herein. However, a continuous decay of the small-scale anisotropy is observed for the scalar field generated by the centreline line source in both the experiments and DNSs. The scalar mixing is found to be more rapid in the near-wall region, where experimental

results exhibit low levels of small-scale anisotropy. However, the DNSs, being performed at lower Re_τ, show that persistent anisotropy can also exist near the wall, independently of the downstream location. The role of the mean velocity gradient in the production of ε_θ (and therefore anisotropy) in the near-wall region is highlighted.

3.3 Introduction

The ability of turbulence to mix one or more scalars within a fluid is of particular relevance to a variety of engineering applications including combustion, pollution dispersion and heat transfer. Using premixed combustion as an example, reactions occur only if the fuel and oxidizer are sufficiently mixed at the molecular level prior to ignition. However, our comprehension and ability to predict turbulent mixing are limited because the fluid mechanics that governs turbulent mixing involve multi-scale phenomena for which the details are not yet fully understood.

The turbulent mixing process stretches and stirs the scalar field, which serves to increase the scalar gradients. The scalar fluctuations are then smoothed out by the molecular mixing that principally occurs at the smallest scales of the turbulence. The rate of destruction of the scalar variance is quantified by the scalar dissipation rate, $\varepsilon_\theta (\equiv \alpha \langle (\partial\theta/\partial x_i)^2 \rangle$. It is the only term in the scalar variance budget that must be non-zero in every turbulent flow. Consequently, ε_θ is omnipresent and of critical importance to the description of turbulent scalar fields. Furthermore, it is a quantity whose primary contributions derive from the smallest scales of the scalar field.

The predominant theory related to turbulent scalar mixing, Kolmogorov Obukhov Corrsin (KOC) theory, predicts that the small scales should be isotropic and independent of the large scales of a scalar field; the latter being anisotropic in most cases. However, it has been shown that departure from

isotropy occurs at the small scales of the scalar field when its large scales are anisotropic, which puts KOC phenomenology into question (Warhaft, 2000).

Investigations into the local isotropy of the scalar field (and, in particular, violations thereof) have been widely reported in the literature (e.g. Sreenivasan, 1991). However, the large majority of these focussed on the evolution of a scalar field injected into a turbulent hydrodynamic field at large scales. Furthermore, in many cases, the underlying flow was homogeneous and isotropic. The assumption of homogeneity considerably simplifies the analysis and yields interesting similarities between the scaling of the velocity and scalar fields when the injection occurs at large scales (Corrsin, 1952; LaRue & Libby, 1981; Ma & Warhaft, 1986; Danaila *et al.*, 2012). However, such a configuration is not representative of real flows, which are generally inhomogeneous and exhibit discrepancies between the scales of the velocity and scalar fields. Furthermore, only a subset of the previous work has focussed on the dissipation rate of the scalar variance, even though ε_θ remains one of the less understood (yet most important) quantities within a turbulent flow.

The small-scale injection of a scalar by means of a point or line source in an inhomogeneous flow is of relevance to multiple engineering applications, including the transport of a plume emitted by a smokestack in the atmospheric boundary layer, or the mixing of chemical species injected into a combustion chamber. Given the importance of such applications, it is somewhat surprising that relatively few studies of turbulent scalar mixing resulting from small-scale injection and focusing on the scalar dissipation rate, ε_θ, have been undertaken. This fact motivates the research herein.

The main objective of the present work is to further investigate and understand the evolution of the scalar field when injected in a highly anisotropic manner at small scales in an inhomogeneous turbulent flow. In measuring the

evolution of ε_θ downstream of the source, we aim to further our understanding of the details of the scalar mixing process, which will improve our effectiveness in predicting the phenomena that rely on this process. In many cases, local isotropy is invoked when estimating ε_θ. When the scalar is injected at small scales, such an assumption is clearly inaccurate near the source. Furthermore, though this assumption may increase in validity with increasing distance from the source, the rate at which it does so is an important factor. Therefore, particular attention will be paid to the evolution of the three different components of the scalar dissipation rate: $\varepsilon_{\theta_x} \equiv \alpha\langle(\partial\theta/\partial x)^2\rangle$, $\varepsilon_{\theta_y} \equiv \alpha\langle(\partial\theta/\partial y)^2\rangle$ and $\varepsilon_{\theta_z} \equiv \alpha\langle(\partial\theta/\partial z)^2\rangle$. We focus our attention on the relative contributions of ε_{θ_x}, ε_{θ_y} and ε_{θ_z} to ε_θ, and therefore on the evolution of this anisotropy. To this end, all three components of the scalar dissipation rate have been studied both, experimentally and by means of numerical simulations.

The remainder of this paper is organized as follows. The relevant literature is reviewed in §3.4. Then, the experimental apparatus and details of the numerical simulations are reported, respectively, in §3.5 and §3.6. Results are presented in §3.7, comparing, as often as possible, the experimental and numerical results. Large-scale statistics (mean and root-mean-square (r.m.s.) temperatures) are also compared to the previous results of Lavertu & Mydlarski (2005) to validate our measurements. The evolution of the scalar dissipation rate and its three components at several locations are then reported in detail. Finally, conclusions are presented in §3.8.

3.4 Literature review

The theoretical foundation of (hydrodynamic) turbulence was proposed by Kolmogorov (1941). This work, commonly referred to as $K41$, introduces several concepts necessary to the description of the transport and dissipation of turbulent kinetic energy in a turbulent flow. As there is also significant interest

in heat and mass transfer, Kolmogorov's arguments were extended by Obukhov (1949) and Corrsin (1951) to the transport of passive scalars, referred to as the Kolmogorov Obukhov Corrsin (KOC) phenomenology. At sufficiently high Reynolds numbers ($Re = UL/\nu$, where U is an average fluid velocity, L is some characteristic length of the system, and ν is the kinematic viscosity of the fluid) and Péclet numbers ($Pe = UL/\alpha$ or UL/D, where α is the thermal diffusivity of the fluid and D the scalar (molecular) diffusivity of a chemical species in the fluid), it supposes that there is a decay of any large-scale anisotropy when smaller and smaller scales are considered, the scalar dissipative scales returning to a statistically isotropic state. The smallest hydrodynamic and scalar scales (η and η_θ, respectively) are related by the Prandtl number ($Pr = \nu/\alpha$) or Schmidt number ($Sc = \nu/D$). (Subsequently, in the interest of concision, we will assume the scalar under consideration is temperature in our discussions.) The relationship between η, η_θ and Pr depends on whether $Pr > 1$ or $Pr < 1$. Note that η_θ and η are of the same order of magnitude in the air flow studied herein, where $Pr = 0.7 \approx O(1)$. Therefore $\eta_\theta = \eta Pr^{-3/4}$ (Corrsin, 1951) where $\eta = (\nu^3/\varepsilon)^{1/4}$ and where $\varepsilon \equiv 2\nu\langle s_{ij}s_{ij}\rangle$ is the dissipation rate of turbulent kinetic energy. ($s_{ij} \equiv \frac{1}{2}(\partial u_i/\partial x_j + \partial u_j/\partial x_i)$ is the fluctuating strain rate.)

The transport of a scalar quantity injected by a line source in a turbulent flow has been studied since the early experiments of Taylor (1935) and Uberoi & Corrsin (1952). Measurements taken downstream of a heated line source in homogeneous, isotropic turbulence were carried out by Warhaft (1984) and Stapountzis *et al.* (1986). The authors showed that, in isotropic turbulence, the development of the mean thermal wake can be divided into three stages corresponding to different times t: i) a molecular diffusive range ($t \ll \alpha/\langle v^2\rangle$, where $\langle v^2\rangle$ is the velocity variance in the transverse direction), in which the width of the mean temperature profile, σ_{mean}, increases as $\sqrt{t}$, ii) a turbulent

convective range ($\alpha/\langle v^2 \rangle \ll t \ll t_L$, where t_L is the Lagrangian integral time-scale) in which the growth of σ_{mean} is linear in time, and iii) a turbulent diffusive range ($t \gg t_L$) where σ_{mean} is proportional to $t^{(2-n)/2}$ (with $n \approx 1$ being the decay exponent of the velocity field). Subsequently, Karnik & Tavoularis (1989) investigated the evolution of a thermal plume in a homogeneous (but non-isotropic) turbulent shear flow. In contrast with grid turbulence, there is a continuous supply of kinetic energy from the mean shear to the turbulence, ensuring that the turbulence does not decay in this flow. The authors observed that the decay of the scalar fluctuations close to the source was not very different from that observed in isotropic turbulence. However, farther downstream, the mean shear affected the scalar statistics, imposing the effect of its large-scale anisotropy on the evolution of the scalar. Chung & Kyong (1989) also investigated the dispersion of a turbulent temperature field behind a line source in a homogeneous turbulent shear flow. Their goal was to provide experimental data for the assessment of third-order transport models. The mean and r.m.s. scalar profiles were found to exhibit nearly Gaussian distributions except for a minor degradation in the center region of the r.m.s. temperature profile. Livescu *et al.* (2000) used Direct Numerical Simulations (DNSs) to study the development of the scalar plume produced by a line source in decaying homogeneous, isotropic turbulence. Their study focused on a statistical analysis of moments of different orders and confirmed the experimental results of Warhaft (1984).

Although previous work in homogeneous flows has drastically increased our understanding of the mixing of scalars emitted from sources at small scales, their applicability to engineering and natural flows remains somewhat limited given that almost all "real" flows (e.g. jets, boundary layers, duct flows) are inhomogeneous. Consequently, scalar dispersion within inhomogeneous flows

has also been studied. To this end, Fackrell & Robins (1982) investigated the evolution of a thermal plume emitted from a point source in a turbulent boundary layer. The authors reported measurements of the variance, intermittency, peak concentration values, probability density function and spectra of the scalar field. They showed that most of the fluctuations are produced in the vicinity of the source, and that the maximum amplitude of the fluctuations is source-size dependent. Raupach & Legg (1983) studied the dispersion of a thermal plume emitted in a turbulent boundary layer from a line source. Their work was focused on testing first- and second-order closure models. To this end, they measured the dissipation rate of the temperature fluctuations by assuming local isotropy and using Taylor's hypothesis ($\varepsilon_{\theta iso} \approx (3\alpha/\langle U\rangle^2)\langle(\partial\theta/\partial t)^2\rangle$, where angular brackets represent averaged quantities). They reported that their measurements of ε_θ were 20% below its value inferred from the scalar variance budget. Paranthoën *et al.* (1988) studied the evolution of the temperature field downstream of a line source in a turbulent boundary layer and in a planar jet. They reported mean and r.m.s. profiles of the temperature field and proposed a rescaling scheme based on the temporal integral Lagrangian scale of the vertical velocity fluctuations. The scheme was shown to be efficient in rescaling the mean profiles, but not the r.m.s. profiles. Tong & Warhaft (1995) studied the dispersion and mixing of temperature fluctuations emitted in the self-similar region of an axisymmetric turbulent jet from two heated annular (ring) sources. The two sources were used to study the mixing of two independently introduced scalar fields. Their results contrasted with those obtained in grid turbulence (Warhaft, 1984), where the mixing and dispersion was slower. The authors also showed that far downstream of the jet exit, the scalar field becomes independent of its method of introduction into the flow. Tong & Warhaft (1995) also examined the relationship between the integral-scale

and dissipation-scale fluctuations in the far-field. Even though they reported that large- (θ^2) and small-scale ($\Delta\theta^2$) quantities become less coupled as the Reynolds number increases, conditional expectations of $\Delta\theta^2$ on θ exhibited a significant dependence of the former on the latter. Rosset *et al.* (2001) investigated the transport of temperature behind a line source in a turbulent jet and a turbulent boundary layer over a flat plate. The authors were particularly interested in the behavior of the scalar dissipation rate, ε_θ. Near the source, they observed a large anisotropy of the dissipative scales, which was explained by the high temperature gradient imposed by the source and by the flapping of the thermal wake. This anisotropy persisted downstream in the off-center region of the plume. However, in the central part of the plume, they reported a return to isotropy of the different components of ε_θ. Rosset *et al.* derived a model to estimate the return-to-isotropy time-scale and proposed arguments to explain this phenomenon. Nevertheless, they ultimately remarked that the details of the process remain to be understood.

One subset of inhomogeneous flows is of particular interest. Fully-developed, turbulent duct flows, of circular or high-aspect-ratio cross-sections, are only inhomogeneous in one (the wall-normal) direction. Such a characteristic simplifies the analysis given that the inhomogeneity of the underlying velocity field is limited to one direction (as opposed to two or three). Brethouwer *et al.* (1999) used DNS to study the turbulent mixing of a passive scalar in fully-developed turbulent pipe flow. In their work, the scalar was released from a point source at the centreline of the pipe. They presented large-scale statistics, i.e., mean and r.m.s. concentration profiles, turbulent fluxes and probability density functions (PDFs) which, in this case, at the center of the flow, compared favorably to experimental data from grid-turbulence. The release of a

scalar field from a line source in a turbulent channel flow has also been investigated in the experiments of Lavertu & Mydlarski (2005). The authors studied the evolution of the temperature field in turbulent channel flow. The line source was oriented in the spanwise (z) direction resulting in a thermal plume that was statistically two-dimensional. The authors reported large-scale statistics measured at different downstream locations in the scalar plume and for several wall-normal locations of the line source. They observed significant differences from the results in grid turbulence, which were attributed to the inhomogeneity of this flow in the wall-normal direction. Vrieling & Nieuwstadt (2003) and Costa-Patry & Mydlarski (2008) both studied the passive scalar mixing downstream of two line sources in fully-developed turbulent channel flow using DNSs and experiments, respectively. They showed that mean temperature values can be inferred from measurements downstream of a single source. However, the combined variance of two sources cannot be obtained by adding the variance of the individual sources. In contrast with Lavertu & Mydlarski (2005) and Costa-Patry & Mydlarski (2008), Bakosi *et al.* (2007) used probability density function methods and the IECM (interaction by exchange with the conditional mean) model to investigate the dispersion of a passive scalar released continuously from a concentrated source in a turbulent channel flow. One-point statistics of the scalar field were compared to the DNS data of Abe *et al.* (2004) and the experimental data of Lavertu & Mydlarski (2005). The width of the mean scalar profiles obtained with the IECM model were larger than those measured in the experiments at different downstream locations from the source. Boppana *et al.* (2012) performed Large-Eddy Simulations (LESs) of the dispersion of a scalar from a line source in a turbulent channel flow. They reported mean and r.m.s. profiles and PDFs of the scalar fluctuations. Their results were also compared to the experiments of Lavertu

& Mydlarski (2005), which exhibited discrepancies for both the width and location of the profile's peak. Note that in contrast to Bakosi *et al.* (2007), the widths of the mean profile computed by Boppana *et al.* (2012) were smaller than those obtained from Lavertu's experiments. In addition, Boppana *et al.* (2012) observed a double peak in the r.m.s. profiles at downstream locations from the source ($x/h > 7.4$) that were not reported in the experiments. PDFs of both the LESs and experiments were in good agreement, except for the thermal fields generated by the centreline source. Lepore & Mydlarski (2011) studied the downstream evolution of a three-dimensional thermal plume in the turbulent channel flow released by a line source oriented in the wall-normal direction. They examined in detail the mean and fluctuating temperature fields at different locations in the thermal plume to highlight the differences between lateral and transverse dispersion. Lastly, Mydlarski *et al.* (2007) focused on the dissipation rate of a scalar field emitted from a line source in a turbulent channel flow. The authors confirmed that small-scale anisotropy is amplified at the interfaces between the plume and the ambient fluid. They reported that a large anisotropy occurs in regions of high turbulent intensity and their results showed that there may exist a competition between mechanisms that amplify and destroy anisotropy. However, they did not directly measure ε_θ, but rather inferred it from the scalar variance budget (given certain assumptions). In contrast to their work, the present work directly measures (all three components of) the scalar dissipation rate, using both experiments and numerical simulations.

3.5 Experimental apparatus

The experiments were conducted in the same open-circuit channel as the one used by Lavertu & Mydlarski (2005), Costa-Patry & Mydlarski (2008) and

Lepore & Mydlarski (2011). The air flow is supplied by a Hudson Buffalo centrifugal blower powered by a 7.5 h.p. electric motor whose speed is monitored by an ABB ACS 600 controller. The air flow is filtered at the inlet of the motor to prevent particles (of diameter greater than 3 μm) from entering the channel. A flexible rubber coupling is used to join the blower output to the entrance of the flow conditioning section to minimize the transmission of any blower vibrations to the flow conditioning section. The latter consists of a wide-angle diffuser, a settling chamber and a contraction. After exiting the contraction, the flow that enters the channel is uniform and has a low-turbulence-intensity (0.25%).

The test section is 8 m long and has a large aspect ratio, i.e. the height of the channel in the spanwise (z) direction is large (1.1 m) compared to its width ($2h = 0.06$ m) in the wall-normal (y) direction. Consequently, the flow is statistically independent of z, away from the top and bottom walls of the channel. The development of the flow is accelerated by the addition of two 3 mm diameter cylindrical rods (located 3 mm from each wall, at the entrance of the test section) that trip the boundary layers that form on the test section walls. At the downstream end of the test section, where the measurements are recorded, the flow is fully-developed with a mean flow in the downstream (x) direction and zero mean wall-normal (V) and lateral (W) velocities. In the fully developed region, the flow is statistically stationary and one-dimensional with velocity statistics depending only on the wall-normal distance (y). Note that such a flow is statistically symmetric about the mid-plane. Lastly, 7.5 cm of honeycomb mesh (of 5 mm cell size) is used at the outlet to prevent perturbations from outside the channel from being communicated upstream, into the channel. The flow conditions are listed in table 3–1.

		Exp.	DNS
$\langle U \rangle_{y/h=1}$	[m/s]	5.3	-
$u_{rms_{y/h=1}}$	[m/s]	0.22	-
u_τ	[m/s]	0.26	-
$\eta_{y/h=1}$	[m]	0.28×10^{-3}	-
$Re(= \langle U \rangle_{y/h=1} h/\nu)$		10600	3600
$Re_\tau(= u_\tau h/\nu)$		520	190
$y_s/h = 0.17$		$y_s^+ = 88$	$y_s^+ = 33$
$y_s/h = 1.0$		$y_s^+ = 520$	$y_s^+ = 190$

Table 3–1: Flow parameters. Properties of the flow considered in the experiments and numerical simulations, and source locations in terms of wall units. $\nu = 15 \times 10^{-6}\ m^2/s$.

In the test section, the scalar (temperature) is injected into the flow by heating a fine line source. The latter is a 0.127 mm diameter Ni-Cr wire extended across the spanwise direction of the test section at wall-normal locations of $y_s/h = 1.0$ (channel centreline) and $y_s/h = 0.17$ (near-wall region). The wire was heated electrically by a DC power supply and the power consumption was continuously monitored so that the energy released into the flow remained equal to 45 W/m.

The temperature fluctuations, θ, and their dissipation rate, ε_θ, were measured by means of cold-wire thermometry. The sensors were inserted into the channel from its outlet using a (915 mm-long) probe support (TSI-1155-36). The accurate positioning of the sensor in the wall-normal direction was ensured by means of a precision transversing mechanism driven by computer controlled stepper motor. The minimum step increment was 0.01 mm. The sensor consisted of two parallel 90%–platinum/10%–rhodium wires of 0.63 μm-diameter mounted on a TSI 1244 probe. Variations of the sensor temperature are linearly proportional to its electrical resistance (over small ranges) and are measured by a cold-wire thermometry circuit designed by Lemay & Benaïssa

(2001). The output signals of the cold-wire thermometer were *i)* amplified and filtered by a Krohn-Hite 3384 8-pole filter, and *ii)* digitized using a 16 bit ($\pm 5V$) National Instruments PCI 6036E data acquisition card. The acquisition procedure was undertaken using LabVIEW virtual instruments. Depending on the wall-normal location of the probe, the sampling frequency (2.5 times the low-pass filter frequency) was in the range $[5-10]$ kHz and the sampling time was fixed at 200 s for each locations. The length-to-diameter ratio of the cold-wire sensors was approximately 800 (i.e. $l_{\text{wire}} \approx 0.5$ mm) and its frequency response was approximately 5 kHz when operated in a 5 m/s flow. Note that the temporal resolution of the wire was sufficient given that the Kolmogorov frequencies, $f_\eta = \langle U \rangle / (2\pi\eta)$, of the flow studied herein did not exceed 4 kHz. In addition, the (temporal resolution) correction proposed by Lemay & Benaïssa (2001) was applied to the acquired data. However, the effect of this correction was relatively small as it increased the estimate of the temperature dissipation by less than 1% when measured at the farthest downstream location and by 5% when measured at the location closest to the line source.

The scalar derivative $(\partial\theta/\partial x)$ in the downstream direction was estimated using Taylor's hypothesis in conjunction with the time derivative of temperature $(\partial\theta/\partial t)$. This measurement required only a single cold-wire, whereas, two wires were needed to estimate the derivatives $(\partial\theta/\partial y)$ and $(\partial\theta/\partial z)$ in the wall-normal and spanwise directions, respectively. Zhou *et al.* (2003) investigated the effects of the separation between the two wires and found that the spectra of temperature derivatives are significantly affected by the electronic noise contamination from one wire to the other when the separation is smaller than 3η. In addition, they recommended the use of a correction method similar to that of Wyngaard (1969) when the wire separation was larger than 3η. As a consequence, we designed our sensors so that the separation between the

two wires was nominally, 3η (= 0.75 mm), being slightly smaller than 3η at the channel centreline, and slightly larger near the wall, as η is a function of wall-normal position.

3.6 Numerical simulations

Direct numerical simulations were also performed to replicate the experiments described in §3. The simulations solved the continuity, Navier-Stokes and advection-diffusion equations, which govern the hydrodynamic and the scalar fields over a numerical domain representing a channel delimited by two parallel, flat plates. The boundary conditions for the velocity field are periodic in the streamwise (x) and spanwise (z) directions, and no-penetration and no-slip conditions at the wall. The streamwise mean pressure gradient that drives the mean flow in the x-direction is adjusted dynamically to maintain a constant mass flux through the channel. The boundary conditions for the scalar field are periodic in the spanwise (z) direction, inflow/outflow at the inlet/outlet of the channel, and adiabatic (no-flux) at the walls. The continuity and Navier-Stokes equations are solved first using a spectral method, whereas the advection-diffusion equation is subsequently solved using a flux-integral method.

Spectral methods have become a classical tool to simulate turbulent channel flows. We therefore took advantage of their high-accuracy and kinetic energy conservation properties to solve the hydrodynamic field. However, the use of a spectral scheme is not suitable for the solution of the scalar field considered herein because the scalar is injected by means of a line source, i.e. a singularity that introduces a sharp-gradient in the scalar field. It is well known that, in the presence of sharp-gradients, the convergence rate of spectral schemes deteriorates to first-order when spurious oscillations develop in the vicinity of the source (Gibbs phenomenon). In addition, and in contrast to the hydrodynamic

field, the scalar field is not homogeneous in the streamwise direction. Spectral methods lose their attractiveness when solving non-periodic problems. (See, for example, Simens *et al.*, 2009, for details.)

To solve the three-dimensional continuity and Navier-Stokes equations, the code named "Channelflow" was used (Gibson *et al.*, 2008; Gibson, 2010*b*, `http://channelflow.org/`). Channelflow, licensed under the GNU GPL, uses a spectral discretization in space (Fourier $\times$ Chebyshev $\times$ Fourier) and a finite difference discretization in time (Runge-Kutta third-order). We implemented a flux-integral scheme, 3DFLUX, to solve the advection-diffusion equation (Germaine *et al.*, 2013). 3DFLUX is a high-order, three-dimensional, conservative, monotonicity preserving numerical solver. It is nominally third-order in space and second-order in time. The scalar field is injected via a line source that is simulated by a string of nodes having a constant source term and located on a straight line, oriented parallel to the z-axis. Note that, as a consequence of the line source orientation, the scalar field is statistically homogeneous in the spanwise direction.

The velocity field is precomputed and then used as an input to solve the advection-diffusion equation. In Channelflow, the velocity field has a spectral representation with a resolution given by its number of Fourier and Chebyshev modes. In 3DFLUX the computational domain is discretized with a number of non-overlapping control volumes or cells. The scalar field is discretized at the centre of each cell, whereas the components of the velocity fields are stored at the centre of the faces of each cell (staggered grid). The velocity field produced by Channelflow is passed to 3DFLUX by interpolating the spectral representation of the velocity field on each face of the 3DFLUX grid.

The interpolation of the divergence-free velocity field from a spectral to a finite-volume representation is a crucial and delicate step. Such interpolations

	velocity	scalar $y_s/h = 1.0$	scalar $y_s/h = 0.17$
$L_x \times L_y \times L_z$	$2\pi h \times 2h \times \pi h$	$2\pi h \times 2h \times \pi h$	$2\pi h \times 2h \times \pi h$
$L_x^+ \times L_y^+ \times L_z^+$	$1187 \times 378 \times 594$	$1187 \times 378 \times 594$	$1187 \times 378 \times 594$
$N_x \times N_y \times N_z$	$256 \times 193 \times 192$	$514 \times 195 \times 194$	$258 \times 390 \times 194$
$\Delta x^+, \Delta y^+, \Delta z^+$	$4.64, 0.025 - 3.1, 3.1$	$2.32, 1.96, 3.1$	$4.64, 0.98, 3.1$
$\Delta x^*, \Delta y^*, \Delta z^*$ at $y/h = 1.0$	$1.25, 0.83, 0.84$	–	–
$\Delta x^*, \Delta y^*, \Delta z^*$ at $y/h = 0.17$	$2.40, 0.88, 1.60$	–	–
$\Delta x^\bullet, \Delta y^\bullet, \Delta z^\bullet$ at $y/h = 1.0$	–	$0.50, 0.42, 0.66$	$0.99, 0.21, 0.66$
$\Delta x^\bullet, \Delta y^\bullet, \Delta z^\bullet$ at $y/h = 0.17$	–	$0.95, 0.80, 1.27$	$1.91, 0.40, 1.27$
t_{sam}^+	2770	665	665

Table 3–2: Details of the numerical grids for the computation of velocity, and scalar fields with two different source locations. The superscript "+" indicates the normalization by the viscous length (ν/u_τ) or time (ν/u_τ^2) scale, and the superscripts "$*$" and "$\bullet$" are used for the normalization by the Kolmogorov (η) and Corrsin (η_θ) length scales, respectively, estimated at $y/h = 1.0$ and 0.17 as specified.

have been the subject of several publications in the last decade (see for example Balsara, 2001; Li & Li, 2004; Chamecki *et al.*, 2008). The method proposed by Chamecki *et al.* (2008) is efficient only when the grids of the two different discretization methods are identical, and therefore not applicable herein. We devised our own method in which we first used a spectral (exact) interpolation to compute the value of the velocity components at nine points on each face, i.e. one at the center, four at the corners, and four at the mid-side of the edges of the faces. Then, we computed the value of each velocity component at the face of each cell by averaging the nine interpolated values. Finally, we applied a very small correction to the $u-$component of the velocity field to guarantee the exact divergence-free condition. Note that *i*) the choice of the $u-$component is arbitrary (it could have been the $w-$component), and *ii*) this correction has a minuscule impact on the velocity field, as it modifies the interpolated instantaneous values of the $u-$component by less than 0.01%.

The simulations of the velocity and scalar fields were both performed without turbulence models, by resolving the entire range of spatial scales. The computational conditions are reported in table 3–2 for the (i) hydrodynamic field, and (ii) scalar field for two source locations ($y_s/h = 1.0$ and $y_s/h = 0.17$). These DNSs require that the computational domain be large enough to capture the integral scales and the spatial resolution be small enough to resolve, as accurately as possible, the dissipative scales. On the one hand, the large scales are correctly represented when the two-point correlations in the streamwise and spanwise directions are zero, respectively, at the half-length and half-height of the domain (Kawamura *et al.*, 1998; Moser *et al.*, 1999). The domain size selected herein is the same as in Kawamura *et al.* (1998), Moser *et al.* (1999) and Schwertfirm & Manhart (2007). On the other hand, the Kolmogorov (i.e. smallest) length scale should ideally be resolved. However, it has been claimed that this requirement is often too stringent. Moin & Mahesh (1998) noted that the smallest resolved length scale is required to be on the order of η but not equal to η. They further reported that very good agreement of *large-scale* statistics can be obtained between DNSs and experiments even though the Kolmogorov scales are not fully resolved in the simulation. Kawamura *et al.* (1998) validated the resolution of their simulations by showing substantial drop-offs in the one-dimensional energy spectra at high-wave numbers.

Traditionally, the goal of most experiments is to resolve the scales given by η. This being said, recent work has taken advantage of the constantly increasing computational power to simulate turbulent scalar mixing at spatial resolutions finer than η. For example, Schumacher *et al.* (2005) studied the fine structures of homogeneous and isotropic turbulent scalar mixing using high-resolution simulations (the grid spacing being smaller than η by a factor of two). They showed that when large fluctuations of ε exist, a spatial resolution

based on η (defined using its average value) incorrectly predicted the small-scale statistics. Kozuka *et al.* (2009) and Galantucci & Quadrio (2010) both performed DNSs of turbulent scalar mixing in channel flows at high resolution. Galantucci & Quadrio (2010) carried out three DNSs at increasing spatial resolutions that they labelled Low, Medium and High. The Low resolution is comparable to the resolution of most wall-turbulence DNSs performed to date (with passive scalars) whereas, in the High resolution simulations, all cell sizes are consistently smaller than η_w, the averaged Kolmogorov length scale evaluated at the wall. The spatial resolution denoted Medium was midway between the two other resolutions. The authors reported several statistics pertaining to the rate of dissipation of the scalar field (mean, variance, and PDFs of ε_θ). They showed that the estimates of ε_θ can increase by 5% when using the High or Medium resolutions instead of the Low one. The resolutions used for the simulations presented herein (see table 3–2) are comparable to the Medium resolution used by Galantucci & Quadrio (2010).

To investigate the resolutions of the smallest scales, we plotted normalized (one-dimensional) dissipation spectra for both the simulations and experiments in figures 3–14 and 3–15. These figures show excellent agreement between the two sets of results, confirming that the numerical simulations are capable of reproducing the dissipative scales measured in the experiments.

To compute the hydrodynamic field, uniform meshes were used in the x- and z-directions whereas a non-uniform mesh (Chebyshev distribution) was adopted in the y-direction. As shown in table 3–2, two different grids were used to discretize the scalar field, depending on the source location. When the source was at the centreline, i.e. $y_s/h = 1.0$, a quasi-homogeneous grid was used given that the scalar plume did not interact with the walls (for the downstream locations studied herein). When the source was near the wall

($y_s/h = 0.17$), the grid resolution was halved in the y-direction to capture the smallest wall-normal fluctuations of the scalar field that occur in the vicinity of the walls. The spatial resolution $(\Delta x, \Delta y, \Delta z)$ of the scalar field generated by the centreline source was, for either grid, smaller than or equal to the Corrsin scale. The spatial resolution of the scalar field generated by the near-wall source is, in the worst case, less than twice the Corrsin scale in the x-direction. However, note that Δy is always smaller than the Corrsin scale.

Lastly, to study the evolution of the scalar field at the farther downstream locations, we adopted a strategy that consisted in connecting several channels in series and computing the solution for the scalar field sequentially, i.e. the outflow of the first channel became the inflow of the second one, and so on. Note that the hydrodynamic field is the same in all channels because of its periodic boundary conditions. In this paper, we limited our computation to two channels, i.e. $(x/h)_{\max} = 2L_x/h$, where L_x is the length of one channel in the x-direction.

3.7 Results

The results are divided into three sections. A few results pertaining to the velocity field are first reported, followed by a thorough discussion of large-scale temperature statistics. Lastly, the small-scale statistics, which comprise the vast majority of the results presented herein, are discussed. Significant emphasis is placed on the evolution of the dissipation rate of the scalar variance, as well as that of its components.

3.7.1 Velocity field

To be consistent with Lavertu & Mydlarski (2005), the experiments were carried out (in the same experimental facility) at $Re_\tau = 520$. However, the simulations were performed at a lower Reynolds number ($Re_\tau = 190$) to resolve all scales while keeping the flow turbulent and the computational effort

feasible. Mean velocity profiles in fully turbulent channel flow from both the experiments and DNSs are plotted in figures 3–3(a) and compared to the numerical results of Moser *et al.* (1999) ($Re_\tau = 180$ and 590) and Abe *et al.* (2001) ($Re_\tau = 180$ and 640). The experiments of Hussain & Reynolds (1975) ($Re_\tau = 640$) are also include for comparison. The mean velocity profile obtained from the present DNS is in very good agreement with those measured in flows at $Re_\tau = 180$. As noted by Kim *et al.* (1987), even if $Re_\tau = 180$ is a relatively low Reynolds number (for a turbulent flow), both linear and logarithmic regions exist and are distinct. Small differences are observed between the experiments and the DNSs. However, these differences can be attributed to the difference in Reynolds number of the flows – a conclusion that is confirmed by the good agreement between the present experimental results and the higher Reynolds number simulations of Moser *et al.* (1999) and Abe *et al.* (2001). These simulations also exhibit smaller values of u^+ for a given location y^+ in the logarithmic region.

The root mean square of the velocity fluctuations is plotted in figure 3–3(b). The data of Hussain & Reynolds (1975), Moser *et al.* (1999) and Abe *et al.* (2001) are once again reported for comparison, where available. The values of the three components (u^+_{rms}, v^+_{rms} and w^+_{rms}) increase with Re_τ and are consistent with differences in the Reynolds number between the present experiments ($Re_\tau = 520$), Moser *et al.* (1999) ($Re_\tau = 590$) and Abe *et al.* (2001) ($Re_\tau = 640$). Furthermore, the present DNS ($Re_\tau = 190$) agrees very well with the results of Moser *et al.* (1999) and Abe *et al.* (2001) (both with $Re_\tau = 180$). In short, figure 3–3(b) shows good agreement between the present and previous data obtained at similar Re_τ. (Note that the peak value of u^+_{rms} measured by Hussain & Reynolds (1975) is somewhat low compared the other results. This discrepancy may be justified by the difficulties in performing these

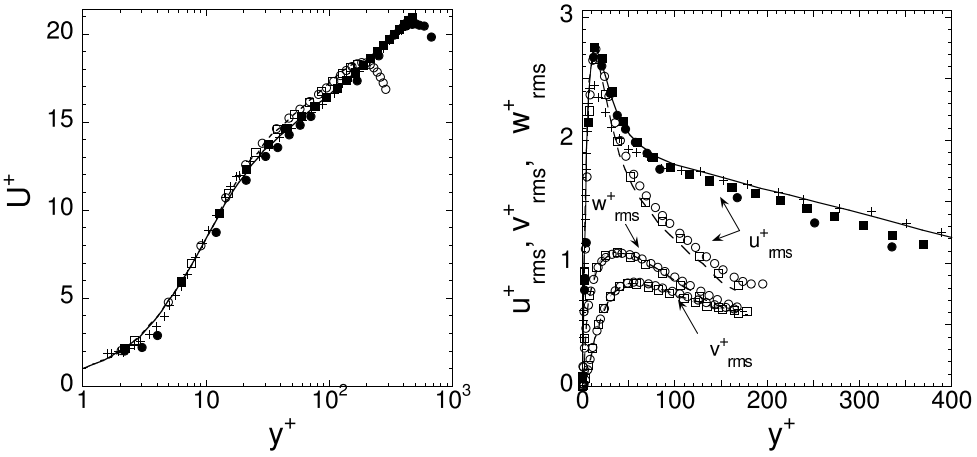

(a) (b)

Figure 3–3: Velocity profiles in fully turbulent channel flow. Mean (a) and r.m.s. (b) velocity profiles (normalized by u_τ) from experiments ($Re_\tau = 520$, (•)), DNSs ($Re_\tau = 190$, (∘)) and compared to the DNSs of Abe *et al.* (2001) ($Re_\tau = 180$, (- - -) and $Re_\tau = 640$, (—)) and Moser *et al.* (1999) ($Re_\tau = 180$, (□) and $Re_\tau = 590$, (■)), and the experiments of Hussain & Reynolds (1975) ($Re_\tau = 640$, (+)).

early near-wall measurements). Finally note that original and interpolated velocity field are indistinguishable. Consequently only the former has been plotted.

3.7.2 Large-scale statistics of the scalar field

In this section, large-scale statistics of the scalar field from experiments and numerical simulations are analyzed and compared with those obtained in Lavertu & Mydlarski (2005). As the experiments were performed at a different Reynolds number than that of the numerical simulations, we normalized the downstream location (x/h) by the ratio $(u_{rms}/\langle U\rangle)^{-1}$ where u_{rms} and $\langle U\rangle$ are the r.m.s. and mean velocities measured at the centreline. Note that this normalization is equivalent to normalizing the flight time from the source by (an approximation of) the integral time scale ($t_L \approx h/u_{rms}$)

$$t/t_L = \frac{(x/\langle U\rangle)}{(\ell/u_{rms})} \approx \frac{(x/\langle U\rangle)}{(h/u_{rms})} = \frac{(x/h)}{(\langle U\rangle/u_{rms})}. \tag{3.1}$$

The mean temperature profiles at three downstream locations behind the line source ($t/t_L = 0.08,\ 0.2$ and 0.4) are shown in figures 3–4(a) and 3–4(b) for the $y_s/h = 1.0$ and 0.17 source locations, respectively. Given that mean temperature excesses can be difficult to measure accurately due to drift in the free-stream temperature, we used the technique proposed in Lepore & Mydlarski (2011), which consists of sequentially measuring the free-stream temperatures at the same location, immediately after measuring the mean temperatures, to estimate the "instantaneous" temperature mean excess, which accounts for drifts in the free-stream (i.e. ambient, room) temperature.

For the centreline source location ($y_s/h = 1.0$), excellent agreement between the experiments and numerical simulations is observed, and the mean profiles are well approximated by Gaussian curve fits. We note that the large-eddy simulations of Boppana *et al.* (2012), carried out at $Re_\tau = 520$ (i.e., the same value as the experiments herein), did not agree as well with the experiments of Lavertu & Mydlarski (2005) (that give very similar results to those herein – to be discussed shortly in the context of figures 3–6-3–9) and underestimated the plume width – see their figure 10(c). This presumably derives from their under-resolved transverse velocity fluctuations – they obtained values of $\langle v^2 \rangle$ at $y/h = 1$ that were 20% lower than the those obtained by Moser *et al.* (1999) at $Re_\tau = 590$ – see figure 5 in Boppana *et al.* (2012). Although a 20% underestimate of $\langle v^2 \rangle$ may not seem egregious, the observed excellent agreement between the present DNS and experiments implies that accurate estimates of $\langle v^2 \rangle$ are critical to reliably predicting the evolution of the plume. We furthermore remark that the PDF method simulations of Bakosi *et al.* (2007) overestimated the width of the mean profiles for a centreline source. However, the explanation in this case is less clear, especially given that they

also under-resolved $\langle v^2 \rangle$ (see their figure 1(b)), as noted by Boppana *et al.* (2012).

Similarly, good agreement between the experimental and numerical mean temperature profiles is obtained for the near-wall line source ($y_s/h = 0.17$). However, for the farthest downstream distance considered herein ($t/t_L = 0.4$) the experimental mean temperature profile is wider than the numerical one. Far downstream of the source, the (two-dimensional) plume grows and becomes wider in the transverse direction. One edge of the plume is mixed with the cold flow contained in the central region of the channel, whereas the other edge comes in contact with the (nominally) adiabatic walls. Consequently, the plume contains a hot region near the wall and a colder region away from the wall. The discrepancies observed for $t/t_L = 0.4$ in figure 3–4(b) are consistent with an energy loss (in the experiments) to the walls due to the latter not being perfectly adiabatic (because ΔT_{peak} is smaller than it should ideally be in the experiments due to the heat transfer from the plume to the wall). For the case of the centreline source, both sides of the plume do not come in contact with the channel walls and the mean temperature profile remains symmetric about the line source location, in excellent agreement with the numerical simulations. Like for the case of the centreline source, the large-eddy simulations of Boppana *et al.* (2012) were found to underestimate the width of the mean plume when $y_s/h = 0.17$ at all downstream locations – see their figure 10(b). This presumably derives from their under-resolved transverse velocity fluctuations, combined with the above-mentioned heat transfer to the wall in the experiments, which results in overly wide (normalized) plume widths farther downstream.

The simulations also exhibit a shift in the peak of the mean profile towards the region of lower velocity (i.e. towards the wall) when $y_s/h = 0.17$. A similar

shift was reported in Karnik & Tavoularis (1989). At the wall, the simulated mean temperature profiles must all exhibit $\partial\langle T\rangle/\partial y|_{y=0} = 0$, consistent with the adiabatic boundary conditions imposed in our simulations. Experimental measurements in the range $0 < y/h < 0.1$ were, however, not possible due to interference of the probe with the wall.

The transverse profiles of the r.m.s. temperature fluctuations, θ_{rms}, normalized by their peak values, $\theta_{rms-peak}$, are reported in figures 3–5(a) and 3–5(b) respectively for $y_s/h = 1.0$ and 0.17 at three downstream locations: $t/t_L = 0.08,\ 0.2$ and 0.4. The experimental and numerical results collapse well for both line source locations, in addition to being well approximated by Gaussian curve fits. At $y_s/h = 1.0$, the peaks of the fluctuations remain behind the line source, as expected, by the underlying symmetry of this flow. However, for $y_s/h = 0.17$, a drift of the peak towards the centreline is clearly observed. Similar drifts have been reported in Fackrell & Robins (1982), Raupach & Legg (1983) and Lavertu & Mydlarski (2005). Also note the excellent agreement between the experiments and simulations at $t/t_L = 0.4$ for the case of the near-wall source. The good collapse of the two r.m.s. profiles (when normalized by their peak value) reaffirms our hypothesis that the disagreement observed in figure 3–4(b) for the mean profiles at the same location arises from an underestimate of ΔT_{peak}. For a centreline source, the large-eddy simulations of Boppana *et al.* (2012) underestimate the plume width, similar to their results for the mean profile. For the case of the source at $y_s/h = 0.17$, the r.m.s. profiles of Boppana *et al.* (2012) are of a similar shape, however are offset and closer to the wall. Given that the r.m.s profiles are related to the mean profiles (i.e., the former can be predicted from the latter using gradient transport theory, for example), such a result is consistent with their mean

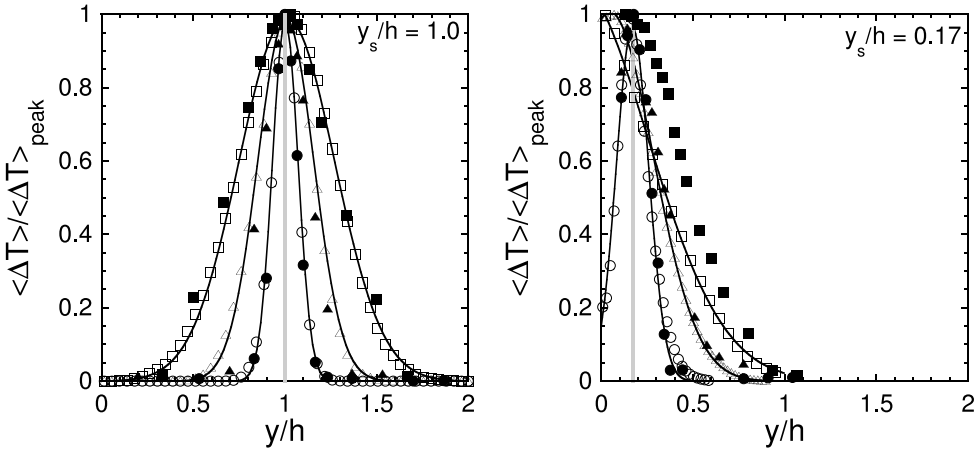

(a) (b)

Figure 3–4: Non-dimensionalized mean temperature excess profiles for two line source locations, $y_s/h = 1.0$ (a) and $y_s/h = 0.17$ (b). Experiments (solid symbols) and DNSs (open symbols) are reported at several downstream locations: $t/t_L = 0.08$, (• and ∘); $t/t_L = 0.2$, (▲ and △); $t/t_L = 0.4$, (■ and □), respectively. The vertical line indicates the transverse location of the source and the solid lines are the best fit Gaussian curve fits to the numerical data.

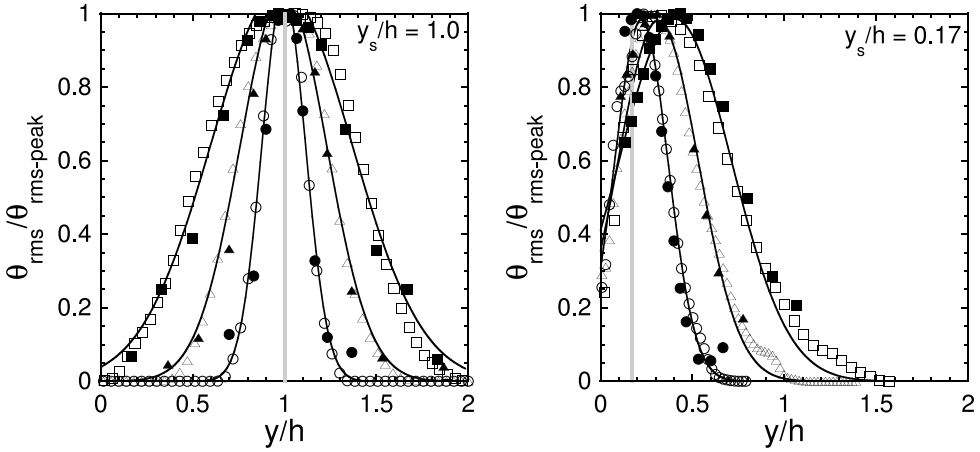

(a) (b)

Figure 3–5: Non-dimensionalized r.m.s. temperature excess profiles for two line source locations, $y_s/h = 1.0$ (a) and $y_s/h = 0.17$ (b). Experiments (solid symbols) and DNSs (open symbols) are reported at several downstream locations: $t/t_L = 0.08$, (• and ∘); $t/t_L = 0.2$, (▲ and △); $t/t_L = 0.4$, (■ and □), respectively. The vertical line indicates the transverse location of the source and the solid lines are the best fit Gaussian curve fits to the numerical data.

profiles that are not as wide. Similar to the mean profiles, the simulations of Bakosi *et al.* (2007) overpredicted the width of the r.m.s.profiles.

The double-peaked r.m.s. profile in the vicinity of the source reported by Warhaft (1984) and Karnik & Tavoularis (1989) for homogeneous flows is also observed for the simulations (not shown). The double peak remains up to $t/t_L = 0.1$ ($x/h = 2.0$), after which the profile becomes single-peaked. Note that when $y_s/h = 0.17$ the double peak is not symmetric, as it must be for the centreline source case, with the near-wall peak having a lower magnitude. Lastly, note that experiments were not performed close enough to the line source to observe double-peaked θ_{rms} profiles.

Figures 3–6 and 3–7 respectively show the downstream decay of the peak of the mean and r.m.s. profiles normalized by a reference temperature

$$\langle \Delta T \rangle_{\text{ref}} = \frac{\int_0^{2h} \rho c_p \langle U \rangle \langle \Delta T \rangle \mathrm{d}y}{\int_0^{2h} \rho c_p \langle U \rangle \mathrm{d}y} \tag{3.2}$$

(see Incropera *et al.*, 2007, p.495), where ρ and c_p are, respectively, the density and the specific heat at constant pressure of air, and where $\langle U \rangle = \langle U(y) \rangle$ is the mean velocity. Note that the above definition of $\langle \Delta T \rangle_{\text{ref}}$ is different from that proposed by Rosset *et al.* (2001): $\langle \Delta T \rangle_{\text{ref}} = (P_s/l_s)/(\rho c_p U_s d_s)$, where P_s/l_s is the electric power per length unit injected via the line source, U_s is the mean longitudinal velocity at the source location, and d_s is the source diameter. Such a reference temperature may not be appropriate if both the diameter of the source and the input power change. For instance, when d_s and P_s are each multiplied by two (assuming that the change of diameter has a negligible impact on the temperature profiles, which is reasonable for a very small diameter line source like those used herein), $\langle \Delta T \rangle_{\text{ref}}$ should also be doubled to maintain a consistent normalization, which is not the case using their definition.

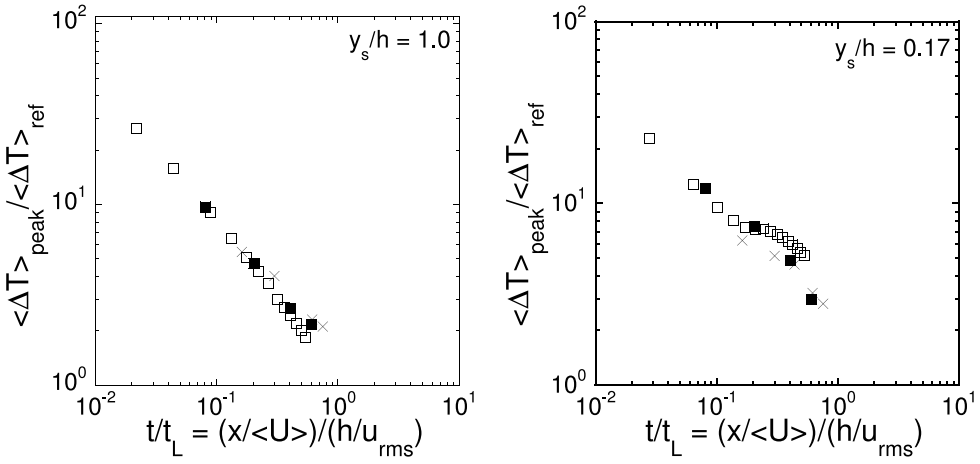

(a) (b)

Figure 3–6: Downstream evolution of the non-dimensionalized peak mean temperature for two line source locations: $y_s/h = 1.0$ (a) and $y_s/h = 0.17$ (b). Experiments (■), DNSs (□) and Lavertu & Mydlarski (2005) (×).

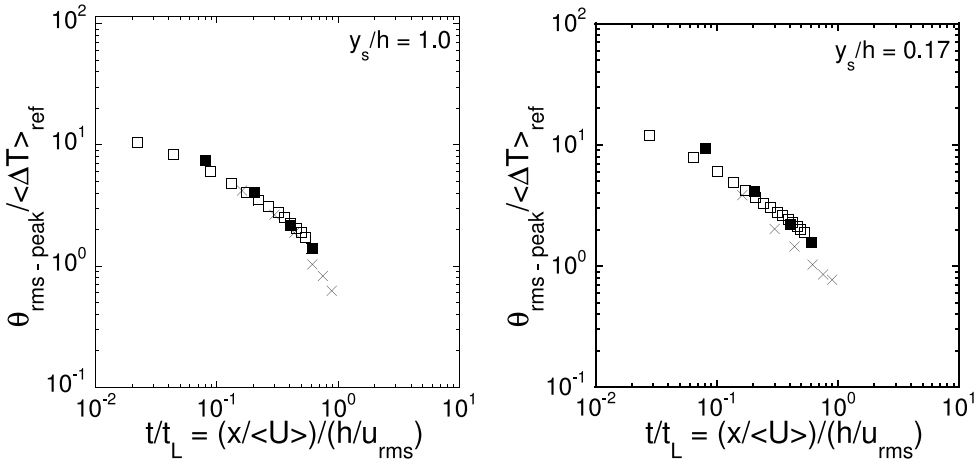

(a) (b)

Figure 3–7: Downstream evolution of the non-dimensionalized peak r.m.s. temperature for two line source locations: $y_s/h = 1.0$ (a) and $y_s/h = 0.17$ (b). Experiments (■), DNSs (□) and Lavertu & Mydlarski (2005) (×).

Figures 3–6 and 3–7 show good agreement between the numerical and experimental results – both the present ones and those of Lavertu & Mydlarski (2005). We note that the plateaus observed in figure 3–6(b) are a consequence of the adiabatic walls. The downstream locations of the plateaus correspond to the locations at which the peak "encounters" the wall, and subsequently stops spreading on that side. Due to the adiabatic boundary conditions at the wall, the peak remains at $y = 0$ for all subsequent downstream locations. A similar plateau was observed for plumes emanating form a near-wall source in Boppana *et al.* (2012). Such a plateau, however, was absent in the case of the centreline source, as the downstream distances studied herein were not large enough for the plume to have grown sufficiently for its edges to interact with the channel walls.

The downstream evolution of the half-width of the mean and r.m.s. profiles are plotted in figures 3–8 and 3–9, respectively, for the two source locations. The standard deviations σ are determined by best fitting a Gaussian curve fit to the data of figure 3–4. (Note that the standard deviation of the Gaussian profile is linearly related to its half-width.) Once again good agreement between experimental and numerical results is obtained. Note that in figure 3–8(b), the standard deviation of the numerical results tends to be larger than that of the experiments for the farthest downstream distance present herein, in contrast with the results of figure 3–4(b). This difference in fact derives from the fact that a Gaussian curve fit is not an especially accurate fit far downstream of the line source.

To complement the preceding analysis of large-scale statistics of the scalar field, we plot in figure 3–10 the instantaneous temperature fields generated by our DNS downstream of both a centreline and near-wall line source. Note the "holes" in the temperature field for the plume emanating from the centreline

source. Such holes are absent in the plume emanating from the near-wall source given the different nature of the mixing near the wall (including a reduced tendency of the plume to flap). The presence of the wall i) limits the plume's growth on one side, ii) is the cause of the flow's inhomogeneity (which is strongest near the wall), and iii) affects the mixing, as will be further discussed.

3.7.3 Small-scale statistics of the scalar field

We now proceed to investigate the small-scale structure of the scalar field. Both experiments and numerical simulations are used in our analysis. We present statistics at six locations, denoted by the crosses in figure 3–11. Three measurements were performed downstream of the line source, whereas the other three locations are closer to the plume edges. Note that, for the sake of clarity, subsequent figures are arranged in a similar pattern to those of the measurement locations in figure 3–11.

3.7.3.1 Spectra of θ, ε_θ and $\partial\theta/\partial x_\beta$

We begin by plotting the one-dimensional longitudinal power spectra of the scalar fluctuations, $E_\theta(\kappa_1)$, where κ_1 is the longitudinal wavenumber. Results are presented for six downstream locations for the two line source locations studied herein, $y_s/h = 1.0$ and 0.17, in figures 3–12 and 3–13, respectively. The experimental results are obtained from time series, which provide Eulerian time spectra, $E_\theta(f)$. Eulerian spatial spectra, $E_\theta(\kappa_1)$, are obtained using Taylor's hypothesis $E_\theta(\kappa_1) = (\langle U\rangle/(2\pi))E_\theta(f)$, where $\kappa_1 = 2\pi f/\langle U\rangle$. Taylor's hypothesis is a reasonable approximation in most regions of the flow where $u_{rms}/\langle U\rangle < 10\%$. (See Sreenivasan *et al.*, 1977; Prasad & Sreenivasan, 1990, for example.) For consistency with the experiments, the numerical spectra presented herein were also computed from time series, so as not to introduce

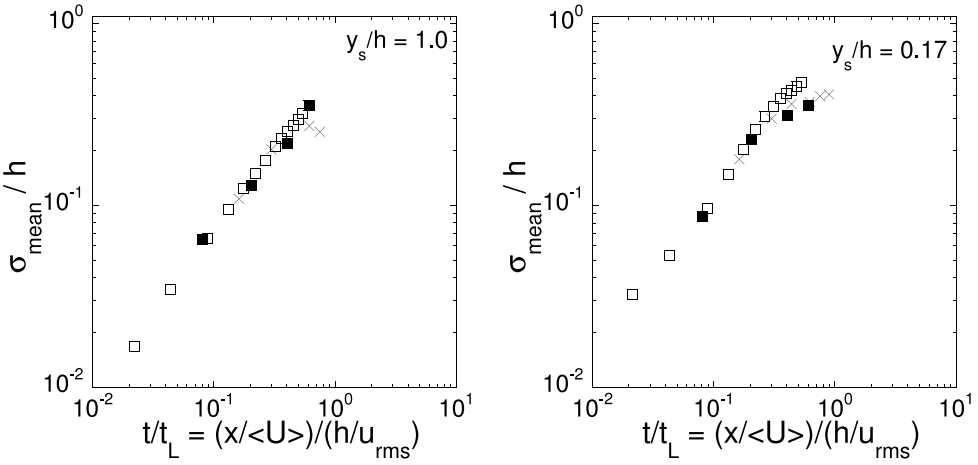

(a) (b)

Figure 3–8: Downstream evolution of the non-dimensionalized width of the mean temperature profiles for two line source locations: $y_s/h = 1.0$ (a) and $y_s/h = 0.17$ (b). Experiments (■), DNSs (□) and Lavertu & Mydlarski (2005) (×).

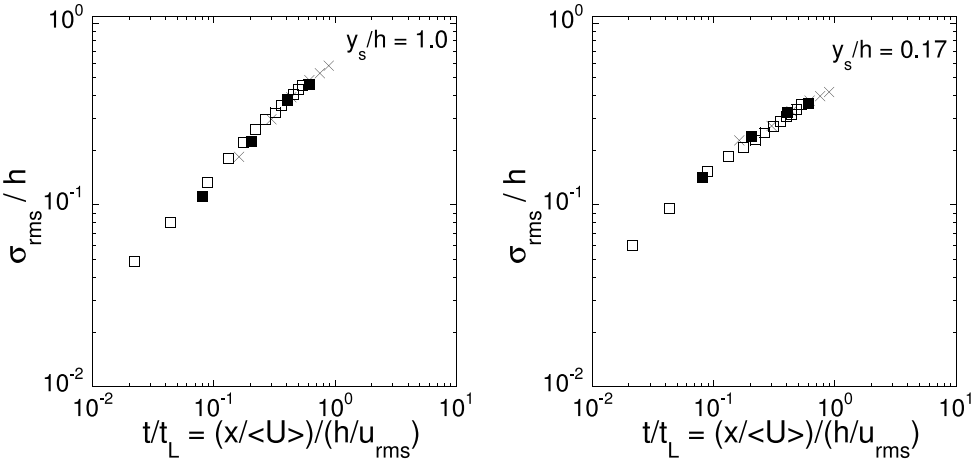

(a) (b)

Figure 3–9: Downstream evolution of the non-dimensionalized width of the r.m.s. temperature profiles for two line source locations: $y_s/h = 1.0$ (a) and $y_s/h = 0.17$ (b). Experiments (■), DNSs (□) and Lavertu & Mydlarski (2005) (×).

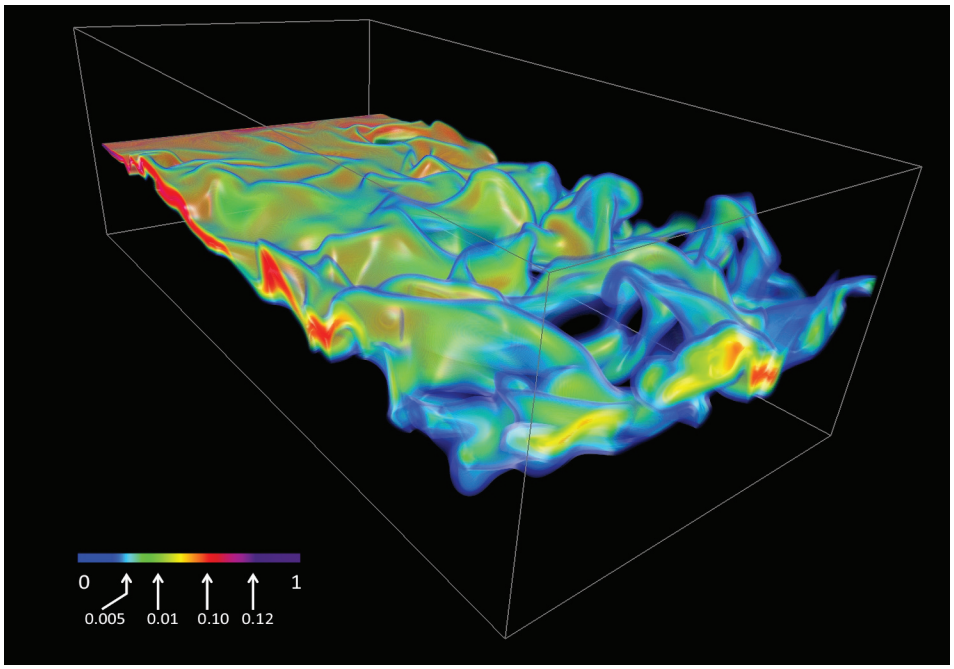

(a)

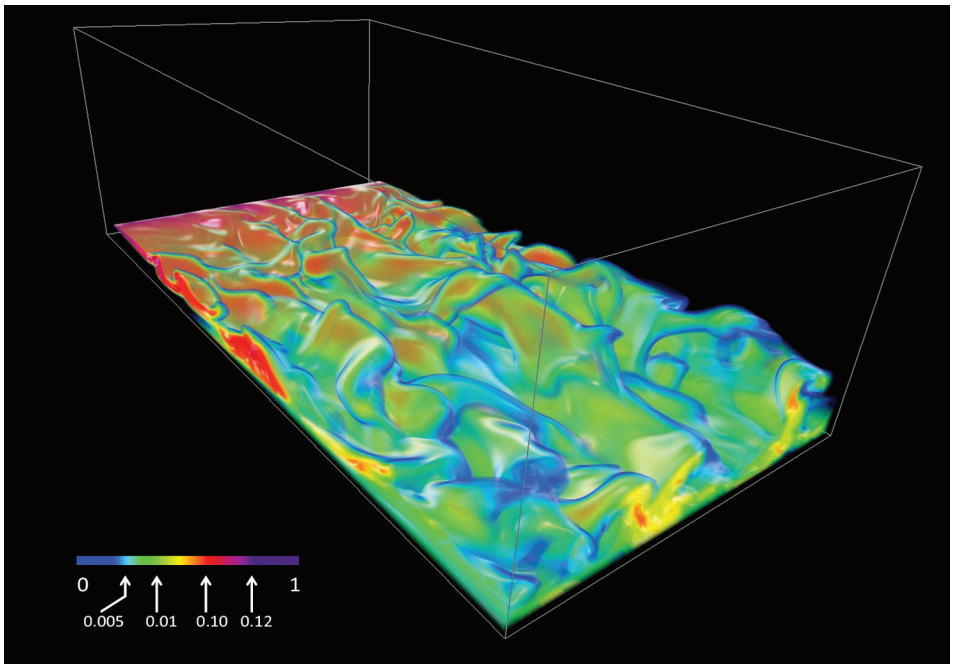

(b)

Figure 3–10: Instantaneous temperature fields generated (by DNS) downstream of line sources at two wall-normal locations: $y_s/h = 1.0$ (a) and $y_s/h = 0.17$ (b). $Re_\tau = 190$. $t^+ = 2770$ for the velocity field and $t^+ = 166$ for the scalar field (where, in the latter case, $t^+ = 0$ corresponds to the time at which the scalar is first injected into the flow). Note that the legend is non-linear in the non-dimensionalized temperature ($(T - T_\infty)/(T_{max} - T_\infty)$). Imagery produced by VAPOR (www.vapor.ucar.edu – see also Clyne & Rast (2005); Clyne *et al.* (2007))

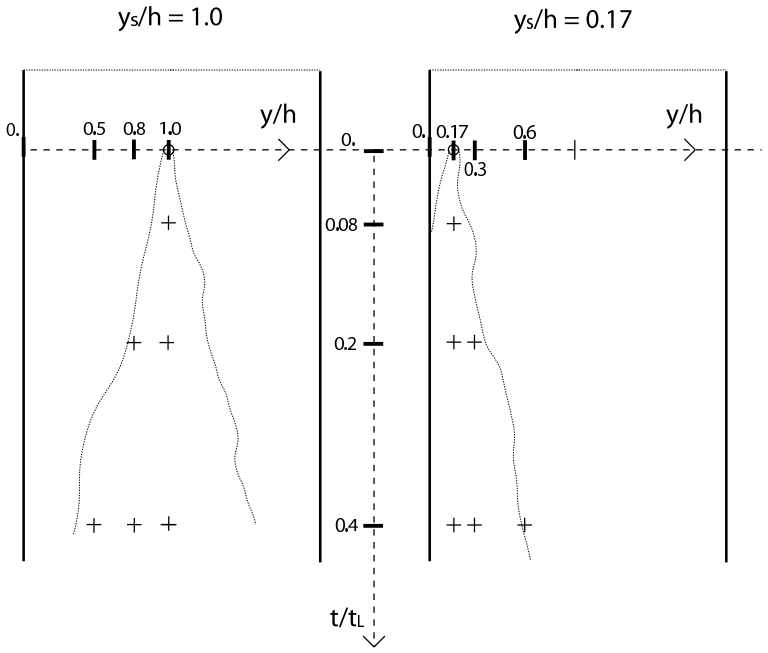

Figure 3–11: Schematic of the measurement locations within the thermal plume for the two line source locations ($y_s/h = 1.0$ and $y_s/h = 0.17$). The crosses indicate the location where the small-scale statistics, reported in this section, were measured.

any artificial differences associated with the (small) errors induced by the inevitable use of Taylor's hypothesis in the experiments.

To compare experiments and simulations, the abscissa and ordinates were normalized by small scale quantities, i.e. $\varepsilon^{-3/4}\nu^{5/4}\varepsilon_{\theta_x}$ and $\eta = (\nu^3/\varepsilon)^{0.25}$. Note that the dissipation rate of the turbulent kinetic energy, ε, was determined using the assumption of local isotropy, i.e., $\varepsilon = 15\nu \int_0^\infty \kappa_1^2 E_u(\kappa_1)\mathrm{d}\kappa_1$, where E_u is the power spectrum of the longitudinal velocity fluctuations. ε_{θ_x} was determined from its definition $(-\alpha/\langle U\rangle^2)\langle(\partial\theta/\partial t)^2\rangle$ and also invoking Taylor's hypothesis.

Figures 3–12 and 3–13 show very good agreement between the experimental and numerical results at large κ_1, independent of the line source location. However, some differences exist at small κ_1 for the spectra measured downstream of the centreline line source (see figure 3–12) due to the difference in

Reynolds numbers between the experimental and numerical flows. (Given that the normalization is based on small-scale quantities, one cannot expect spectra of the two flows at different Reynolds number to be the same at large scales.) Note that the turbulence intensity (and therefore local Reynolds number) is higher in the near-wall region and, hence, the mixing more effective (Lavertu & Mydlarski, 2005). As a consequence, the agreement between experimental and numerical results at small to medium κ_1 is better for the scalar field generated by the near-wall source (figure 3–13) than that for the centreline source (figure 3–12).

One-dimensional streamwise dissipation spectra, i.e. $\kappa_1^2 E_\theta(\kappa_1)$, for thermal fields originating from line sources located at $y_s/h = 1.0$ and $y_s/h = 0.17$ are plotted in figures 3–14 and 3–15, respectively. The experiments and DNSs are in good agreement at all measurement locations for both line source locations. Note that the normalization used in these figures implies that the area under each curve is equal to the Prandtl number ($Pr = 0.7$). As previously noted, these results serve to confirm that the resolution of our DNSs is sufficient to *i*) accurately resolve the contributions to ε_θ, and *ii*) reproduce the range of length scales measured in the experiments.

The dissipation spectra are generally found to peak at $\kappa_1\eta \approx 0.2$ showing that most of the dissipation occurs at length scales five times larger than η, consistent with the finding of Kozuka *et al.* (2009). However, figures 3–14 (a,c and f) show a slight drift of the peak locations with increasing downstream distance from larger to smaller κ_1 for the centreline source. (The peak occurs at $\kappa_1\eta = 0.26,\ 0.21$ and 0.17 for $t/t_L = 0.08,\ 0.2$ and 0.4, respectively.) Such a trend is not observed downstream of the near-wall sources. This may be attributed to the increased mixing that occurs near the wall (Lavertu & Mydlarski, 2005).

We proceed to analyze the components of the dissipation spectra by examining one-dimensional spectra of the temperature derivative $\partial\theta/\partial\beta$, where $\partial\theta/\partial\beta$ is the β-derivative of the scalar fluctuations ($\beta = x,\ y$ or z). To this end, figures 3–16 and 3–17 plot spectra of the streamwise (x), wall-normal (y) and spanwise (z) components of the fluctuating temperature gradient, i.e. $E_{\partial\theta/\partial\beta}$. $E_{\partial\theta/\partial x}$ was measured by assuming Taylor's hypothesis, whereas the other two were measured using a second-order finite difference approximation. Note that the streamwise (one-dimensional) spectrum tends towards zero at large scales, which differs from the two other spectra that are subject to aliasing and have a finite value at zero wavenumber (Van Atta, 1991). This difference is therefore *not* dynamical and thus not indicative of a lack of local isotropy. Note that the spectra were normalized by $\varepsilon_\theta\eta/\nu$, where $\varepsilon_\theta = \varepsilon_{\theta_x} + \varepsilon_{\theta_y} + \varepsilon_{\theta_z}$ and where η was computed using the assumption of local isotropy.

The present spectra are similar to those reported by Van Atta (1991) and Thoroddsen & Van Atta (1996), who studied scalar dissipation in decaying stably stratified grid turbulence. The authors showed that the large and small scales are anisotropic near the grid but become strongly anisotropic farther downstream in their stratified flow. Interestingly, they noticed that all scales develop anisotropies at about the same rate.

In the present research, the scalar is injected in a highly anisotropic manner that produces sharp gradients in the y-direction in the vicinity of the source. This anisotropy is shown in both figures 3–16(a) and 3–17(a) where $\varepsilon_{\theta_y} > \varepsilon_{\theta_z}$. However, the gap between ε_{θ_y} and ε_{θ_z} diminishes considerably with increasing downstream distance. Ultimately, the experimentally measured spectra of ε_{θ_y} and ε_{θ_z} at $t/t_L = 0.4$ (figure 3–16(d)) are almost indistinguishable, which shows a clear tendency of the scalar dissipation rate towards isotropy. It is also interesting to note that the collapse between the spectra of

ε_{θ_y} and ε_{θ_z} appears even sooner when the source is in the near-wall region (i.e. $t/t_L = 0.2$ as shown in 3–17(b)). This can again be attributed to the higher turbulence intensity (and therefore better mixing) that occurs in the near-wall region.

Figures 3–16 and 3–17 exhibit good agreement between the experiments and DNSs at large wavenumbers, especially for the centreline line source. Furthermore, a similar good agreement is also reported at small wavenumbers when the line source is located at the centreline, which reinforces the validity of the results presented herein. However, discrepancies exist at small wavenumbers when the line source is in the near-wall region. The numerical results exhibit a persistent anisotropy between ε_{θ_y} and ε_{θ_z} when $y_s/h = 0.17$. These discrepancies are related to the production of ε_θ by mean velocity gradients, which occurs away from the centreline, near the wall. This effect will be discussed in more detail further on in this section. The reader is also referred to Gonzalez (2000), which describes the effects of mean velocity and temperature gradients on the isotropy of ε_θ in detail.

3.7.3.2 PDFs of $\partial\theta/\partial x_\beta$

The PDFs of the temperature derivatives are plotted in figures 3–18 and 3–19 for line sources located at $y_s/h = 1.0$ and 0.17, respectively. There is good agreement between the experiments and DNSs. The PDFs of the three components are quite different from each other near the source and become similar at the farthest downstream distance, where they develop quasi-exponential tails. Close to the source, figure 3–18(a) shows three peaks in the simulated PDF of the wall-normal temperature derivative, $P(\partial\theta/\partial y)$, whereas the PDFs of the other two derivatives are unimodal. These triple peaks are due to the nature of the temperature field immediately downstream of the source. For very small t/t_L, the plume is a top-hat profile and thus we expect the

PDF to be given by two delta functions where the two peaks are nominally at $\pm\left(T_{wire}-T_{\infty}\right)/(d_s/2)$, where d_s is the source diameter. However, slightly farther away from the source, after some mixing has occurred, the principal peak (or mode) starts to emerge while the other two initial peaks recede. Even farther away from the source, the peaks from the initial top-hat profile disappear and the PDF develops exponential tails, in this case, characteristic of a well-mixed scalar. In the near-wall region, the mixing being better, the initial peaks disappear very quickly and the initial trimodal PDF is not observed for the measurement locations considered herein. For a similar reason, the experimentally measured $P(\partial\theta/\partial y)$ (being at a higher Reynolds number) is also unimodal although of a shape that would be consistent with a trimodal PDF farther upstream. In addition, it is worth noting that the quasi-exponential tails appear sooner for the near-wall line source than when the line source is at the centreline.

3.7.3.3 The evolution of ε_θ

The instantaneous fields of the (total and three components of the) scalar dissipation rate (i.e., ε_θ, ε_{θ_x}, ε_{θ_y} and ε_{θ_z}), are plotted in figure 3–20. These are presented to provide qualitative insight into the scalar dissipation rate. In the analysis that follows, we quantitatively discuss the evolution of ε_θ and its components by analyzing specific statistics related to these quantities. For example, it is already evident from figure 3–20 that the largest contribution to ε_θ comes from ε_{θ_y}. However, one can also observe that its relative contribution to ε_θ decreases with increasing downstream distance, as will be elaborated upon below. We encourage the reader to refer back to these plots for further insight in the course of the subsequent discussion.

Wall-normal profiles of the three components of the scalar dissipation rate are reported in figure 3–21 for four downstream locations within the range

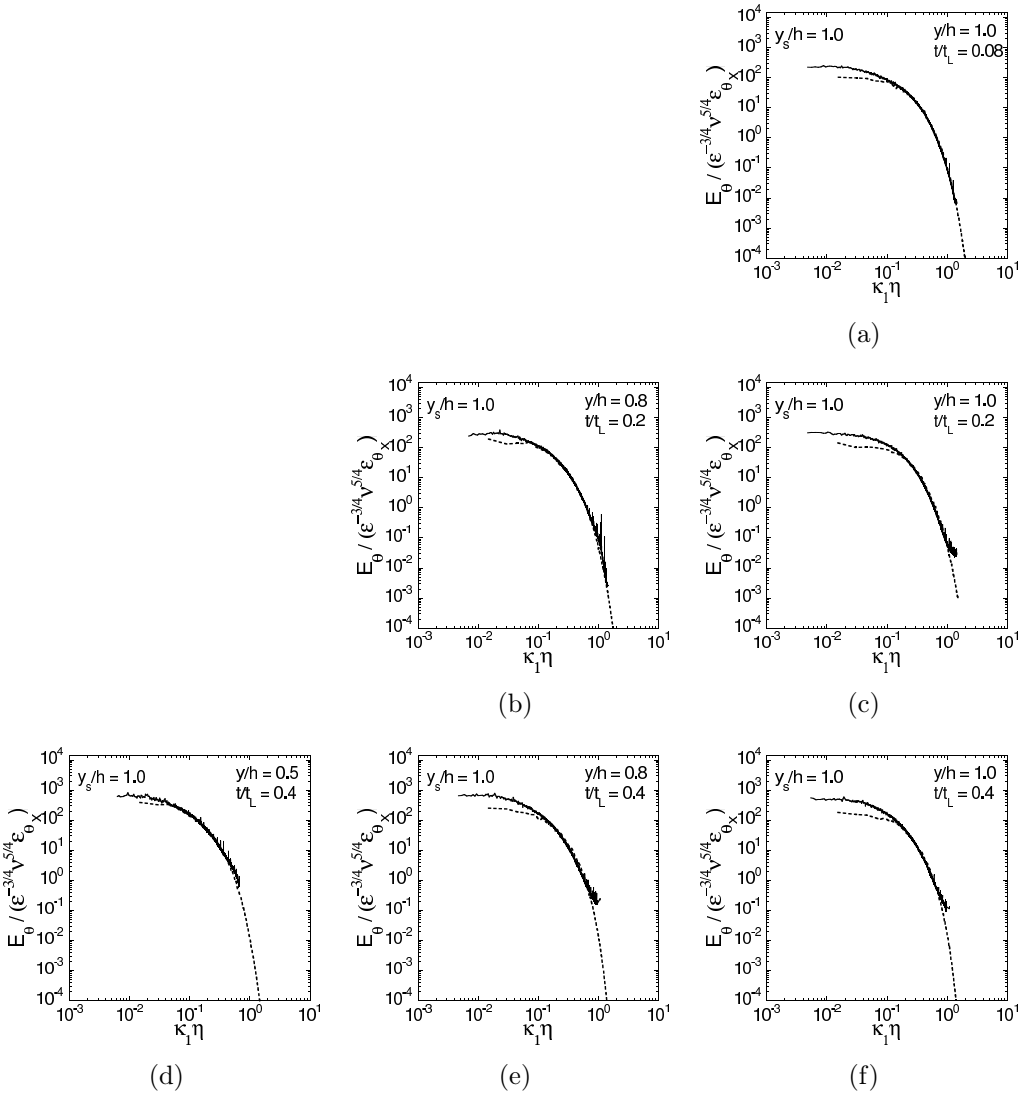

Figure 3–12: One-dimensional longitudinal spectra of the temperature fluctuations for $y_s/h = 1.0$ at three downstream locations: $t/t_L = 0.08$ (a), $t/t_L = 0.2$ (b,c) and $t/t_L = 0.4$ (d-f) and at three wall-normal locations: $y/h = 1.0$ (a,c,f), $y/h = 0.8$ (b,e) and $y/h = 0.5$ (d). Results from experiments (solid line) and DNSs (dashed line) are reported.

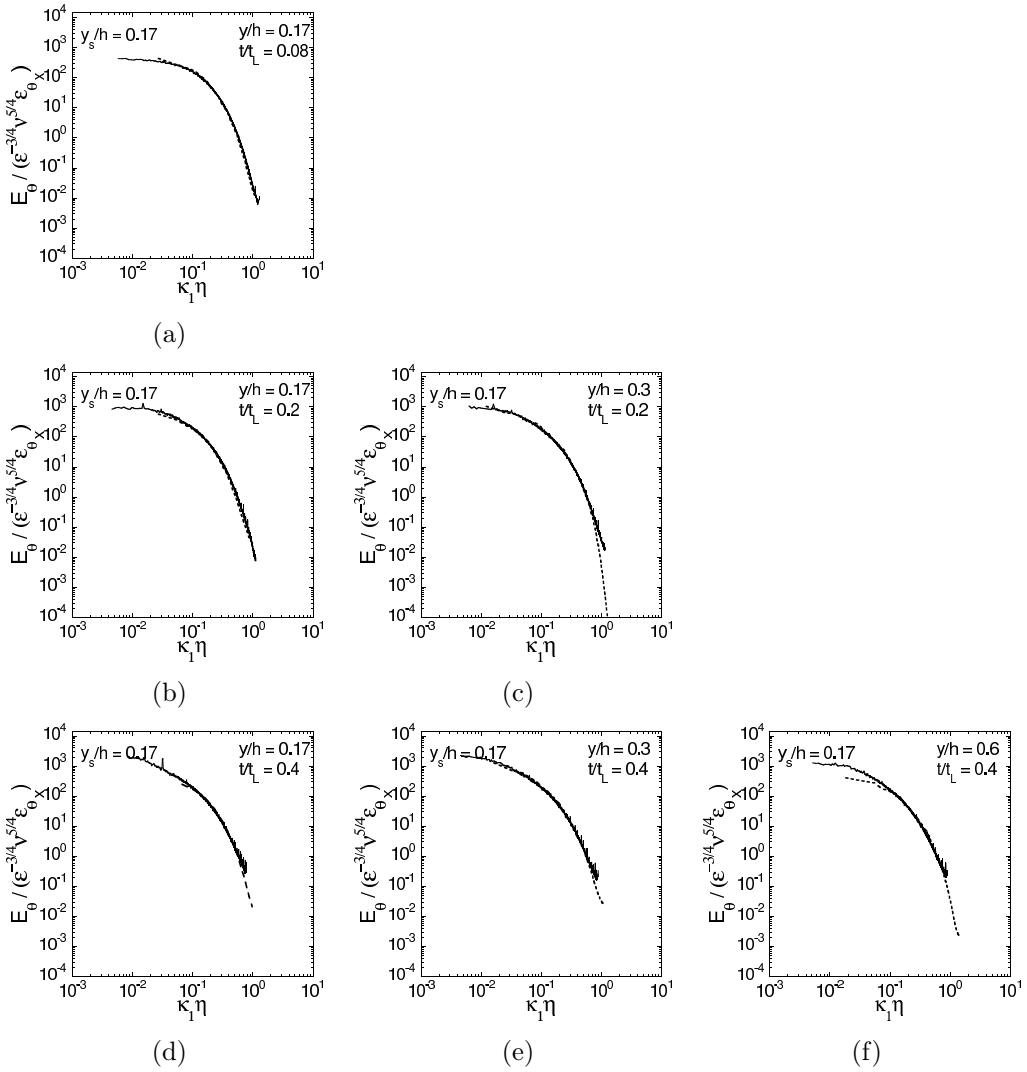

Figure 3–13: One-dimensional longitudinal spectra of the temperature fluctuations for $y_s/h = 0.17$ at three downstream locations: $t/t_L = 0.08$ (a), $t/t_L = 0.2$ (b,c) and $t/t_L = 0.4$ (d-f) and at three wall-normal locations: $y/h = 0.17$ (a,b,d), $y/h = 0.3$ (c,e) and $y/h = 0.6$ (f). Results from experiments (solid line) and DNSs (dashed line) are reported.

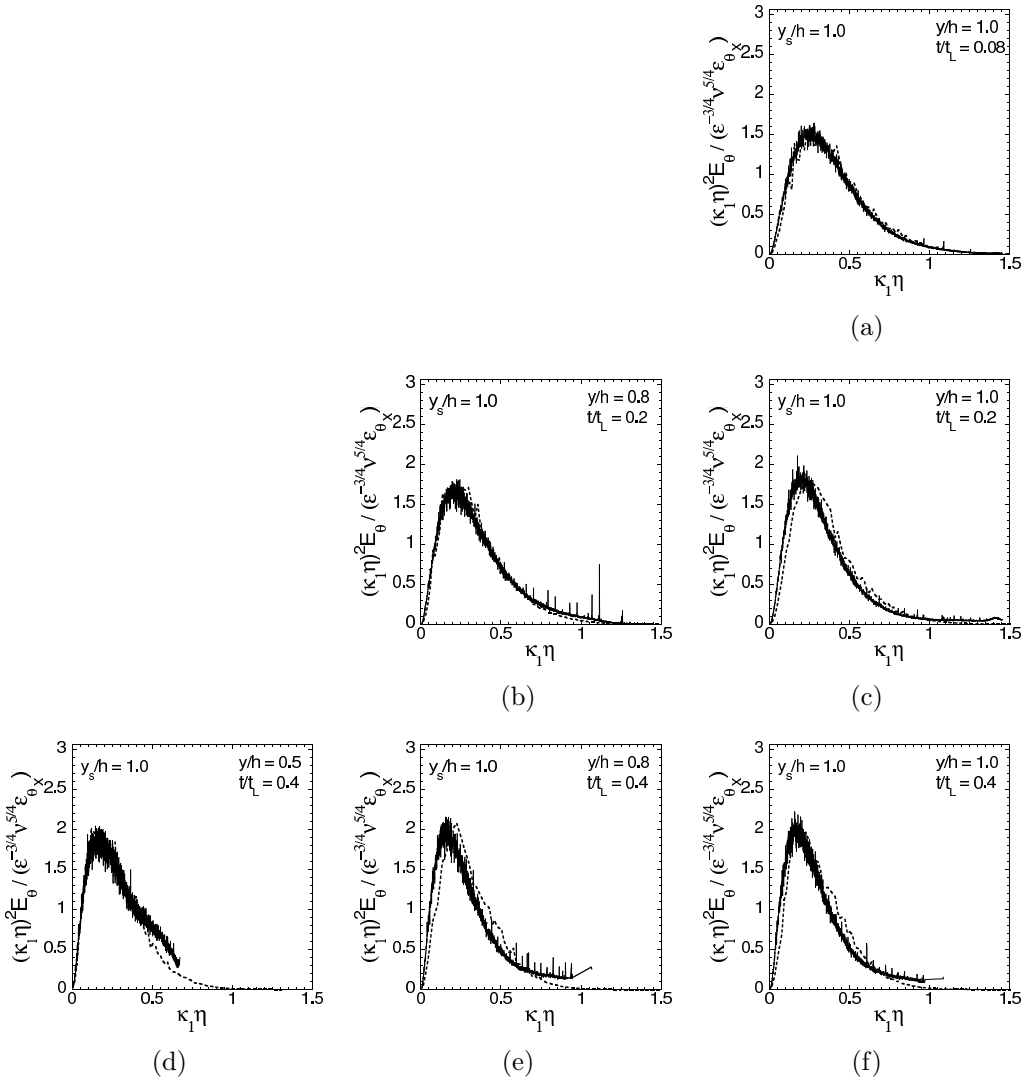

Figure 3–14: One-dimensional longitudinal dissipation spectra of the temperature fluctuations for $y_s/h = 1.0$ at three downstream locations: $t/t_L = 0.08$ (a), $t/t_L = 0.2$ (b,c) and $t/t_L = 0.4$ (d-f) and at three wall-normal locations: $y/h = 1.0$ (a,c,f), $y/h = 0.8$ (b,e) and $y/h = 0.5$ (d). Results from experiments (solid line) and DNSs (dashed line) are reported.

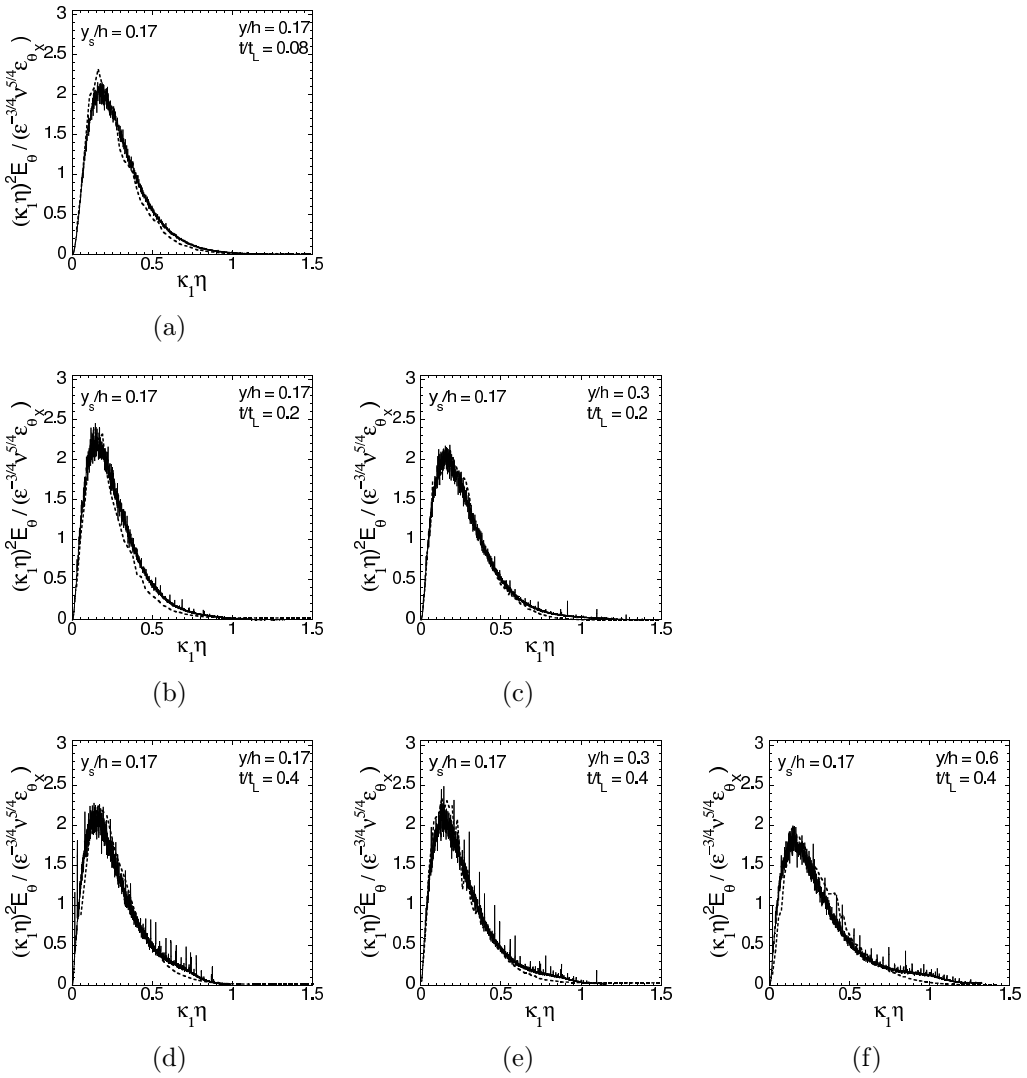

Figure 3–15: One-dimensional longitudinal dissipation spectra of the temperature fluctuations for $y_s/h = 0.17$ at three downstream locations: $t/t_L = 0.08$ (a), $t/t_L = 0.2$ (b,c) and $t/t_L = 0.4$ (d-f) and at three wall-normal locations: $y/h = 0.17$ (a,b,d), $y/h = 0.3$ (c,e) and $y/h = 0.6$ (f). Results from experiments (solid line) and DNSs (dashed line) are reported.

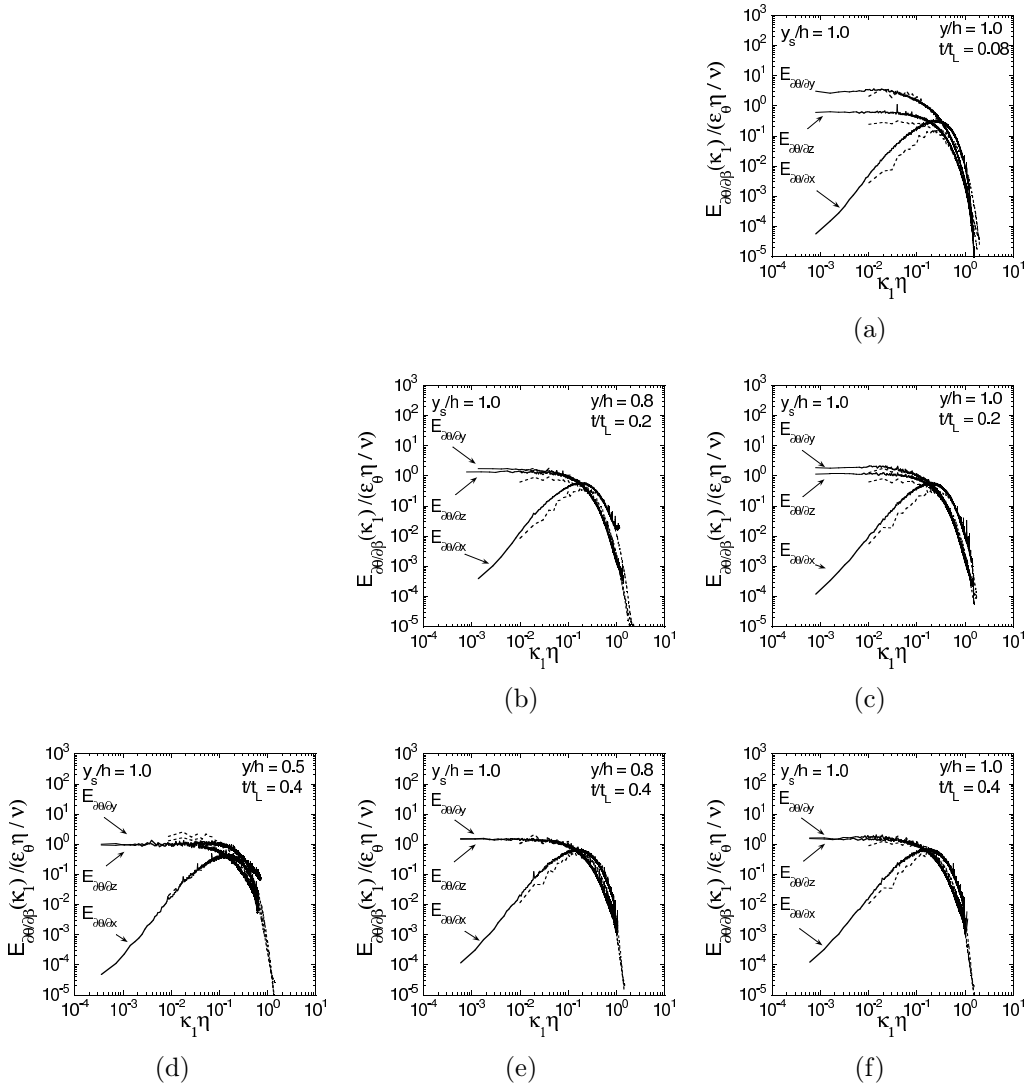

Figure 3–16: One-dimensional spectra of the temperature derivatives ($\partial\theta/\partial\beta$ where $\beta = x, y$ or z) for $y_s/h = 1.0$ at three downstream locations: $t/t_L = 0.08$ (a), $t/t_L = 0.20$ (b,c) and $t/t_L = 0.40$ (d-f), and at three wall-normal locations: $y/h = 1.0$ (a,c,f), $y/h = 0.8$ (b,e) and $y/h = 0.5$ (d). Results from experiments (solid line) and DNSs (dashed line) are reported.

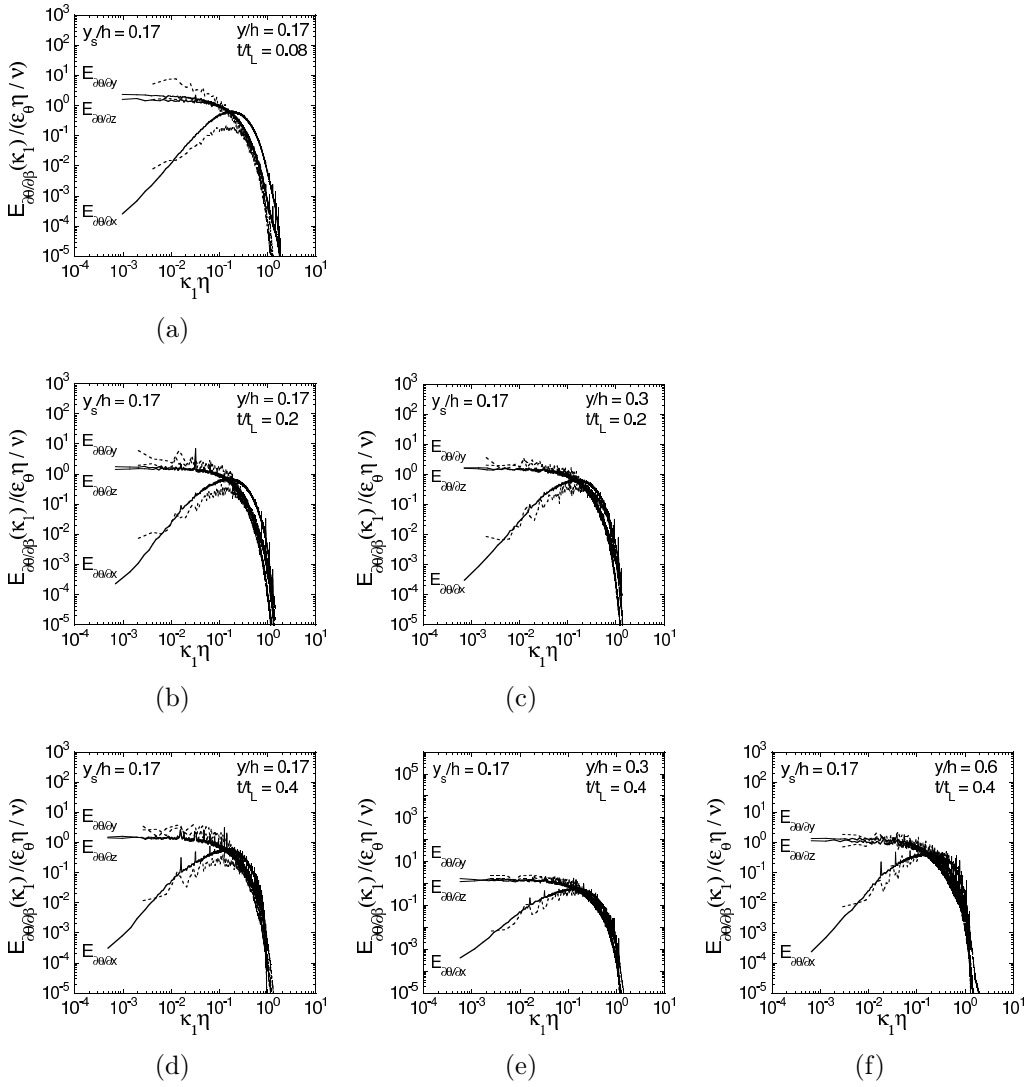

Figure 3–17: One-dimensional spectra of the temperature derivatives ($\partial\theta/\partial\beta$ where $\beta = x, y$ or z) for $y_s/h = 0.17$ at three downstream locations: $t/t_L = 0.08$ (a), $t/t_L = 0.20$ (b,c) and $t/t_L = 0.40$ (d-f), and at three wall-normal locations: $y/h = 0.17$ (a,b,d), $y/h = 0.3$ (c,e) and $y/h = 0.6$ (f). Results from experiments (solid line) and DNSs (dashed line) are reported.

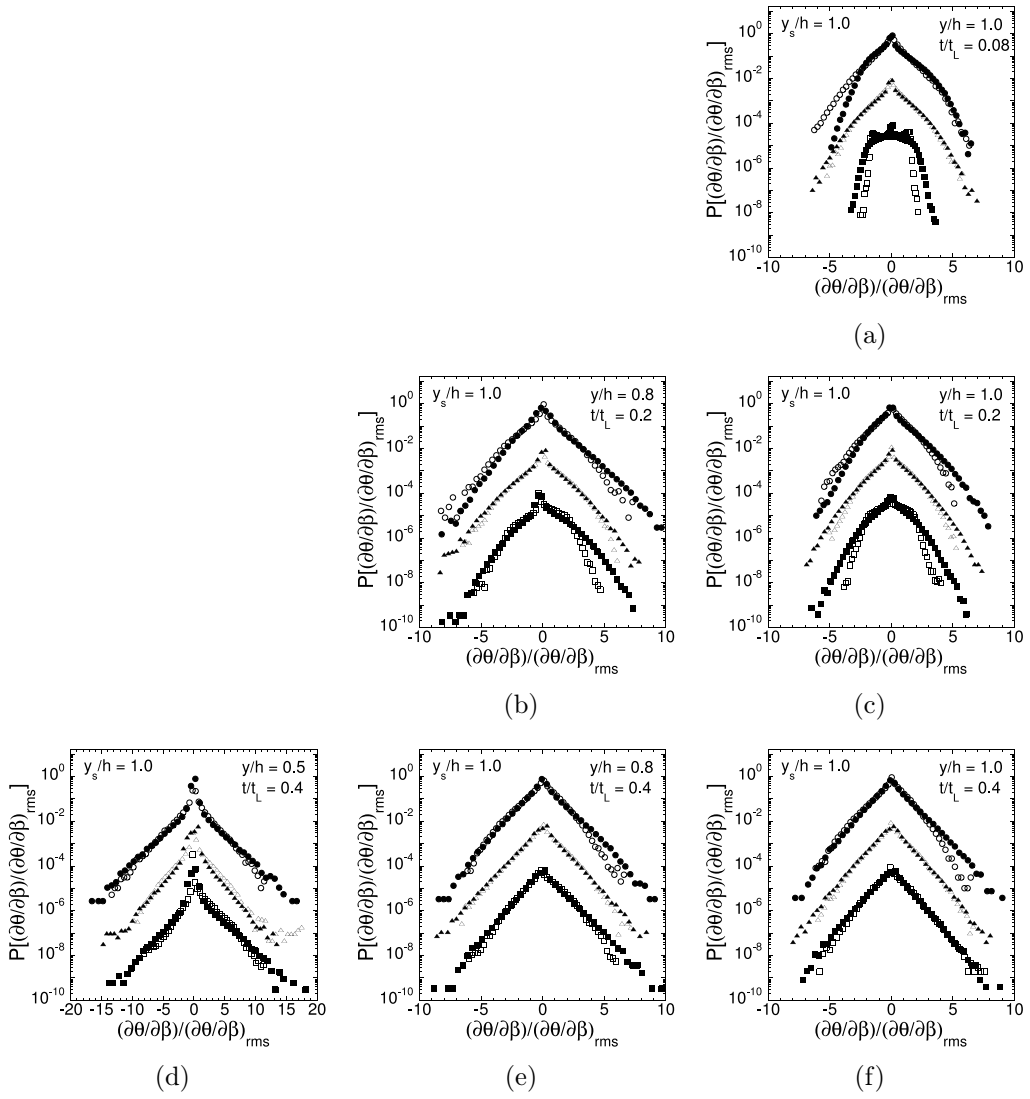

Figure 3–18: PDFs of the temperature derivatives ($\partial\theta/\partial\beta$ where $\beta = x, y$ or z) for $y_s/h = 1.0$ at three downstream locations: $t/t_L = 0.08$ (a), $t/t_L = 0.20$ (b,c) and $t/t_L = 0.40$ (d-f) and at three wall-normal locations: $y/h = 1.0$ (a,c,f), $y/h = 0.8$ (b,e) and $y/h = 0.5$ (d). Experimental and DNS results are respectively denoted by the solid symbols ($\partial\theta/\partial x$ (•), $\partial\theta/\partial y$ (■) and $\partial\theta/\partial z$ (▲)) and by the open symbols ($\partial\theta/\partial x$ (○), $\partial\theta/\partial y$ (□) and $\partial\theta/\partial z$ (△)). The curve for $\mathrm{P}[(\partial\theta/\partial x)/(\partial\theta/\partial x)_{rms}]$ is plotted normally, whereas remaining curves are offset downwards in increments of two decades.

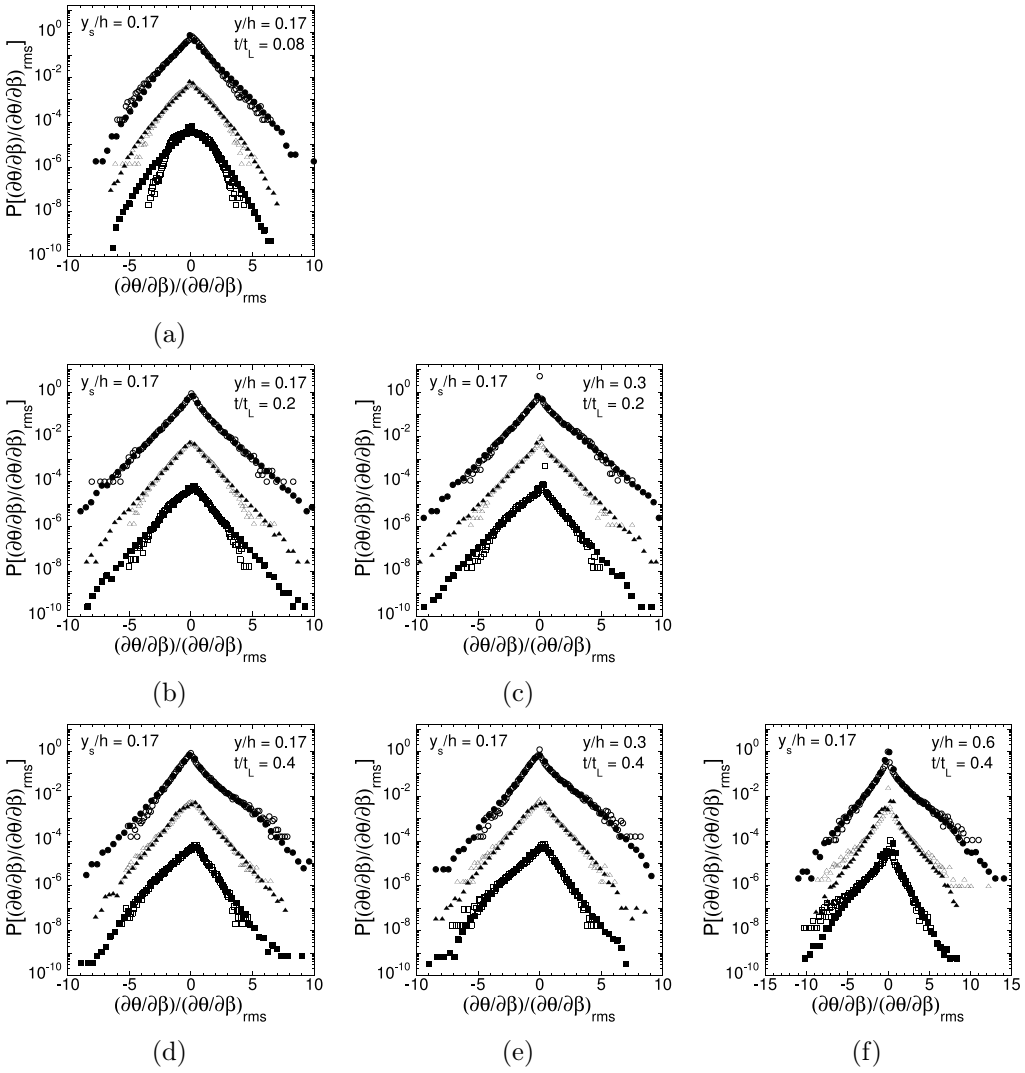

Figure 3–19: PDFs of the temperature derivatives ($\partial\theta/\partial\beta$ where $\beta = x, y$ or z) for $y_s/h = 0.17$ at three downstream locations: $t/t_L = 0.08$ (a), $t/t_L = 0.2$ (b,c) and $t/t_L = 0.40$ (d-f) for three wall-normal locations: $y/h = 0.17$ (a,b,d), $y/h = 0.3$ (c,e) and $y/h = 0.6$ (f). Experimental and DNSs results are respectively denoted by the solid symbols ($\partial\theta/\partial x$ (●), $\partial\theta/\partial y$ (■) and $\partial\theta/\partial z$ (▲)) and by the open symbols ($\partial\theta/\partial x$ (○), $\partial\theta/\partial y$ (□) and $\partial\theta/\partial z$ (△)). The curve for $\mathrm{P}[(\partial\theta/\partial x)/(\partial\theta/\partial x)_{rms}]$ is plotted normally, whereas remaining curves are offset downwards in increments of two decades.

$t/t_L = 0.08 - 0.6$. The scalar dissipation rate shown for both line source locations has been scaled by $t_L/\langle \Delta T \rangle_{ref}^2$.

For $y_s/h = 1.0$, figure 3–21 shows good agreement between the experiments and the DNSs. The three components of the scalar dissipation rate have approximately Gaussian profiles with maxima at the channel centreline. Outside the plume, a plateau is observed in the experimental data due to the non-zero ambient thermal noise. Small-scale anisotropy is observed near the source ($t/t_L = 0.08$) where $\varepsilon_{\theta_y} > \varepsilon_{\theta_z} \approx \varepsilon_{\theta_x}$. Farther downstream ($t/t_L = 0.4$), the gap between the three components of ε_θ is considerably reduced.

For $y_s/h = 0.17$, figure 3–21 shows differences between the experiments and the DNSs for the near-wall data. Firstly, the experimental data appear to be more isotropic, presumably due to their larger Reynolds number, whereas the DNSs exhibit differences between the three components ($\varepsilon_{\theta_y} > \varepsilon_{\theta_z} > \varepsilon_{\theta_x}$). Furthermore, the peak of ε_{θ_y} (the largest component) measured from the DNSs remains downstream of the source location for all measurement locations presented herein, whereas the peak of ε_{θ_y} measured in the experiments drifts towards the channel centreline. This may be explained by the prominence in the DNSs of the mechanism of production of ε_{θ_y} due to mean velocity gradients (which, as previously mentioned, will be discussed shortly). The movement in the peak of the scalar dissipation profile recalls the drift observed in the r.m.s. profiles. Note that in both the experiments and the DNSs, the peaks of the ε_{θ_x} and ε_{θ_z} profiles drift towards the centreline as t/t_L is increased (but the rate at which they do so is faster for the experiments). ε_{θ_y} also remains the largest component. Note that if the scalar were injected uniformly, one might expect that the scalar dissipation would peak near the region of maximum shear. (Recall that in a turbulent channel flow, the turbulence intensity is maximum in the buffer layer, i.e. $y^+ \in [5, 30]$. In the present flows, $y^+ = 15$

corresponds to $y/h = 0.03$ and $y/h = 0.08$ in the experiments and the DNSs, respectively.)

The evolution of the peak of the dissipation profile is somewhat similar to the evolution of the peak of the r.m.s. profile (see figure 3–5(b)). Previous researchers have attempted to establish a parallel between the location of the maximum of dissipation and that of the maximum temperature fluctuations. For instance, Lockwood & Moneib (1980) measured the fluctuating temperature in a heated round turbulent free jet. They showed that the scalar dissipation rate of a turbulent jet attains its maximum at the location of the maximum of the temperature fluctuation intensity. However, this conclusion was contradicted by the observations of Antonia & Mi (1993), who studied the temperature "jumps" (a relatively sudden increase in temperature followed by a gradual decrease – also known as "ramp-cliff" structures) in a heated turbulent jet, and who attempted to estimate their contributions to the temperature dissipation. They showed that although the temperature "jumps" contributed to an increase in the temperature variance, their contribution to the scalar dissipation rate was small.

The downstream evolution of the centreline ($y/h = 1.0$) and the off-centreline ($y/h = 0.8$) mean thermal dissipation is shown in figure 3–22 for $y_s/h = 1.0$. Excellent agreement between the experiments and the DNSs are shown. At the centreline, the experiments and DNS both exhibit a power law-decay of the form $\varepsilon_\theta \sim (t/t_L)^n$, where n varied between -2.2 and -2.0, with the experiments tending to exhibit slightly more rapid decay exponents. Away from the centreline, a power-law decay is also observed, but only after a certain distance downstream ($t/t_L \gtrsim 0.2$), which approximately corresponds to the point at which the plume is wide enough so that the sensor (located at $y/h = 0.8$) no longer measures outside of the plume as it flaps. Analogous

plots for the near-wall source are also given in figure 3–23. As for $y_s/h = 1.0$, the dissipation is maximum in the vicinity of the source and exhibits a power law-decay with similar values of decay exponents, with the experiments again tending to exhibit a slightly more rapid decay. Given the larger values of ε_θ measured in the central region of the plume, one can furthermore conclude that the efficiency in smearing the fluctuations in the scalar field is larger behind the source than at the edges of the plume. However, at the farthest downstream location, the difference between the two is smaller than 8%, indicating that ε_θ tends to become more uniform inside the plume as it expands, as observed in figure 3–21. We also note that Rosset *et al.* (2001) found $\varepsilon_\theta \sim x^{-2.5}$ downstream of a heated line source placed in a turbulent boundary layer. Their decay exponent, albeit slightly more negative, is quite similar to the values measured herein, despite the differences in flow geometry, Reynolds number, line source location, etc.

The components of ε_θ are investigated in figure 3–24 and 3–25 when $y_s/h = 1.0$ and 0.17, respectively, where the downstream evolutions of the three components, ε_{θ_x}, ε_{θ_y} and ε_{θ_z}, are plotted. When the line source is at the centreline, both the experiments and the DNSs converge towards an isotropic state. Near the source, however, the dissipation is predominantly in the y-direction due to the sharp temperature gradients ($\partial\theta/\partial y$) there that are associated with the plume boundary. The dissipation in the two other directions ($\partial\theta/\partial x$ and $\partial\theta/\partial z$) are almost equal, indicative of the quasi-axisymmetric nature of the turbulence at that location. For the near-wall source, the agreement between the experiments and the DNSs is not as good as it is for the centreline source. (Differences in the Reynolds numbers of the two flows may be more significant in the near-wall region.) The experiments are found to be almost isotropic, whereas the DNS results exhibit persistent anisotropy.

To further investigate the anisotropy, we calculated the following ratios: $\varepsilon_\theta/\varepsilon_{\theta_\beta}$ (figures 3–26 and 3–27) and $\varepsilon_{\theta_\beta}/\varepsilon_{\theta_\gamma}$ (figures 3–28 and 3–29), where the indices β and γ can be x, y or z, and where $\beta \neq \gamma$. For an isotropic flow, these ratios must be equal to 3 and 1, respectively. Figures 3–26 and 3–28 confirm that the small-scale anisotropy is reduced with the downstream distance for the centreline source. Furthermore, figure 3–28 most clearly shows that the anisotropy in ε_θ comes from ε_{θ_y} (which is equally offset/balanced by the anisotropies in ε_{θ_x} and ε_{θ_z}). For $y_s/h = 0.17$, figures 3–27 and 3–29 show that the anisotropy decays until $t/t_L = 0.2$ and then remains constant (and anisotropic). Furthermore, note that the anisotropy is stronger when measured at $y/h = 0.17$ than at $y/h = 0.3$, indicating that there exists regions in the channel flow field that better lend themselves to returning to an isotropic state. We will subsequently argue that the anisotropy is dependent on the presence of velocity gradients (Antonia & Browne, 1986; Gonzalez, 2000), as well as the Reynolds number of the flow. In this vein, we remark that the anisotropy measured in the experiments is less strong than in the DNSs, presumably due to its larger Reynolds numbers, which i) results from a more rapid elimination of the large-scale anisotropy associated with the injection of the scalar, and ii) explains the discrepancies observed in figure 3–25. Moreover, note that the flow is no longer (quasi-)homogeneous in the regions plotted in figures 3–27 and 3–29, so the equal offset of the anisotropy of ε_{θ_y} by ε_{θ_x} and ε_{θ_z} is not observed here (like in figures 3–26 and 3–28). Regarding these figures, we finally note that the measured increase in anisotropy observed in figures 3–26(b), 3–27, 3–28(b) and 3–29 is presumably due to experimental errors arising from the low signal-noise ratio at the farthest downstream location ($t/t_L = 0.6$).

To investigate and explain the aforementioned anisotropy, consider the evolution equation of the scalar dissipation rate, given by

$$\frac{\partial \varepsilon_\theta}{\partial t} + \langle U_j \rangle \frac{\partial \varepsilon_\theta}{\partial x_j} = \overbrace{-2\alpha \frac{\partial \langle U_j \rangle}{\partial x_i} \langle \frac{\partial \theta}{\partial x_i} \frac{\partial \theta}{\partial x_j} \rangle}^{\mathcal{P}} - 2\alpha \frac{\partial \langle T \rangle}{\partial x_j} \langle \frac{\partial u_j}{\partial x_i} \frac{\partial \theta}{\partial x_i} \rangle$$
$$- 2\alpha \langle u_j \frac{\partial \theta}{\partial x_i} \rangle \frac{\partial^2 \langle T \rangle}{\partial x_i^2} x_j - 2\alpha \langle \frac{\partial u_j}{\partial x_i} \frac{\partial \theta}{\partial x_i} \frac{\partial \theta}{\partial x_j} \rangle$$
$$+ \frac{\partial}{\partial x_j} \left(\alpha \frac{\partial \langle \varepsilon_\theta \rangle}{\partial x_j} - \langle u_j \varepsilon_\theta \rangle \right) - \underbrace{2\alpha^2 \langle \frac{\partial^2 \theta}{\partial x_i^2} x_j \frac{\partial^2 \theta}{\partial x_i^2} x_j \rangle}_{\Gamma}, \qquad (3.3)$$

(where repeated indices imply Einstein's summation convention) and focus on the two terms $\mathcal{P}(= \mathcal{P}_x + \mathcal{P}_y + \mathcal{P}_z)$ and $\Gamma(= \Gamma_x + \Gamma_y + \Gamma_z)$. The former is the production of ε_θ by mean velocity gradients, and the latter quantifies the dissipation of ε_θ by molecular processes. For channel flow, the components of these two terms are: $\mathcal{P} = \mathcal{P}_y = -2\alpha \partial \langle U \rangle / \partial y \langle (\partial \theta / \partial y)(\partial \theta / \partial x) \rangle$ with $\mathcal{P}_x = \mathcal{P}_z = 0$ and $\Gamma_x = 2\alpha^2 [\langle (\partial^2 \theta / \partial x^2)^2 \rangle + \langle (\partial^2 \theta / \partial x \partial y)^2 \rangle + \langle (\partial^2 \theta / \partial x \partial z)^2 \rangle]$, $\Gamma_y = 2\alpha^2 [\langle (\partial^2 \theta / \partial y \partial x)^2 \rangle + \langle (\partial^2 \theta / \partial y^2)^2 \rangle + \langle (\partial^2 \theta / \partial y \partial z)^2 \rangle]$ and $\Gamma_z = 2\alpha^2 [\langle (\partial^2 \theta / \partial z \partial x)^2 \rangle + \langle (\partial^2 \theta / \partial z \partial y)^2 \rangle + \langle (\partial^2 \theta / \partial z^2)^2 \rangle]$. Figure 3–30 shows the wall-normal profile of the three components of Γ and $\mathcal{P}_y$, for the two source locations ($y_s/h = 1.0$ and 0.17) at three downstream positions ($t/t_L = 0.08,\ 0.2$ and 0.4). Both experiments and DNSs are reported on the figures. Note that the y- and z-components of Γ were not accessible experimentally as $\partial\theta/\partial y$ and $\partial\theta/\partial z$ were not simultaneously measured.

The mean velocity gradient that exists in the wall-normal direction only, contributes to the production of ε_θ (in the y-direction). The relative importance of this production depends on the wall-normal location within the channel. As the mean velocity gradient ($\partial \langle U \rangle / \partial y$) is small in the centre of the channel, there is very little production of the scalar dissipation by the mean velocity field in the central region (and none at the channel mid-plane, by

symmetry). On the other hand, the contribution of $\mathcal{P}_y$ to ε_{θ_y} is not negligible in the near-wall region, as the velocity gradients are large there. In fact, figure 3–30 shows that the production of dissipation in the wall-normal direction is of the same order of magnitude as Γ_y near the walls. The figure also shows that $\mathcal{P}_y$ does not contribute to the evolution of ε_{θ_y} (or ε_θ) when the source is at the centreline, as expected. Lastly, this production of ε_θ due to mean velocity gradients now explains the aforementioned *i*) persistent anisotropies for the near-wall scalar fields (figures 3–27 and 3–29), and *ii*) the persistence of a maximum in ε_{θ_y} near the wall (figure 3–21).

Johansson & Wikström (1999) performed DNSs of turbulent channel flow with an imposed mean scalar gradient. In the near-wall region, they showed that the two mean gradient production terms (i.e. the first and second terms on the right hand side of equation (3.3)) as well as the term that is the scalar-field analogue to the vortex-stretching term in the turbulent enstrophy budget (i.e. the fourth term in the right hand side of equation (3.3)) contribute the most to the production of ε_θ. These results agree with those presented herein. (Note that combined statistical moments of both the velocity and temperature derivatives are not computed due to the fact that the velocity and temperature field are not calculated nor measured simultaneously in the present approach.)

Anisotropy invariant maps for ε_θ (Antonia & Kim, 1994) are plotted in figures 3–31-3–33 where the three solid lines are (often referred to as) the Lumley triangle (Lumley, 1978). This triangle is delimited by the following

three curves (in the (III,$-II$) plane):

$$III = -\frac{II}{3} - \frac{1}{27}, \tag{3.4}$$

$$III = -2\left(\frac{II}{3}\right)^{3/2}, \tag{3.5}$$

$$III = 2\left(\frac{II}{3}\right)^{3/2}. \tag{3.6}$$

II and III are the second and third invariants of the scalar dissipation rate anisotropy tensor defined as:

$$t_{ij} = \alpha\frac{\langle\theta_{,x_i}\theta_{,x_j}\rangle}{\langle\varepsilon_\theta\rangle} - \frac{1}{3}\delta_{ij}, \tag{3.7}$$

where δ_{ij} is the Kronecker delta. The second and third invariants are given by:

$$II = -\frac{1}{2}t_{ij}t_{ji}, \tag{3.8}$$

$$III = \frac{1}{3}t_{ij}t_{jk}t_{ki}. \tag{3.9}$$

The plot of $-II$ versus III represents all the possible states that characterize the tensor t_{ij}. Curves (3.5) and (3.6) are respectively the right and left "axisymmetric" boundaries of the anisotropic invariant map. The vertex $II = III = 0$ characterizes the isotropic state. The top right vertex of the line given by equation (3.4) represents the one-component state and the bottom left vertex represents the two-component state.

The return to isotropy behind a centreline source (figure 3–31(a)) is *i*) clearly axisymmetric, consistent with the previous results of figure 3–28, and *ii*) more rapid than that of the scalar field behind the near-wall source. The axisymmetry of the scalar field behind the centreline line source is more clearly observed in figure 3–32, which shows a very large level of axisymmetry at $y/h = 1.0$, but a slightly smaller degree of axisymmetry at $y/h = 0.8$. These results

should be contrasted with those of figure 3–33, which depict the anisotropy invariant maps for different wall-normal locations for the scalar field generated by the near-wall source. Of particular interest is the evolution from a one-dimensional state very close to the wall (Antonia & Kim, 1994) in figure 3–33(c) to an almost axisymmetric state farther away from the wall in figure 3–33(d).

3.7.3.4 Conditional statistics

To gain further insight into the dependence of the scalar fluctuations, θ, on their dissipation, ε_θ, which is of particular use in PDF models of scalar mixing, we examine the expectation of $\varepsilon_{\theta_\beta}$ conditioned on individual values of θ, i.e. $\left\langle \varepsilon_{\theta_\beta} | \theta \right\rangle$, where $\varepsilon_{\theta_\beta}$ is the β-component of the scalar dissipation ($\beta = x,\ y$ or z). Theoretical work has shown that the form of the conditional expectation profiles, $\langle \varepsilon_\theta | \theta \rangle$, depends on the PDF of the scalar fluctuation, θ (Pope & Ching, 1993). A Gaussian PDF of θ is associated with ε_θ and θ being independent. In this case, $\langle \varepsilon_\theta | \theta \rangle$ is found to be a constant (e.g. Anselmet *et al.*, 1994, figure 9*b*). A super-Gaussian PDF of the scalar is associated with a rounded, concave-up V-shape for the profile (Sinai & Yakhot, 1989; Jayesh & Warhaft, 1992) whereas a sub-Gaussian PDF is associated with a rounded concave-down V-shape for the profile (Mydlarski, 2003).

Figure 3–34 plots the expected value of the various components of the scalar dissipation rate conditioned on the temperature fluctuations for $y_s/h = 1.0$. In the present work, the scalar dissipation rate conditioned on the scalar fluctuation exhibit a concave-down, rounded V-shape. Such a shape indicates that large values of the scalar fluctuation are associated with low values of the scalar dissipation. The behavior of the experiments and the DNSs is similar, but not identical. Each plot begins with an approximately linear departure from $\theta/\theta_{rms} \approx -1.5$, increasing to a maximum, after which the conditional

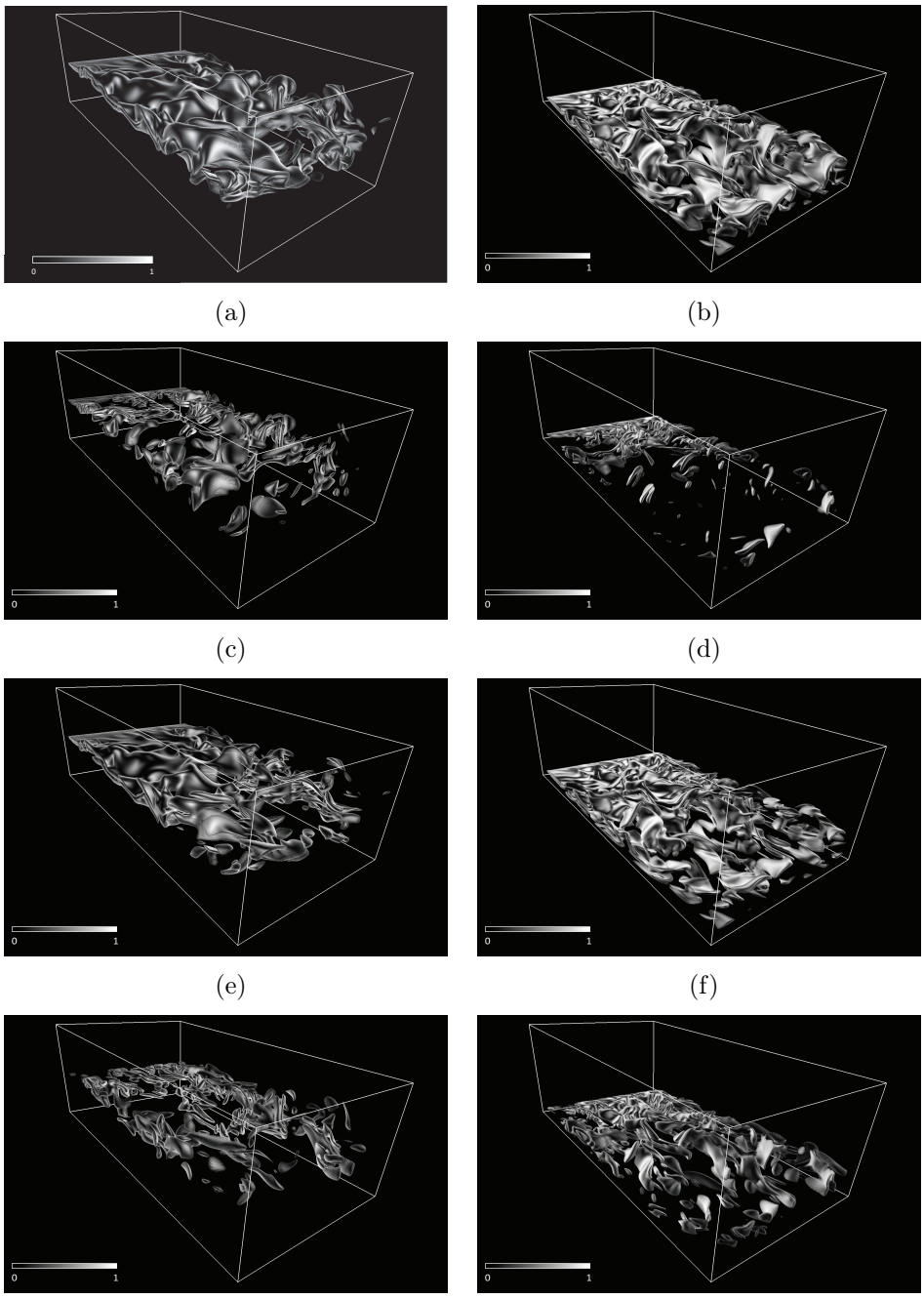

Figure 3–20: Instantaneous scalar dissipation rate fields – total and individual components – generated (by DNS) downstream of a line source at two wall-normal locations: $y_s/h = 1.0$ (a), (c), (e) and (g); $y_s/h = 0.17$ (b), (d), (f) and (h). $\alpha(\partial\theta/\partial x_i)^2$: (a) and (b). $\alpha(\partial\theta/\partial x)^2$: (c) and (d). $\alpha(\partial\theta/\partial y)^2$: (e) and (f). $\alpha(\partial\theta/\partial z)^2$: (g) and (h). $Re_\tau = 190$. $t^+ = 2770$ for the velocity field and $t^+ = 166$ for the scalar field (where, in the latter case, $t^+ = 0$ corresponds to the time at which the scalar is first injected into the flow). Note that the legends corresponds to the instantaneous scalar dissipation rates non-dimensionalized by $\varepsilon_\theta(t/t_L = 0.08, y/h = 1.0; y_s/h = 1.0)$. Imagery produced by VAPOR (www.vapor.ucar.edu – see also Clyne & Rast (2005); Clyne *et al.* (2007)).

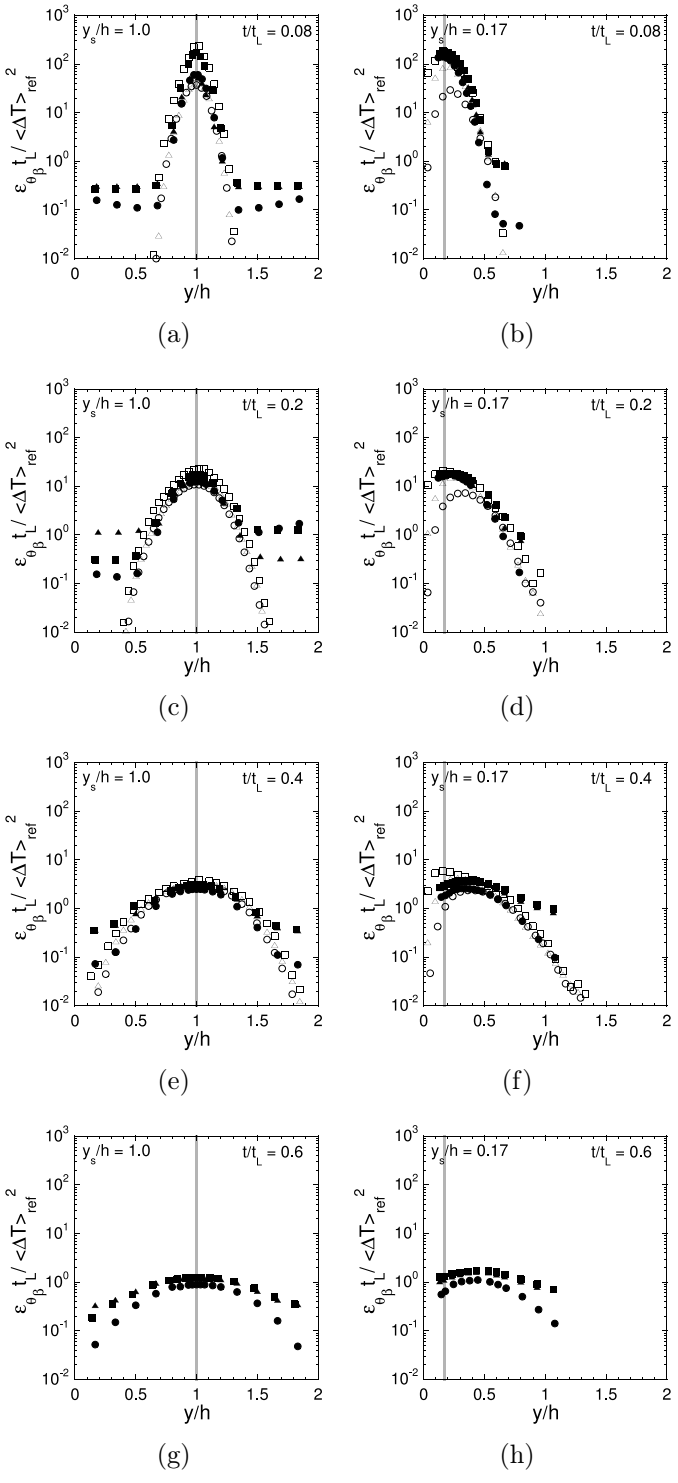

Figure 3–21: Wall-normal evolutions of the three components of the scalar dissipation rate for $y_s/h = 1.0$ and $y_s/h = 0.17$ at four downstream locations: $t/t_L = 0.08$ (a,b), $t/t_L = 0.2$ (c,d), $t/t_L = 0.4$ (e,f) and $t/t_L = 0.6$ (g,h). Experimental results are denoted by the solid symbols: ε_{θ_x} (●), ε_{θ_y} (■) and ε_{θ_z} (▲) and the numerical results are denoted by the open symbols: ε_{θ_x} (○), ε_{θ_y} (□) and ε_{θ_z} (△). The vertical line indicates the transverse location of the source.

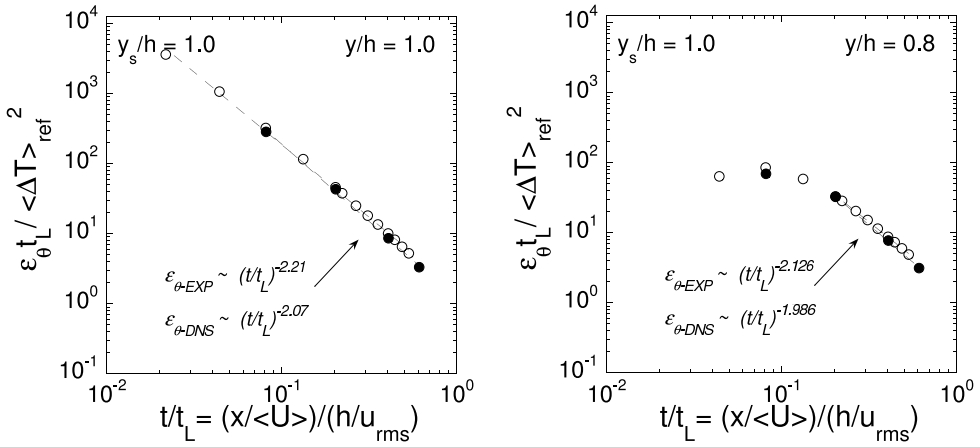

(a) (b)

Figure 3–22: Downstream evolution of the total scalar dissipation rate for $y_s/h = 1.0$ at two wall-normal locations: $y/h = 1.0$ (a) and $y/h = 0.8$ (b). Experimental results are denoted by the solid symbols and the numerical results are denoted by the open symbols. The solid line and dashed line are the best-fit power laws to the experimental and numerical data, respectively.

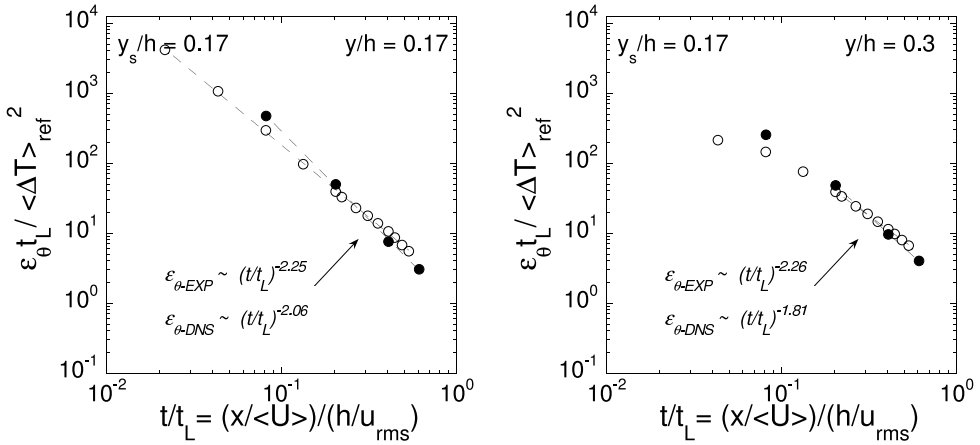

(a) (b)

Figure 3–23: Downstream evolution of the total scalar dissipation rate for $y_s/h = 0.17$ at two wall-normal locations: $y/h = 0.17$ (a) and $y/h = 0.3$ (b). Experimental results are denoted by the solid symbols and the numerical results are denoted by the open symbols. The solid line and dashed line are the best-fit power laws to the experimental and numerical data, respectively.

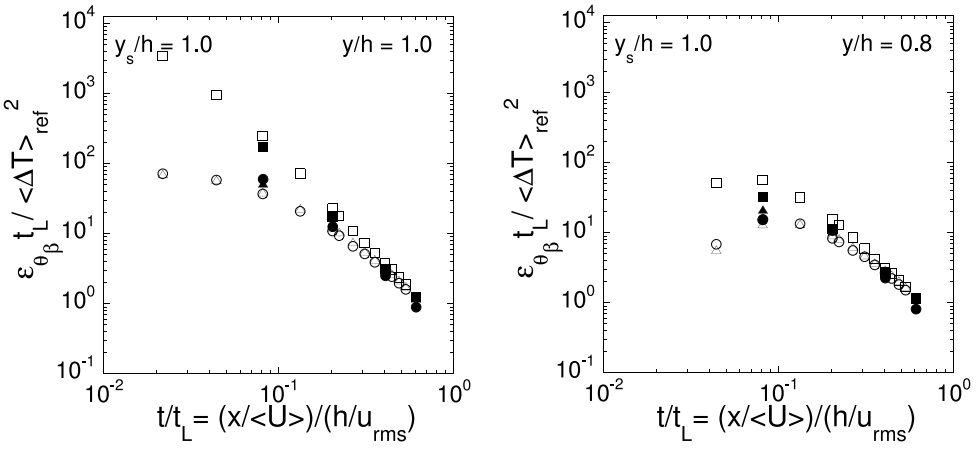

(a) (b)

Figure 3–24: Downstream evolution of the three components of the scalar dissipation rate for $y_s/h = 1.0$ at two wall-normal locations: $y/h = 1.0$ (a) and $y/h = 0.8$ (b). Experimental results are denoted by the solid symbols: ε_{θ_x} (•), ε_{θ_y} (■) and ε_{θ_z} (▲), and the numerical results are denoted by the open symbols: ε_{θ_x} (○), ε_{θ_y} (□) and ε_{θ_z} (△).

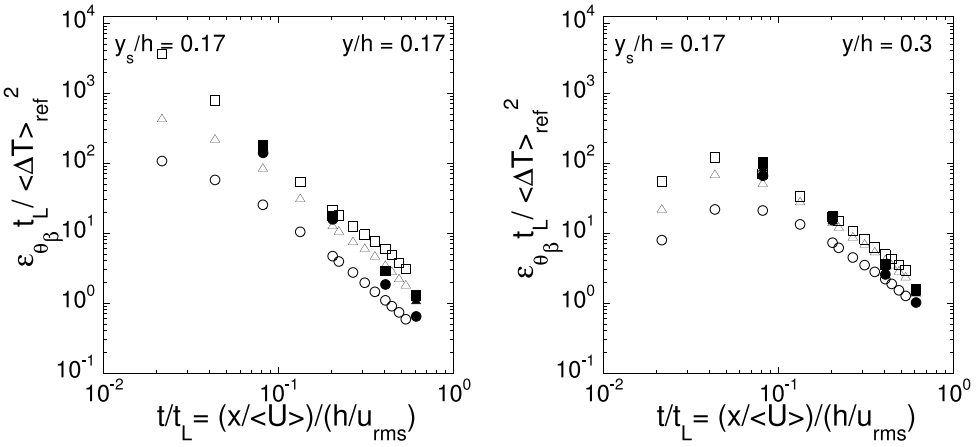

(a) (b)

Figure 3–25: Downstream evolution of the three components of the scalar dissipation rate for $y_s/h = 0.17$ at two wall-normal locations: $y/h = 0.17$ (a) and $y/h = 0.3$ (b). Experimental results are denoted by the solid symbols: ε_{θ_x} (•), ε_{θ_y} (■) and ε_{θ_z} (▲) and the numerical results are denoted by the open symbols: ε_{θ_x} (○), ε_{θ_y} (□) and ε_{θ_z} (△).

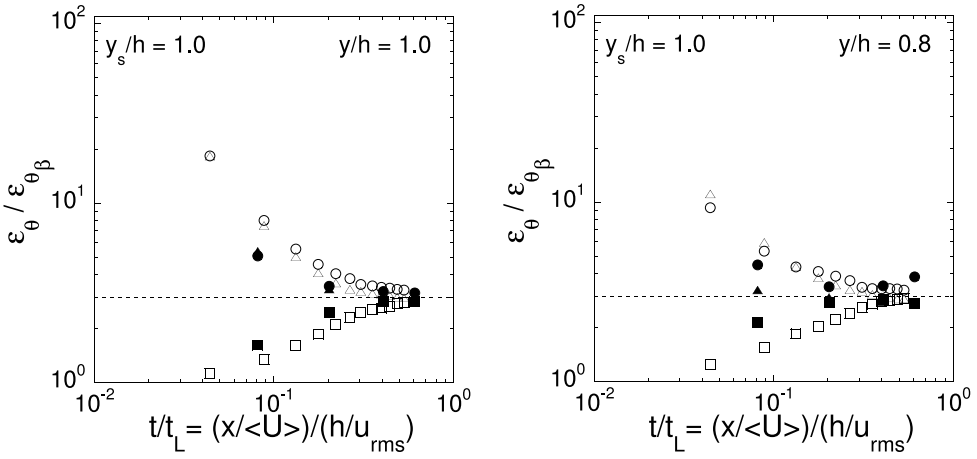

(a) (b)

Figure 3–26: Downstream evolution of the ratios $\varepsilon_\theta/\varepsilon_{\theta_\beta}$ (where $\beta = x, y$ or z) for $y_s/h = 1.0$ at two wall-normal locations: $y/h = 1.0$ (a) and $y/h = 0.8$ (b). Experimental results are denoted by the solid symbols: $\varepsilon_\theta/\varepsilon_{\theta_x}$ (●), $\varepsilon_\theta/\varepsilon_{\theta_y}$ (■) and $\varepsilon_\theta/\varepsilon_{\theta_z}$ (▲) and the numerical results are denoted by the open symbols: $\varepsilon_\theta/\varepsilon_{\theta_x}$ (○), $\varepsilon_\theta/\varepsilon_{\theta_y}$ (□) and $\varepsilon_\theta/\varepsilon_{\theta_z}$ (△).

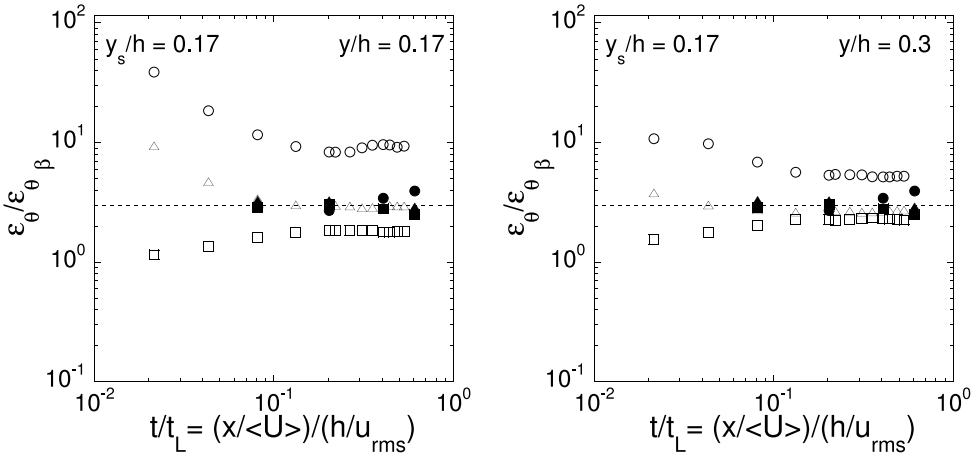

(a) (b)

Figure 3–27: Downstream evolution of the ratios $\varepsilon_\theta/\varepsilon_{\theta_\beta}$ (where $\beta = x, y$ or z) for $y_s/h = 0.17$ at two wall-normal locations: $y/h = 0.17$ (a) and $y/h = 0.3$ (b). Experimental results are denoted by the solid symbols: $\varepsilon_\theta/\varepsilon_{\theta_x}$ (●), $\varepsilon_\theta/\varepsilon_{\theta_y}$ (■) and $\varepsilon_\theta/\varepsilon_{\theta_z}$ (▲) and the numerical results are denoted by the open symbols: $\varepsilon_\theta/\varepsilon_{\theta_x}$ (○), $\varepsilon_\theta/\varepsilon_{\theta_y}$ (□) and $\varepsilon_\theta/\varepsilon_{\theta_z}$ (△).

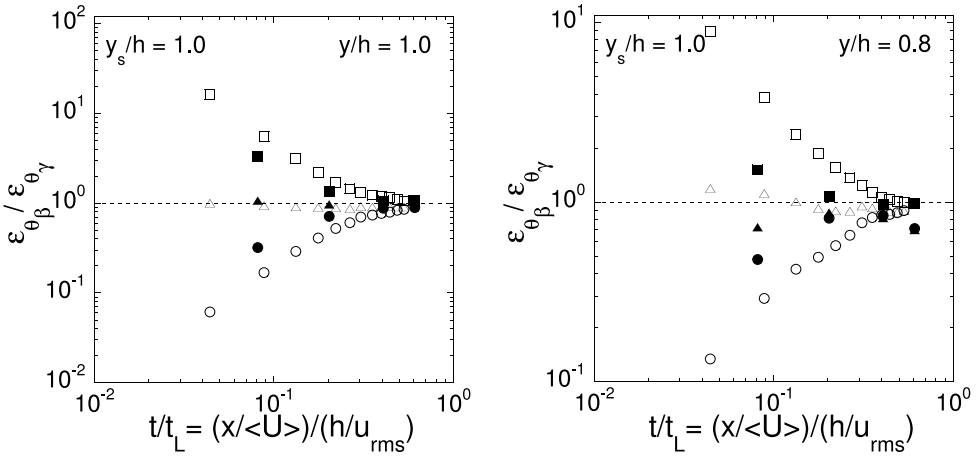

(a) (b)

Figure 3–28: Downstream evolution of the ratios $\varepsilon_{\theta_\beta}/\varepsilon_{\theta_\gamma}$ (where β and $\gamma = x, y$ or z and $\beta \neq \gamma$) for $y_s/h = 1.0$ at two wall-normal locations: $y/h = 1.0$ (a) and $y/h = 0.8$ (b). Experimental results are denoted by the solid symbols: $\varepsilon_{\theta_x}/\varepsilon_{\theta_y}$ (●), $\varepsilon_{\theta_y}/\varepsilon_{\theta_z}$ (■) and $\varepsilon_{\theta_x}/\varepsilon_{\theta_z}$ (▲) and the numerical results are denoted by the open symbols: $\varepsilon_{\theta_x}/\varepsilon_{\theta_y}$ (○), $\varepsilon_{\theta_y}/\varepsilon_{\theta_z}$ (□) and $\varepsilon_{\theta_x}/\varepsilon_{\theta_z}$ (△).

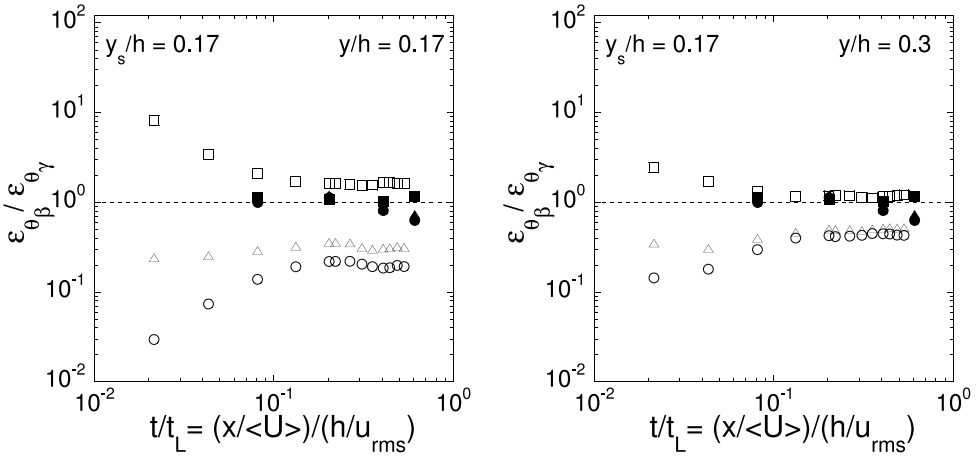

(a) (b)

Figure 3–29: Downstream evolution of the ratios $\varepsilon_{\theta_\beta}/\varepsilon_{\theta_\gamma}$ (where β and $\gamma = x, y$ or z and $\beta \neq \gamma$) for $y_s/h = 0.17$ at two wall-normal locations: $y/h = 0.17$ (a) and $y/h = 0.3$ (b). Experimental results are denoted by the solid symbols: $\varepsilon_{\theta_x}/\varepsilon_{\theta_y}$ (●), $\varepsilon_{\theta_y}/\varepsilon_{\theta_z}$ (■) and $\varepsilon_{\theta_x}/\varepsilon_{\theta_z}$ (▲) and the numerical results are denoted by the open symbols: $\varepsilon_{\theta_x}/\varepsilon_{\theta_y}$ (○), $\varepsilon_{\theta_y}/\varepsilon_{\theta_z}$ (□) and $\varepsilon_{\theta_x}/\varepsilon_{\theta_z}$ (△).

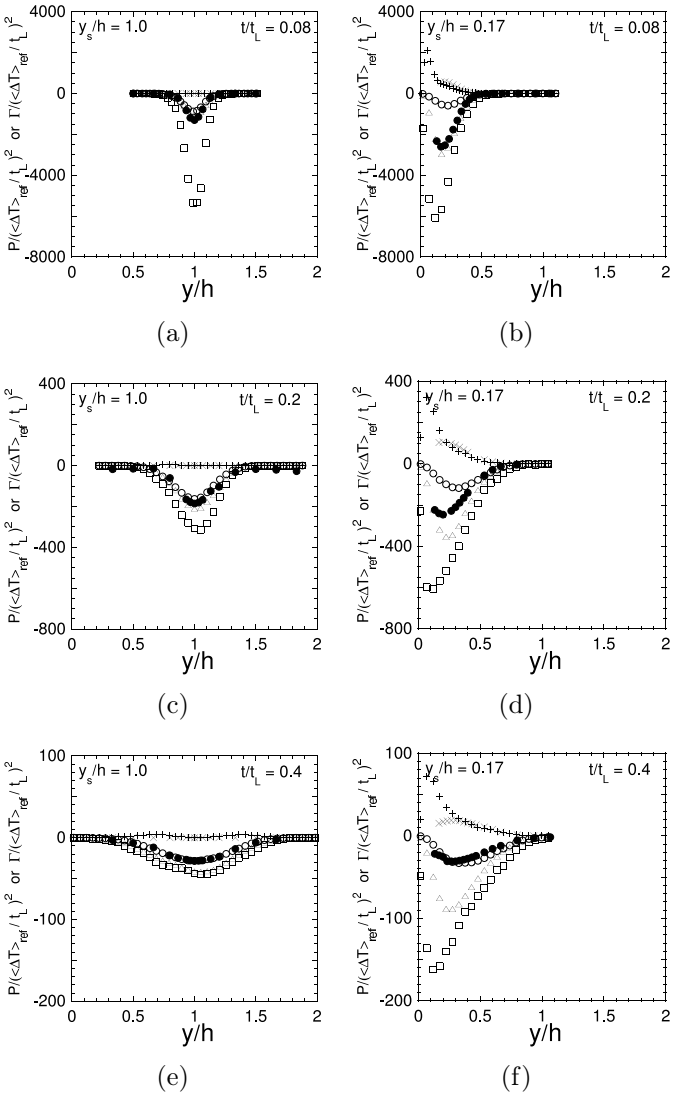

Figure 3–30: Wall-normal evolution of the y-component of the production of ε_θ by the three components of the dissipation of ε_θ and by the mean velocity gradient for $y_s/h = 1.0$ and $y_s/h = 0.17$ at three downstream locations: $t/t_L = 0.08$ (a), $t/t_L = 0.2$ (b) and $t/t_L = 0.4$ (c). Experimental results are denoted by the solid symbols: $-2\alpha^2\left(\langle(\partial^2\theta/\partial x^2)^2\rangle + \langle(\partial^2\theta/\partial x\partial y)^2\rangle + \langle(\partial^2\theta/\partial x\partial z)^2\rangle\right)$ ($\bullet$) and the numerical results are denoted by the open symbols: $-2\alpha^2\left[\langle(\partial^2\theta/\partial x^2)^2\rangle + \langle(\partial^2\theta/\partial x\partial y)^2\rangle + \langle(\partial^2\theta/\partial x\partial z)^2\rangle\right]$ ($\circ$), $-2\alpha^2\left[\langle(\partial^2\theta/\partial y\partial x)^2\rangle + \langle(\partial^2\theta/\partial y^2)^2\rangle + \langle(\partial^2\theta/\partial y\partial z)^2\rangle\right]$ ($\square$), $-2\alpha^2\left[\langle(\partial^2\theta/\partial z\partial x)^2\rangle + \langle(\partial^2\theta/\partial z\partial y)^2\rangle + \langle(\partial^2\theta/\partial z^2)^2\rangle\right]$ ($\triangle$). The production of dissipation $-2\alpha\langle U\rangle_y\langle(\partial\theta/\partial y)(\partial\theta/\partial x)\rangle$ is also reported for the experiments ($\times$) and the DNSs ($+$).

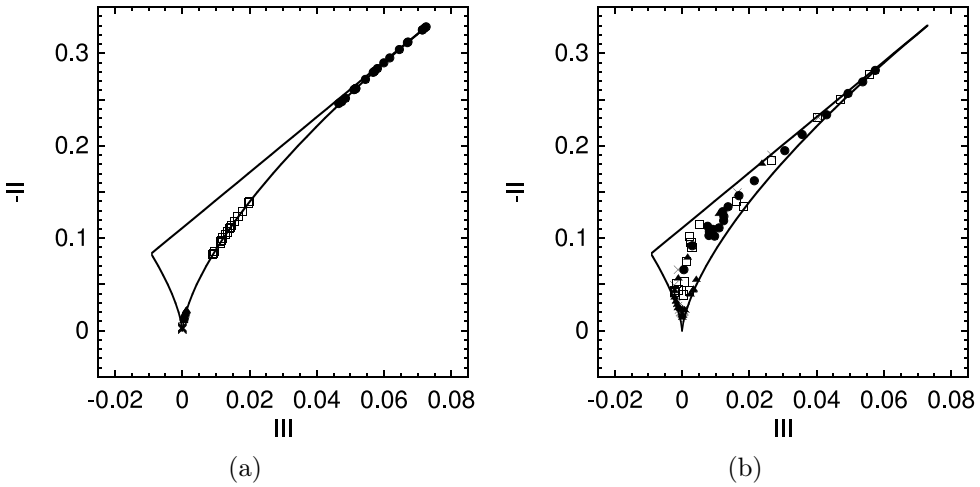

Figure 3–31: Anisotropy invariant map of ε_θ for $y_s/h = 1.0$ (a) and $y_s/h = 0.17$ (b). Statistics were computed at $t/t_L = 0.02$ ($\circ$), 0.08 ($\square$), 0.2 ($\triangle$) and 0.4 ($\times$) and for $y/h \in [0.8, 1.2]$ (a) and $y/h \in [0.0, 0.4]$ (b).

expectation begins to decrease. The double peaks of $\left\langle \varepsilon_{\theta_y} | \theta \right\rangle$ measured in the experiments in the vicinity of the source disappear farther downstream. These may be related to the previously discussed PDFs of $\partial\theta/\partial y$, which were shown to be bi- or trimodal near the source (see figure 3–18). Note that figure 3–34(d) has been plotted with different axis ranges due to large rare excursions in this part of the flow, where some measurements are outside the plume, and the others in its outer edges.

Figure 3–35 plots the conditional expectation $\left\langle \varepsilon_{\theta_\beta} | \theta/\theta_{rms} \right\rangle / \langle \varepsilon_{\theta_\beta} \rangle$ when the line source is near the wall ($y_s/h = 0.17$). The general form of the profiles is somewhat different from that with the centreline line source and is double peaked. In contrast with the DNS profiles, the experimental profiles increase near the upper limits of the range of temperature fluctuations. This increase also appears when the source is at the centreline but with a (relatively) smaller magnitude.

Kailasnath *et al.* (1993) investigated the conditional scalar dissipation rate in three different shear flows: wakes, jets, and in the atmospheric surface

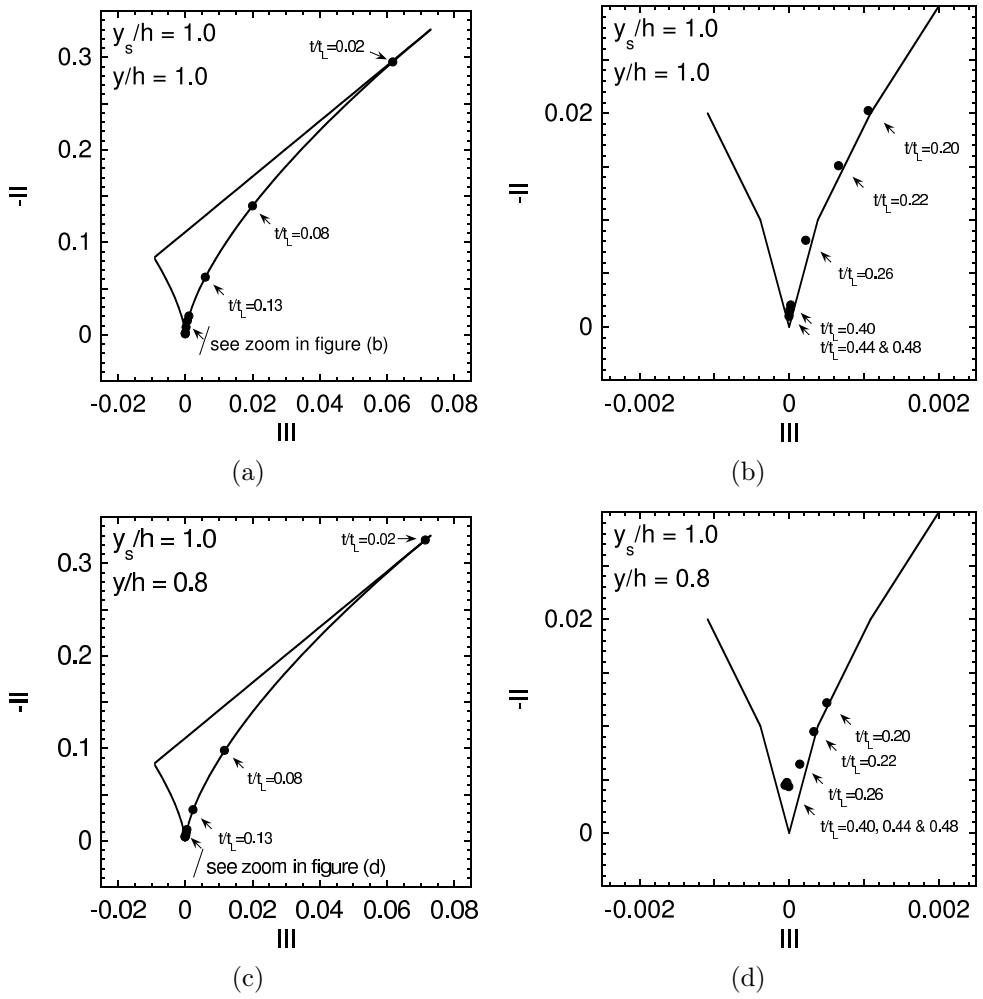

Figure 3–32: Anisotropy invariant map of ε_θ for $y_s/h = 1.0$ and $y/h = 1.0$ (a). A close-up of figure (a) is presented in figure (b). Anisotropy invariant map of ε_θ for $y_s/h = 1.0$ and $y/h = 0.8$ (c). A close-up of figure (c) is presented in figure (d). Statistics were computed from $t/t_L = 0.02$ to 0.48.

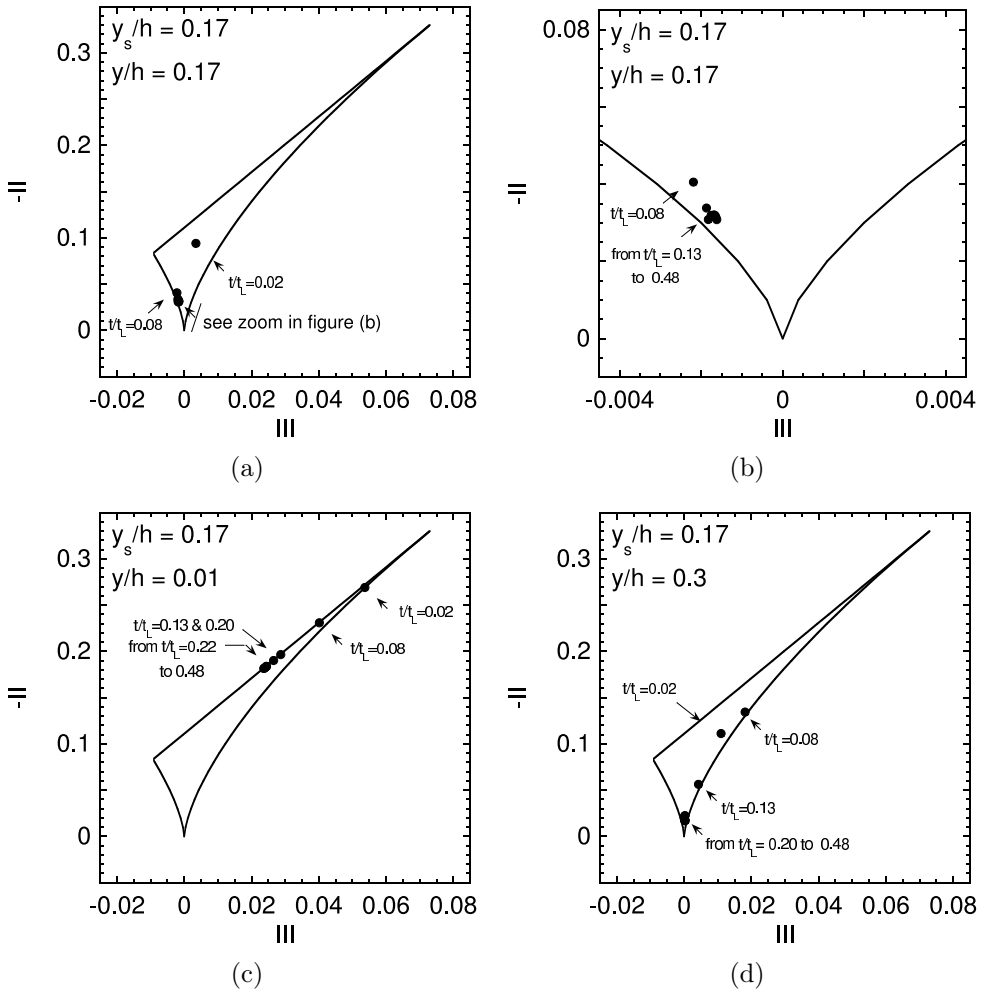

Figure 3–33: Anisotropy invariant map of ε_θ for $y_s/h = 0.17$ and $y/h = 0.17$ (a). A close-up of figure (a) is presented in figure (b). Anisotropy invariant map of ε_θ for $y_s/h = 0.17$ and $y/h = 0.01$ (c) and for $y_s/h = 0.17$ and $y/h = 0.3$ (d). Statistics were computed from $t/t_L = 0.02$ to 0.48.

layer. They also found that the "hot side" of the conditional expectation $\langle \varepsilon_\theta | \theta \rangle$ increased with θ. They concluded that the very hot events associated with very high intermittent dissipation rates were non-universal. In addition, they mentioned that the low temperature events may also be non-universal but their contribution to the conditional expectation is small because the dissipation in the cold fluid is small. These observations are consistent with the present results.

Independently of the source location, figure 3–35 shows a tendency to isotropic behavior as the downstream distance from the source increases. At low θ/θ_{rms}, the experiments and DNSs agree relatively well, like in figure 3–34. However, the discrepancies at large θ/θ_{rms} may be due to the difference in the rare events arising from the difference in the Reynolds numbers. That being said, the numerical simulations are more isotropic than the experiments. However, it should be reminded that the statistics related to the large positive fluctuations of θ are rare and may suffer from a reduced level of statistical convergence.

The expectations of the components of the dissipation conditioned upon individual values of the temperature derivatives, $\left\langle \varepsilon_{\theta_\beta} | \partial\theta/\partial x \right\rangle$, where $\beta = x,\ y$ or z, are plotted in figures 3–36 and 3–37 for the two line source locations presented herein. These figures show that larger magnitudes of $\partial\theta/\partial x$ lead to higher values of ε_{θ_x} consistent with the definition $\varepsilon_{\theta_x} \equiv \alpha \langle (\partial\theta/\partial x)^2 \rangle$. In addition, ε_{θ_y} and ε_{θ_z} do not directly depend on $\partial\theta/\partial x$ which explains the flatter profiles obtained for $\left\langle \varepsilon_{\theta_y} | \partial\theta/\partial x \right\rangle$ and $\langle \varepsilon_{\theta_z} | \partial\theta/\partial x \rangle$. That being said, they are clearly not independent, especially farther downstream. Overall, a very good agreement between experiments and DNSs is observed.

Figure 3–38 and 3–39 compare the expectations of $\varepsilon_{\theta_\beta}$ conditioned upon individual values of $\partial\theta/\partial x$, $\partial\theta/\partial y$, and $\partial\theta/\partial z$. The figures show consistent

results for all three components, where *i*) the correlation is highest when considering the component of ε_θ and the derivative of θ measured in the same direction, and *ii*) a reduced, but clearly non-zero, correlation is observed for the expectations conditioned on the temperature derivative in a different direction.

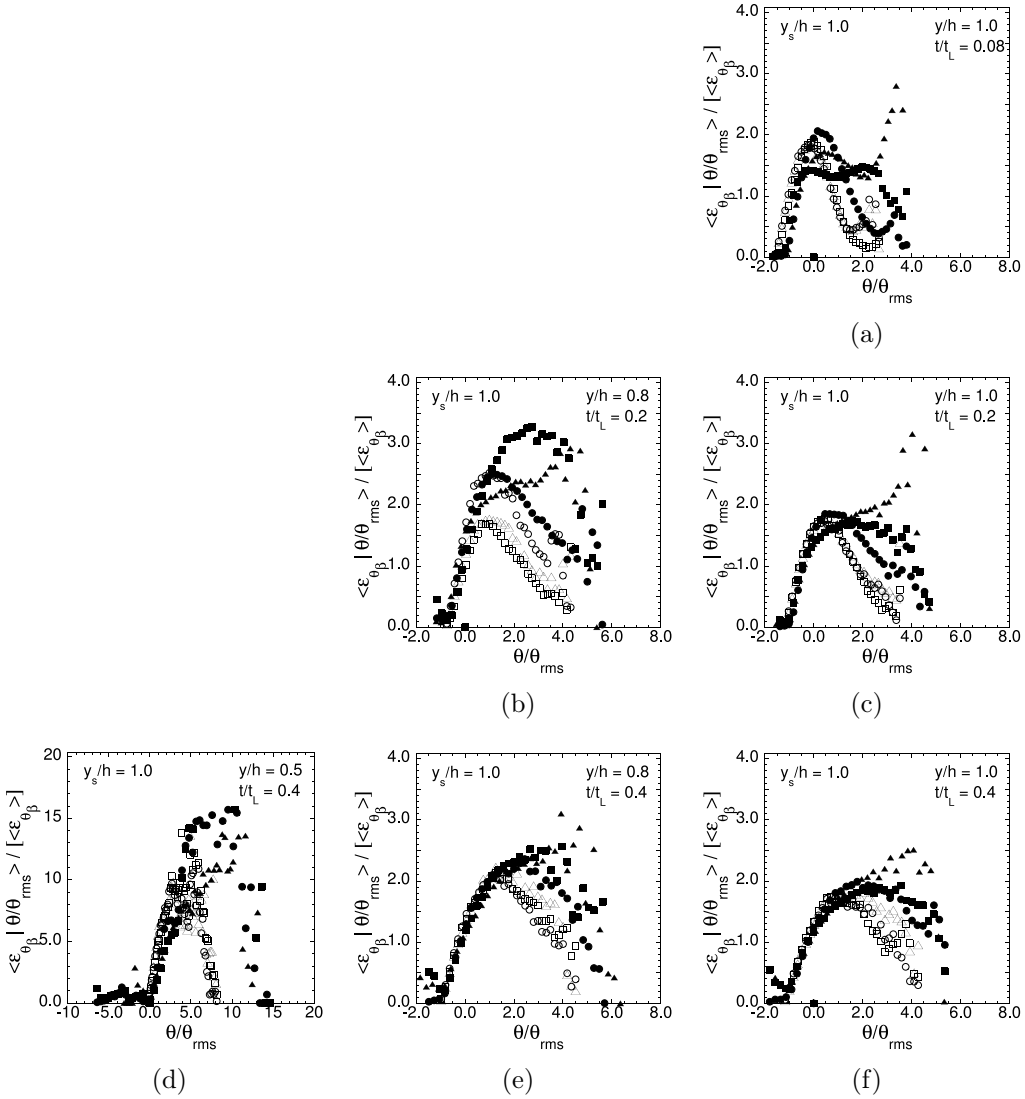

Figure 3–34: The expectation of the components of the temperature dissipation conditioned on the temperature fluctuations for $y_s/h = 1.0$ at three downstream locations: $t/t_L = 0.08$ (a), $t/t_L = 0.20$ (b,c) and $t/t_L = 0.40$ (d-f) at three wall-normal locations: $y/h = 1.0$ (a,c,f), $y/h = 0.8$ (b,e) and $y/h = 0.5$ (d). Experimental results are denoted by the solid symbols: $\langle \varepsilon_{\theta_x} | \theta \rangle$ (●), $\langle \varepsilon_{\theta_y} | \theta \rangle$ (■) and $\langle \varepsilon_{\theta_z} | \theta \rangle$ (▲) and the numerical results are denoted by the open symbols: $\langle \varepsilon_{\theta_x} | \theta \rangle$ (○), $\langle \varepsilon_{\theta_y} | \theta \rangle$ (□) and $\langle \varepsilon_{\theta_z} | \theta \rangle$ (△).

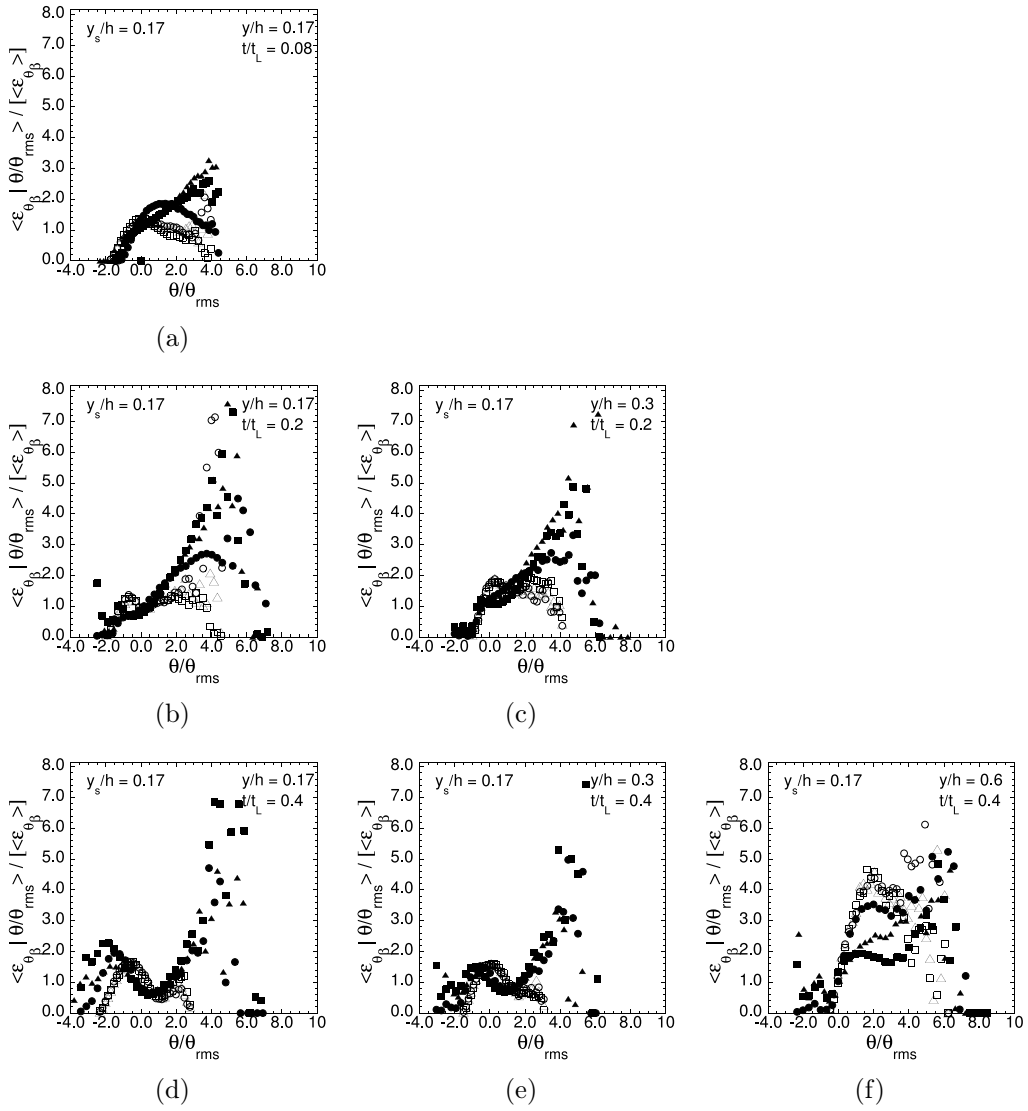

Figure 3–35: The expectation of the components of the temperature dissipation conditioned on the temperature fluctuations for $y_s/h = 0.17$ at three downstream locations: $t/t_L = 0.08$ (a), $t/t_L = 0.20$ (b,c) and $t/t_L = 0.40$ (d-f) at three wall-normal locations: $y/h = 0.17$ (a,b,d), $y/h = 0.3$ (c,e) and $y/h = 0.6$ (f). Experimental results are denoted by the solid symbols: $\langle \varepsilon_{\theta_x} | \theta \rangle$ (•), $\langle \varepsilon_{\theta_y} | \theta \rangle$ (■) and $\langle \varepsilon_{\theta_z} | \theta \rangle$ (▲) and the numerical results are denoted by the open symbols: $\langle \varepsilon_{\theta_x} | \theta \rangle$ (○), $\langle \varepsilon_{\theta_y} | \theta \rangle$ (□) and $\langle \varepsilon_{\theta_z} | \theta \rangle$ (△).

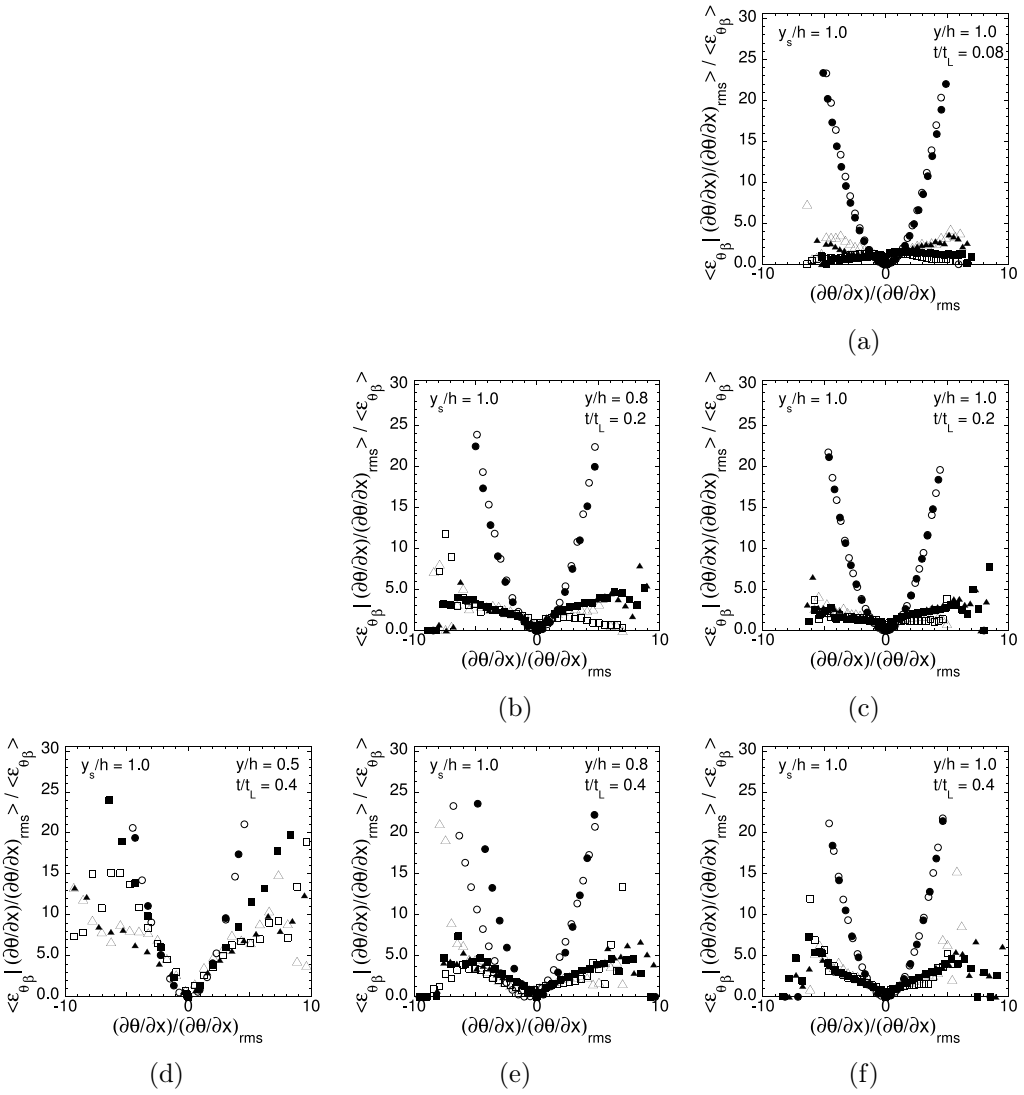

Figure 3–36: The expectation of the components of the temperature dissipation conditioned on the x-partial derivative of the temperature fluctuations for $y_s/h = 1.0$ at three downstream locations: $t/t_L = 0.08$ (a), $t/t_L = 0.20$ (b,c) and $t/t_L = 0.40$ (d-f) at three wall-normal locations: $y/h = 1.0$ (a,c,f), $y/h = 0.8$ (b,e) and $y/h = 0.5$ (d). Experimental results are denoted by the solid symbols: $\langle \varepsilon_{\theta_x} | \partial\theta/\partial x \rangle$ (●), $\langle \varepsilon_{\theta_y} | \partial\theta/\partial x \rangle$ (■) and $\langle \varepsilon_{\theta_z} | \partial\theta/\partial x \rangle$ (▲) and the numerical results are denoted by the open symbols: $\langle \varepsilon_{\theta_x} | \partial\theta/\partial x \rangle$ (○), $\langle \varepsilon_{\theta_y} | \partial\theta/\partial x \rangle$ (□) and $\langle \varepsilon_{\theta_z} | \partial\theta/\partial x \rangle$ (△).

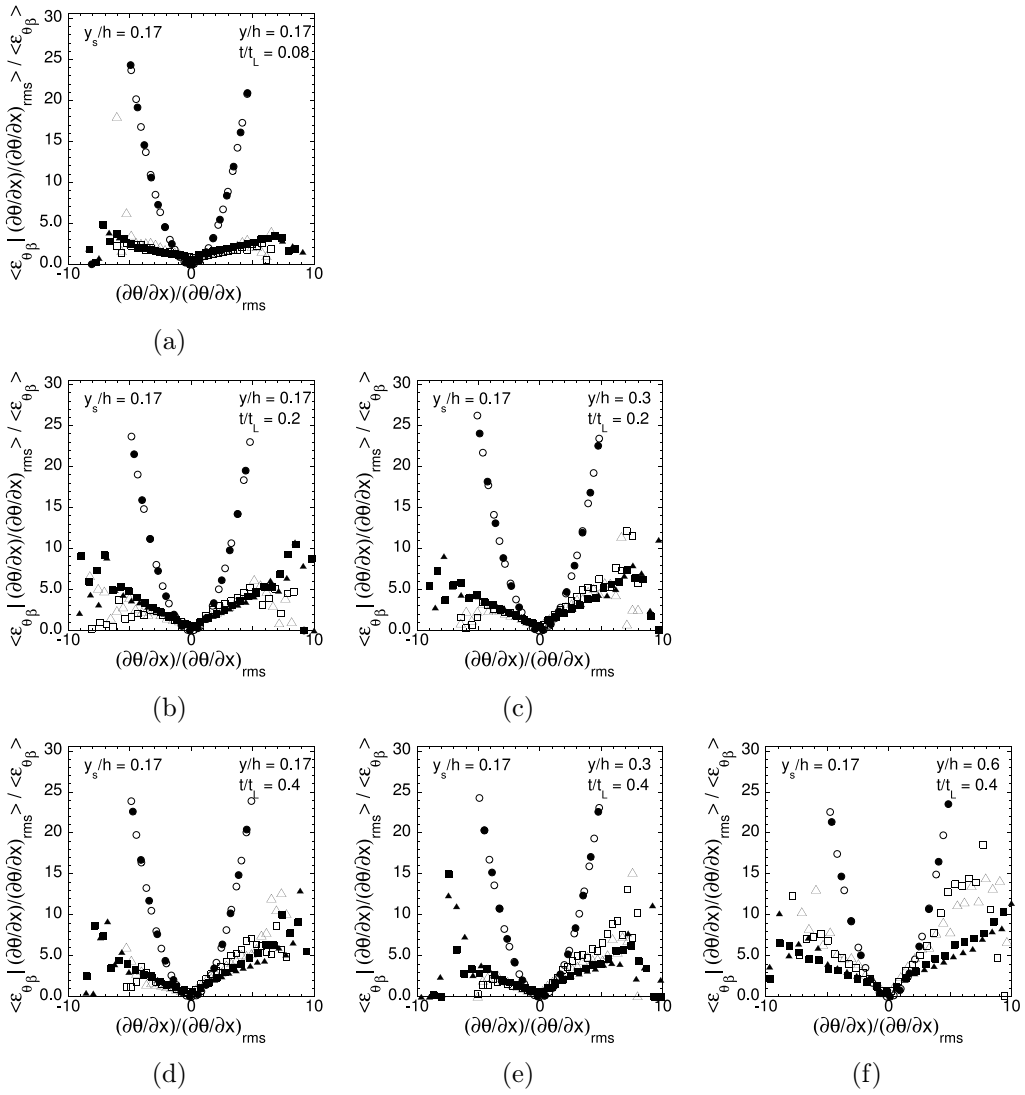

Figure 3–37: The expectation of the components of the temperature dissipation conditioned on the x-partial derivative of the temperature fluctuations for $y_s/h = 0.17$ at three downstream locations: $t/t_L = 0.08$ (a), $t/t_L = 0.20$ (b,c) and $t/t_L = 0.40$ (d-f) at three wall-normal locations: $y/h = 0.17$ (a,b,d), $y/h = 0.3$ (c,e) and $y/h = 0.6$ (f). Experimental results are denoted by the solid symbols: $\langle \varepsilon_{\theta_x} | \partial\theta/\partial x \rangle$ (●), $\langle \varepsilon_{\theta_y} | \partial\theta/\partial x \rangle$ (■) and $\langle \varepsilon_{\theta_z} | \partial\theta/\partial x \rangle$ (▲) and the numerical results are denoted by the open symbols: $\langle \varepsilon_{\theta_x} | \partial\theta/\partial x \rangle$ (○), $\langle \varepsilon_{\theta_y} | \partial\theta/\partial x \rangle$ (□) and $\langle \varepsilon_{\theta_z} | \partial\theta/\partial x \rangle$ (△).

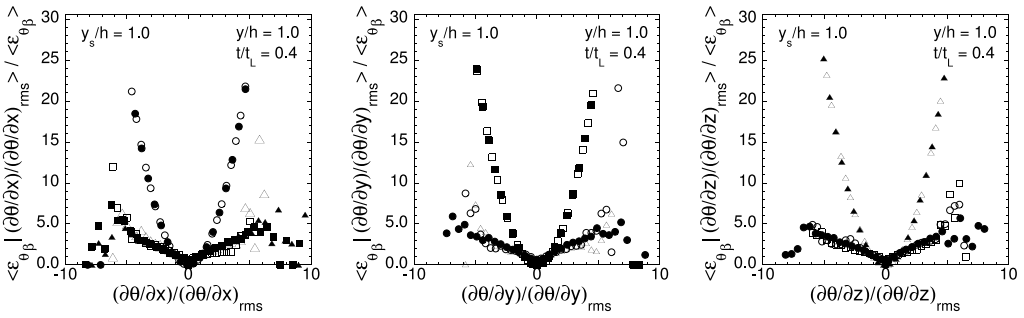

(d) (e) (f)

Figure 3–38: The expectation of the components of the temperature dissipation conditioned on the x-, y- and z-partial derivatives of the temperature fluctuations for $y_s/h = 1.0$ at $t/t_L = 0.40$ and $y/h = 1.0$. Experimental results are denoted by the solid symbols: $\langle \varepsilon_{\theta_x} | \partial\theta/\partial\beta \rangle$ (●) and $\left\langle \varepsilon_{\theta_y} | \partial\theta/\partial\beta \right\rangle$ (■) and the numerical results are denoted by the open symbols: $\langle \varepsilon_{\theta_x} | \partial\theta/\partial\beta \rangle$ (○), $\left\langle \varepsilon_{\theta_y} | \partial\theta/\partial\beta \right\rangle$ (□) and $\langle \varepsilon_{\theta_z} | \partial\theta/\partial\beta \rangle$ (△).

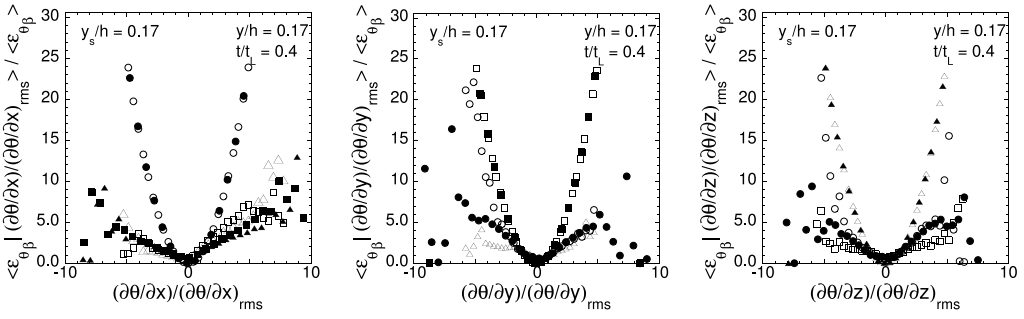

(d) (e) (f)

Figure 3–39: The expectation of the components of the temperature dissipation conditioned on the x-, y- and z-partial derivatives of the temperature fluctuations for $y_s/h = 0.17$ at $t/t_L = 0.40$ and $y/h = 0.17$. Experimental results are denoted by the solid symbols: $\langle \varepsilon_{\theta_x} | \partial\theta/\partial\beta \rangle$ (●) and $\left\langle \varepsilon_{\theta_y} | \partial\theta/\partial\beta \right\rangle$ (■) and the numerical results are denoted by the open symbols: $\langle \varepsilon_{\theta_x} | \partial\theta/\partial\beta \rangle$ (○), $\left\langle \varepsilon_{\theta_y} | \partial\theta/\partial\beta \right\rangle$ (□) and $\langle \varepsilon_{\theta_z} | \partial\theta/\partial\beta \rangle$ (△).

3.8 Conclusions

In the present work, the dissipation rate of a scalar (temperature) emitted from a concentrated line source in a fully developed turbulent channel flow was studied by means of both experiments and numerical simulations. The aim was to investigate the evolution of the small scales of the scalar field by measuring the (three components of the) scalar dissipation rate, ε_θ, at several downstream and wall-normal locations. The scalar was injected in a highly anisotropic manner and an examination of the downstream evolution of ε_θ permitted an investigation of the return to isotropy of the small scales of the scalar field.

Large- and small-scale statistics of the scalar field were reported for two different source locations ($y_s/h = 1.0$ and 0.17). Mean and r.m.s. statistics were computed from both experiments and DNSs, then analyzed, compared, and found to exhibit good overall agreement.

One-dimensional longitudinal power and dissipation spectra of the temperature fluctuations were reported at several downstream locations, both downstream of the source, as well as closer to the edges of the thermal plume. The small-scales statistics of the experiments and numerical simulations agree well, confirming that the DNS is capable of resolving the experimentally measured dissipative scales. In addition, comparison of the spectra measured when $y_s/h = 1.0$ and 0.17 support the notion that the scalar mixing is more rapid in the near-wall region. The discrepancies observed at large scales were attributed to the differences in the Reynolds number between the experiments ($Re_\tau = 520$) and the DNSs ($Re_\tau = 190$).

One-dimensional spectra of the temperature derivatives were subsequently presented. In the experiments, the y- and z-derivatives converge towards isotropy with increasing distance from the source at both large and small

scales, independently of the source location. ε_{θ_y} was clearly larger (when compared to ε_{θ_z}) close to the source, and the two components became almost indistinguishable farther downstream. The spectra obtained from the DNSs also exhibit a trend towards isotropy, excepted for the small-scale derivatives when $y_s/h = 0.17$. These latter results exhibit persistent small-scale anisotropy that were related to the high mean velocity gradients present in the near-wall region. This anisotropy was not observed in the experiments because *i*) our measurements were not performed sufficiently closed to the wall (due to technical constraints related to the size of the probes), and *ii*) they were undertaken at a significant larger Reynolds number.

The PDFs of the temperature derivatives ($\partial\theta/\partial x, \partial\theta/\partial y$ and $\partial\theta/\partial z$) were also studied at several downstream locations from the source. The results showed that the PDFs of the three derivatives were very similar and symmetric and develop exponential tails when measured sufficiently far downstream from the centreline source. However, significant difference in the PDF of $\partial\theta/\partial y$ were observed close to the source. Consistent with previous results, it was observed that exponential tails of the PDF, associated with a well mixed scalar field, appear sooner for the near-wall source than for the centreline source.

The wall-normal and downstream evolutions of the three components of the scalar dissipation rate were studied in detail. The experiments and DNSs showed good agreement, except in the near-wall region where the former were more isotropic than the latter. ε_θ was found to decay as $x^{-2\pm0.2}$ downstream of the source. Near the source, the y-component of ε_θ was clearly the largest, but its three components tended to isotropy when $y_s/h = 1.0$, whereas the decay of the anisotropy reached a plateau and remained constant with increasing downstream distance when $y_s/h = 0.17$. Finally, conditional statistics were

studied to investigate the dependence of the scalar fluctuations, θ, on their dissipation, ε_θ.

3.9 Acknowledgements

The authors acknowledge the gracious support of the Natural Sciences and Engineering Research Council of Canada.

CHAPTER 4

Conclusions and Future Work

This research aimed to develop a deeper understanding of scalar mixing in turbulent flows. In a turbulent flow that mixes a scalar, the large scales effect the majority of its transport, whereas the small scales diffuse the scalar fluctuations by molecular processes. Consequently, small-scale phenomena are fundamental to both understanding and predicting turbulent mixing. The fact that this phenomenon is not yet fully understood was the principal motivation for this research. Particular attention was paid to the small scales and their anisotropic behavior.

A passive scalar (temperature) was injected into a fully developed turbulent channel flow via a line source and analyzed by means of both experiments and numerical simulations. The scalar dissipation rate, ε_θ, was the focus of the research because it quantifies the rate at which the scalar fluctuations are destroyed. Measurements of its three components, $\varepsilon_{\theta_x}, \varepsilon_{\theta_y}$ and ε_{θ_z}, were performed at different locations in the streamwise and wall-normal directions of the flow. In addition, the influence of flow's inhomogeneity on the scalar mixing was investigated by injecting the temperature at two different wall-normal locations.

Complementary direct numerical simulations (DNSs) and experiments were performed. To this end, I developed a new numerical scheme, named

3DFLUX, for the solution of the advection-diffusion equation in three dimensions. 3DFLUX uses the flux integral method, i.e. a conservative form of the semi-Lagrangian method. It is a high-order (third-order in space and second-order in time), explicit, fully multidimensional, conservative and selective monotonicity preserving numerical scheme. The latter property prevents violations of the monotonicity of the solution near poorly resolved gradients from occurring, while preserving the global accuracy of the scheme. In addition, 3DFLUX is very attractive for practical applications as it does not necessitate dimensional splitting, leverages the multi-threaded architecture of modern CPUs, and generates highly accurate solutions at a realistic computational cost.

As discussed in chapter 2, 3DFLUX has been tested on several multidimensional problems, including purely advective and advective-diffusive problems, and has been shown to compare favorably with other methods. It notably resulted in a substantial improvement in accuracy over UTOPIA, the original version of the flux-integral method. In addition, 3DFLUX exhibited a better convergence rate than widely used one-dimensional techniques, such as the piecewise parabolic method (PPM), the weighted essentially non-oscillatory (WENO) method, and the recently-proposed jet scheme, which is based on the level-set method. Furthermore, the impact of the time integration scheme on the accuracy of the solution and the convergence rate of the scheme was shown. Somewhat surprisingly, it was found that, for very small time steps, the convergence rate can even be higher than the expected theoretical value, i.e. $O(h^3)$.

As discussed in chapter 3, 3DFLUX was used to simulate real experiments in turbulent flow. Due to the emergence of multi-core processors and the availability of high capacity memory chips, such complex simulations are

now possible with multidimensional schemes. Hence, the evolution of the three components of the scalar dissipation rate, ε_θ, was investigated at several downstream and wall-normal locations in the thermal plume behind a heated line source. Experimental and numerical results were compared and exhibited good agreement for both large- and small-scale statistics of the scalar field. Experimentally, the temperature fluctuations and temperature derivatives were measured by means of a pair of parallel cold-wire thermometers in a flow at $Re_\tau = 520$. In the DNSs, temperature derivatives were estimated by a finite central difference approximation. To emphasize on the role played by the wall on the scalar mixing, we performed our statistical analysis for two different line source locations: at the channel centreline ($y_s/h = 1.0$) and near the wall ($y_s/h = 0.17$).

The goal of combining both experiments and numerical simulations was particularly efficient and produced a significant quantity of statistical data on the scalar dissipation rate. It was observed that *i*) the small scales tend to become isotropic with increasing distance when the source is located at the centre of the channel, and *ii*) a return to isotropy of the small scales of the scalar field was not observed in the presence of high mean velocity gradients, at the lower Reynolds number characteristic of the DNS. An investigation of the scalar dissipation rate (and its components) when the source is oriented in the wall-normal direction, thus focussing on the lateral dispersion, would provide further information on the role played by the walls on the small scales of the scalar field. Further work examining the mixing from multiple line sources is also worth pursuing.

From a numerical methods perspective, 3DFLUX presently solves the three-dimensional linear advection-diffusion equation. However, further development is possible and could be the subject of future challenging project.

The present version of 3DFLUX uses a quadratic polynomial to approximate the scalar field within each computational cell. Investigation on the benefits of using higher-order polynomial should be performed. Furthermore, the use of non-uniform computational grids, which are widely used in CFD of practical applications, should be investigated. The solution of non-linear equations that can be cast in the form of equation (2.1) is theoretically possible, and could be, from my point of view, a major evolution for this code. Lastly, 3DFLUX is limited to problems for which the velocity field has been precomputed, but its scope would be considerably extended if it could also compute solutions to the Navier-Stokes equations.

REFERENCES

Abe, H., Kawamura, H. & Matsuo, Y. 2001 Direct numerical simulation of a fully developed turbulent channel flow with respect to the Reynolds number dependence. *J. Fluids Eng.* **123** (2), 382–393.

Abe, H., Kawamura, H. & Matsuo, Y. 2004 Surface heat-flux fluctuations in a turbulent channel flow up to $Re_\tau = 1020$ with $Pr = 0.025$ and 0.71. *Int. J. Heat Fluid Flow* **25** (3), 404–419.

Anselmet, F., Djeridi, H. & Fulachier, L. 1994 Joint statistics of a passive scalar and its dissipation in turbulent flows. *J. Fluid Mech.* **280**, 173–197.

Antonia, R.A. & Browne, L.W.B. 1986 Anisotropy of the temperature dissipation in a turbuelnt wake. *J. Fluid Mech.* **163**, 393–403.

Antonia, R. A. & Kim, J. 1994 A numerical study of local isotropy of turbulence. *Phys. Fluids* **6** (2), 834–841.

Antonia, R. A. & Mi, J. 1993 Temperature dissipation in a turbulent round jet. *J. Fluid Mech.* **250**, 531–551.

Bakosi, J., Franzese, P. & Boybeyi, Z. 2007 Probability density function modeling of scalar mixing from concentrated sources in turbulent channel flow. *Phys. Fluids* **19** (11), 115106.

Balsara, D. S. 2001 Divergence-free adaptive mesh refinement for magneto-hydrodynamics. *J. Comput. Phys.* **174** (2), 614–648.

Blossey, P. N. & Durran, D. R. 2008 Selective monotonicity preservation in scalar advection. *J. Comput. Phys.* **227** (10), 5160–5183.

Boppana, V. B. L., Xie, Z. T. & Castro, I. P. 2012 Large-eddy simulation

of dispersion from line sources in a turbulent channel flow. *Flow Turbul. Combust.* **88**, 311–342.

Bethouwer, G., Boersma, B. J., Pourquie, M. & Nieuwstadt, F. T. M. 1999 Direct numerical simulation of turbulent mixing of a passive scalar in pipe flow. *Eur. J. Mech. B-Fluid.* **18** (4), 739–756.

Chamecki, M., Meneveau, C. & Parlange, M. B. 2008 A hybrid spectral/finite-volume algorithm for large-eddy simulation of scalars in the atmospheric boundary layer. *Bound.-Lay. Meteorol.* **128** (3), 473–484.

Chung, M. K. & Kyong, N. H. 1989 Measurement of turbulent dispersion behind a fine cylindrical heat source in a weakly sheared flow. *J. Fluid Mech.* **205**, 171–193.

Clyne, John, Mininni, Pablo, Norton, Alan & Rast, Mark 2007 Interactive desktop analysis of high resolution simulations: application to turbulent plume dynamics and current sheet formation. *New J. Phys* **9** (301).

Clyne, John & Rast, Mark 2005 A prototype discovery environment for analyzing and visualizing terascale turbulent fluid flow simulations. In *Proceedings of Visualization and Data Analysis 2005*.

Colella, P. & Woodward, P. R. 1984 The piecewise parabolic method (PPM) for gas-dynamical simulations. *J. Comput. Phys.* **54** (1), 174–201.

Corrsin, S. 1951 On the spectrum of isotropic temperature fluctuations in an isotropic turbulence. *J. Appl. Phys.* **22** (4), 469–473.

Corrsin, S. 1952 Heat transfer in isotropic turbulence. *J. Appl. Phys.* **23**, 113–118.

Costa-Patry, E. & Mydlarski, L. 2008 Mixing of two thermal fields emitted from line sources in turbulent channel flow. *J. Fluid Mech.* **609**, 349–375.

Courant, R., Isaacson, E. & Rees, M. 1952 On the solution of nonlinear hyperbolic differential equations by finite differences. *Commun. Pure Appl.*

Math. **5** (3), 243–255.

Danaila, L., Antonia, R. A. & Burattini, P. 2012 Comparison between kinetic energy and passive scalar energy transfer in locally homogeneous isotropic turbulence. *Physica D: Nonlinear Phenomena* **241** (3), 224–231.

Durran, D. R. 1991 The third-order Adams-Bashforth method – an attractive alternative to Leapfrog time differencing. *Mon. Weather Rev.* **119** (3), 702–720.

Fackrell, J. E. & Robins, A. G. 1982 Concentration fluctuations and fluxes in plumes from point sources in a turbulent boundary layer. *J. Fluid Mech.* **117**, 1–26.

Falcone, M. & Ferretti, R. 2002 Semi-Lagrangian schemes for Hamilton-Jacobi equations, discrete representation formulae and Godunov methods. *J. Comput. Phys.* **175** (2), 559–575.

Ferziger, J. H. & Perić, M. 2002 *Computational methods for fluid dynamics*, 3rd edn. Berlin-Heidelberg: Springer Verlag.

Galantucci, L. & Quadrio, M. 2010 Very fine near-wall structures in turbulent scalar mixing. *Int. J. Heat Fluid Flow* **31** (4), 499–506.

Germaine, E., Mydlarski, L. & Cortelezzi, L. 2013 3DFLUX: A high-order fully three-dimensional flux integral solver for the scalar transport equation. *J. Comput. Phys.* **240**, 121–144.

Gibson, J. F. 2010*a* Channelflow: A spectral Navier-Stokes simulator in `C++`. *Tech. Rep.*. New Hampshire University.

Gibson, J. F. 2010*b* Channelflow: A spectral Navier-Stokes simulator in `C++`. *Tech. Rep.*. University of New Hampshire.

Gibson, J. F., Halcrow, J. & Cvitanović, P. 2008 Visualizing the geometry of state space in plane Couette flow. *J. Fluid Mech.* **611**, 107–130.

Godunov, S. K. 1959 A difference method for numerical calculation of discontinuous solutions of the equations of hydrodynamics. *Mat. Sb.* **47** (3), 271–306.

Gonzalez, M. 2000 Study of the anisotropy of a passive scalar field at the level of dissipation. *Phys. Fluids* **12** (9), 2302–2310.

Harris, L. M., Lauritzen, P. H. & Mittal, R. 2011 A flux-form version of the conservative semi-lagrangian multi-tracer transport scheme (CSLAM) on the cubed sphere grid. *J. Comput. Phys.* **230** (4), 1215–1237.

Harten, A. 1983 High resolution schemes for hyperbolic conservation laws. *J. Comput. Phys.* **49** (3), 357–393.

Hasumi, H. & Daigaku, T. 2006 *CCSR ocean component model (COCO) Version 4.0*. Center for Climate System Research, University of Tokyo.

Hussain, A. K. M. F. & Reynolds, W. C. 1975 Measurements in fully developed turbulent channel flow. *J. Fluids Eng.* **97**, 568–578.

Incropera, F. P., De Witt, D. P., Bergman, T. L. & Lavine, A. S. 2007 *Fundamentals of heat and mass transfer*, 6th edn. New York: John Wiley and Sons Inc.

Jakobsen, H. A. 2008 *Chemical reactor modeling: multiphase reactive flows*. Berlin Heidelberg: Springer Verlag.

Jayesh & Warhaft, Z. 1992 Probability distribution, conditional dissipation, and transport of passive temperature fluctuations in grid-generated turbulence. *Phys. Fluids A* **4** (10), 2292–2307.

Jiang, G. S. & Shu, C. W. 1996 Efficient implementation of weighted ENO schemes. *J. Comput. Phys.* **126** (1), 202–228.

Johansson, A. V. & Wikström, P. M. 1999 DNS and modelling of passive scalar transport in turbulent channel flow with a focus on scalar dissipation rate modelling. *Flow Turbul. Combust.* **63**, 223–245.

Kailasnath, P., Sreenivasan, K. R. & Saylor, J. R. 1993 Conditional scalar dissipation rates in turbulent wakes, jets, and boundary layers. *Phys. Fluids A* **5** (12), 3207–3215.

Karnik, U. & Tavoularis, S. 1989 Measurements of heat diffusion from a continuous line source in a uniformly sheared turbulent flow. *J. Fluid Mech.* **202**, 233–261.

Kawamura, H., Ohsaka, K., Abe, H. & Yamamoto, K. 1998 DNS of turbulent heat transfer in channel flow with low to medium-high prandtl number fluid. *Int. J. Heat Fluid Fl.* **19** (5), 482–491.

Kim, J., Moin, P. & Moser, R. 1987 Turbulence statistics in fully developed channel flow at low Reynolds number. *J. Fluid Mech.* **177**, 133–166.

Kolmogorov, A. 1941 The local structure of turbulence in incompressible viscous fluid for very large Reynolds numbers. *Dokl. Akad. Nauk SSSR* **30**, 301–305.

Kozlov, R., Kværnø, A. & Owren, B. 2004 The behaviour of the local error in splitting methods applied to stiff problems. *J. Comput. Phys.* **195** (2), 576–593.

Kozuka, M., Seki, Y. & Kawamura, H. 2009 DNS of turbulent heat transfer in a channel flow with a high spatial resolution. *Int. J. Heat Fluid Fl.* **30** (3), 514–524.

Krivodonova, L. & Berger, M. 2006 High-order accurate implementation of solid wall boundary conditions in curved geometries. *J. Comput. Phys.* **211** (2), 492–512.

LaRue, J. C. & Libby, P. A. 1981 Thermal mixing layer downstream of half-heated turbulence grid. *Phys. Fluids* **24** (4), 597–603.

Lavertu, R. A. & Mydlarski, L. 2005 Scalar mixing from a concentrated source in turbulent channel flow. *J. Fluid Mech.* **528**, 135–172.

Lemay, J. & Benaïssa, A. 2001 Improvement of cold-wire response for measurement of temperature dissipation. *Exp. Fluids* **31** (3), 347–356.

Leonard, B. P. 1979 A stable and accurate convective modelling procedure based on quadratic upstream interpolation. *Comput. Methods Appl. Mech. Engrg.* **19** (1), 59–98.

Leonard, B. P. 1997 Bounded higher-order upwind multidimensional finite-volume convection-diffusion algorithms. In *Advances in Numerical Heat Transfer, vol. 1* (ed. W.J. Minkowycz & E.M. Sparrow), pp. 1–57. Taylor and Francis, New York.

Leonard, B. P., Lock, A. P. & MacVean, M. K. 1996 Conservative explicit unrestricted-time-step multidimensional constancy-preserving advection schemes. *Mon. Weather Rev.* **124** (11), 2588–2606.

Leonard, B. P., MacVean, M. K. & Lock, A. P. 1993 Positivity-preserving numerical schemes for multidimensional advection. *NASA-TM-106055, ICOMP-93-05, E-7656, NAS 1.15:106055* pp. 1–62.

Leonard, B. P., MacVean, M. K. & Lock, A. P. 1995 The flux integral method for multidimensional convection and diffusion. *Appl. Math. Model.* **19** (6), 333–342.

Lepore, J. & Mydlarski, L. 2011 Lateral dispersion from a concentrated line source in turbulent channel flow. *J. Fluid Mech.* **678**, 417–450.

Leveque, R. J. 1996 High-resolution conservative algorithms for advection in incompressible flow. *SIAM J. Numer. Anal.* **33** (2), 627–665.

Leveque, R. J. 2002 *Finite volume methods for hyperbolic problems*. Cambridge: Cambridge Texts in Applied Mathematics, Cambridge University Press.

Li, S. & Li, H. 2004 A novel approach of divergence-free reconstruction for adaptive mesh refinement. *J. Comput. Phys.* **199**, 1–15.

Liu, J. G., Wang, C. & Johnston, H. 2003 A fourth order scheme for incompressible Boussinesq equations. *J. Sci. Comput.* **18** (2), 253–285.

Liu, X. D., Osher, S. & Chan, T. 1994 Weighted essentially non-oscillatory schemes. *J. Comput. Phys.* **115** (1), 200–212.

Livescu, D., Jaberi, F. A. & Madnia, C. K. 2000 Passive-scalar wake behind a line source in grid turbulence. *J. Fluid Mech.* **416**, 117–149.

Lockwood, F. C. & Moneib, H. A. 1980 Fluctuating temperature measurements in a heated round free jet. *Combust. Sci. Technol.* **22** (1-2), 63–81.

Lohéac, J. P. 1991 An artificial boundary condition for an advection-diffusion equation. *Math. Methods Appl. Sci.* **14** (3), 155–175.

Lumley, J. L. 1978 Computational modeling of turbulent flows. *Adv. Appl. Mech.* **18** (1), 123–176.

Ma, B. K. & Warhaft, Z. 1986 Some aspects of the thermal mixing layer in grid turbulence. *Phys. Fluids* **29** (10), 3114–3120.

Mittal, R. & Skamarock, W. C. 2010 Monotonic limiters for a second-order finite volume advection scheme using icosahedral-hexagonal meshes. *Mon. Weather Rev.* **138** (12), 4523–4527.

Moin, P. & Mahesh, K. 1998 Direct numerical simulation: a tool in turbulence research. *Annu. Rev. Fluid Mech.* **30**, 539–578.

Moser, R. D., Kim, J. & Mansour, N. N. 1999 Direct numerical simulation of turbulent channel flow up to $Re = 590$. *Phys. Fluids* **11** (4), 943–945.

Mydlarski, L. 2003 Mixed velocity-passive scalar statistics in high-Reynolds-number turbulence. *J. Fluid Mech.* **475**, 173–203.

Mydlarski, L., Danaila, L. & Lavertu, R. A. 2007 Isotropy of the temperature field downstream of a line source in turbulent channel flow. *Advances in Turbulence XI, Proc. the 11th EUROMECH European Turbulence Conference* **117**, 500–502.

Nassehi, V. & Das, D. B. 2007 *Computational methods in the management of hydro-environmental systems*. London: IWA publishing.

Nave, J. C., Rosales, R. R. & Seibold, B. 2010 A gradient-augmented level set method with an optimally local, coherent advection scheme. *J. Comput. Phys.* **229** (10), 3802–3827.

Nordström, J., Nordin, N. & Henningson, D. 1999 The fringe region technique and the Fourier method used in the direct numerical simulation of spatially evolving viscous flows. *SIAM J. Sci. Comput.* **20** (4), 1365–1393.

Obukhov, AM 1949 Structure of the temperature field in a turbulent current. *Izv. Aka. Nauk. SSSR, Ser. Geograf. Geofiz* **13**, 58–69.

Orszag, S. A. 1971 Numerical simulation of incompressible flows within simple boundaries: accuracy. *J. Fluid Mech.* **49**, 75–112.

Paoli, R., Poinsot, T. & Shariff, K. 2006 Testing semi-Lagrangian schemes for two-phase flow applications. In *Center for Turbulence research, proceedings of the summer program, Stanford University*, pp. 213–222.

Paranthoën, P., Fouari, A., Dupont, A. & Lecordier, J. C. 1988 Dispersion measurements in turbulent flows (boundary layer and plane jet). *Int. J. Heat Mass Transfer* **31**, 153–165.

Patankar, S. V. 1980 *Numerical heat transfer and fluid flow*. London: Hemisphere Publishing Corporation.

Pope, S. B. & Ching, E. S. C. 1993 Stationary probability density functions: An exact result. *Phys. Fluids* **5**, 1529–1531.

Pozrikidis, C. 1998 *Numerical computation in science and engineering*. London: Oxford University Press.

Prasad, R. R. & Sreenivasan, K. R. 1990 Quantitative three-dimensional imaging and the structure of passive scalar fields in fully turbulent flows. *J. Fluid Mech.* **216**, 1–34.

Press, W. H., Teukolsky, S. A., Vetterling, W. T. & Flannery, B. P. 2007 *Numerical recipes: the art of scientific computing*, 3rd edn. Cambridge: Cambridge University Press.

Raupach, M. R. & Legg, B. J. 1983 Turbulent dispersion from an elevated line source: measurements of wind-concentration moments and budgets. *J. Fluid Mech.* **136**, 111–137.

Rosset, L., Paranthoën, P., Lecordier, J. C. & Gonzalez, M. 2001 Anisotropy of a thermal field at dissipative scales in the case of small-scale injection. *Phys. Fluids* **13** (12), 3729–3737.

Russell, W. S. 1995 Polynomial interpolation schemes for internal derivative distributions on structured grids. *Appl. Numer. Math.* **17** (2), 129–171.

Schlatter, P., Adams, N. A. & Kleiser, L. 2005 A windowing method for periodic inflow/outflow boundary treatment of non-periodic flows. *J. Comput. Phys.* **206** (2), 505–535.

Schumacher, J., Sreenivasan, K. R. & Yeung, P. K. 2005 Very fine structures in scalar mixing. *J. Fluid Mech.* **531**, 113–122.

Schwertfirm, F. & Manhart, M. 2007 DNS of passive scalar transport in turbulent channel flow at high Schmidt numbers. *Int. J. Heat Fluid Fl.* **28** (6), 1204–1214.

Seibold, B., Rosales, R. R. & Nave, J. C. 2012 Jet schemes for advection problems. *Discrete Contin. Dyn. Syst. Ser. B* **17** (4), 1229 – 1259.

Simens, M. P., Jiménez, J., Hoyas, S. & Mizuno, Y. 2009 A high-resolution code for turbulent boundary layers. *J. Comput. Phys.* **228** (11), 4218–4231.

Sinai, Y. G. & Yakhot, V. 1989 Limiting probability distributions of a passive scalar in a random velocity field. *Phys. Rev. Lett.* **63** (18), 1962–1964.

Skamarock, W. C. 2006 Positive-definite and monotonic limiters for unrestricted-time-step transport schemes. *Mon. Weather Rev.* **134** (8), 2241–2250.

Spalding, D. B. 1972 A novel finite difference formulation for differential expressions involving both first and second derivatives. *Int. J. Numer. Meth. Eng.* **4** (1), 551–559.

Sreenivasan, K. R. 1991 On local isotropy of passive scalars in turbulent shear flows. *Proc. R. Soc. London, Ser. A* **434** (1890), 165–182.

Sreenivasan, K. R., Antonia, R. A. & Danh, H. Q. 1977 Temperature dissipation fluctuations in a turbulent boundary layer. *Phys. Fluids* **20**, 1238–1249.

Staniforth, A. & Côté, J. 1991 Semi-Lagrangian integration schemes for atmospheric models – A review. *Mon. Weather Rev.* **119** (9), 2206–2223.

Stapountzis, H., Sawford, B. L., Hunt, J. C. R. & Britter, R. E. 1986 Structure of the temperature field downwind of a line source in grid turbulence. *J. Fluid Mech.* **165**, 401–424.

Strang, G. 1968 On the construction and comparison of difference schemes. *SIAM J. Numer. Anal.* **5** (3), 506–517.

Tan, S. & Shu, C. W. 2010 Inverse Lax-Wendroff procedure for numerical boundary conditions of conservation laws. *J. Comput. Phys.* **229** (21), 8144–8166.

Taylor, G. I. 1935 Statistical theory of turbulence. parts $1-4$. *Proc. R. Soc. London, Ser. A* **151** (873), 421–478.

Thoroddsen, S. T. & Van Atta, C. W. 1996 Experiments on density-gradient anisotropies and scalar dissipation of turbulence in a stably stratified fluid. *J. Fluid Mech.* **322**, 383–409.

Thuburn, J. 1996 Multidimensional flux-limited advection schemes. *J. Comput. Phys.* **123** (1), 74–83.

Tong, C. & Warhaft, Z. 1995 Passive scalar dispersion and mixing in a turbulent jet. *J. Fluid Mech* **292**, 1–38.

Tsynkov, S. V. 1998 Numerical solution of problems on unbounded domains. A review. *Appl. Numer. Math.* **27** (4), 465–532.

Uberoi, M. S. & Corrsin, S. 1952 Diffusion of heat from a line source in isotropic turbulence. *Tech. Rep.* Note 2710 (also NACA Rep. 1142). Nat. Adv. Comm. Aero.

Van Atta, C. 1991 Local isotropy of the smallest scales of turbulent scalar and velocity fields. *Proc. R. Soc. London, Ser. A* **434** (1890), 139–147.

Versteeg, H. K. & Malalasekera, W. 2007 *An introduction to computational fluid dynamics: the finite volume method*. Harlow: Pearson Education Limited.

Vrieling, A. J. & Nieuwstadt, F. T. M. 2003 Turbulent dispersion from nearby point sources interference of the concentration statistics. *Atmos. Environ.* **37** (32), 4493–4506.

Warhaft, Z. 1984 The interference of thermal fields from line sources in grid turbulence. *J. Fluid Mech.* **144**, 363–387.

Warhaft, Z. 2000 Passive scalars in turbulent flows. *Annu. Rev. Fluid Mech.* **32**, 203–240.

Wyngaard, J. C. 1969 Spatial resolution of the vorticity meter and other hot-wire arrays. *J. Phys. E: Sci. Instrum.* **2**, 983–987.

Xiu, D. & Karniadakis, G. E. 2001 A semi-Lagrangian high-order method for Navier-Stokes equations. *J. Comput. Phys.* **172** (2), 658–684.

Xu, J., Xiu, D. & Karniadakis, G. E. 2002 A semi-Lagrangian method for turbulence simulations using mixed spectral discretizations. *J. Sci. Comput.*

17 (1-4), 585–597.

Zalesak, S. T. 1979 Fully multidimensional flux-corrected transport algorithms for fluids. *J. Comput. Phys.* **31** (3), 335–362.

Zalesak, S. T. 2005 The design of flux-corrected transport (FCT) algorithms for structured grids. In *Flux-Corrected Transport* (ed. D. Kuzmin, R. Löhner & S. Turek), pp. 29–78. Springer, New York.

Zhou, T., Antonia, R. A., Lasserre, J. J., Coantic, M. & Anselmet, F. 2003 Transverse velocity and temperature derivative measurements in grid turbulence. *Exp. Fluids* **34** (4), 449–459.